MANUEL GLAS

# Mn-BASED HEUSLER COMPOUNDS AND CoFeB THIN FILMS WITH PERPENDICULAR ANISOTROPY

BIELEFELD UNIVERSITY

DEPARTMENT OF PHYSICS

*Mn-based Heusler compounds and CoFeB thin films with perpendicular anisotropy*

# *Mn-based Heusler compounds and CoFeB thin films with perpendicular anisotropy*

*Thesis by Manuel Glas*

I hereby declare that the work in this thesis is my own original work, except where indicated in the text.

(Manuel Glas)

Reviewers:
Prof. Dr. Günter Reiss
Prof. Dr. Dario Anselmetti

BIELEFELD UNIVERSITY, DEPARTMENT OF PHYSICS

THIN FILMS AND PHYSICS OF NANOSTRUCTURES
CENTER FOR SPINELECTRONIC DEVICES AND MATERIALS

Ph.D. Thesis

*November 2015*

# *Abbreviations*

*AES* Auger electron spectroscopy

*AFM* atomic force microscopy

*AHE* anomalous Hall effect

*AMR* anisotropic magnetoresistance

*AR* area resistance

*BL* beamline

*CIMS* current-induced magnetization switching

*CMOS* complementary metal-oxide-semiconductor

*DOS* density of states

*DRAM* dynamic random access memory

*EAMS* electric-field-assisted magnetization switching

*FeRAM* ferroelectric random access memory

*FL* free layer

*FM* ferromagnetic

*FWHM* full width at half maximum

*GMR* giant magnetoresistance

*HDD* hard disk drive

*LM* luminescence mode

*LT* low temperature

*MDL* magnetic dead layer

*MRAM* magnetoresistive random access memory

*MTJ* magnetic tunnel junction

*OHE* ordinary Hall effect

*PCRAM* phase change random access memory

*PMA* perpendicular magnetocrystalline anisotropy

*pMTJ* perpendicular magnetic tunnel junction

*RAM* random access memory

*RL* reference layer

*rms* root mean square

*RRAM* resistive random access memory

*RT* room temperature

*SEM* scanning electron microscope

*SQUID* superconducting quantum interference device

*SRAM* static random access memory

*STT* spin-transfer torque

*TEM* transmission electron microscopy

*TEY* total electron yield

*UHV* ultra-high vacuum

*XA* x-ray absorption

*XAS* x-ray absorption spectroscopy

*XMCD* x-ray magnetic circular dichroism

*XMLD* x-ray magnetic linear dichroism

*XRD* x-ray diffraction

*XRF* x-ray fluorescence

*XRR* x-ray reflectivity

# *Nomenclature*

| | |
|---|---|
| $a$ | in-plane lattice constant |
| $A$ | atomic mass |
| $\alpha$ | Gilbert damping constant |
| $B$ | broadening of the XRD peak |
| $b$ | in-plane lattice constant |
| $\vec{B}$ | magnetic field |
| $\beta$ | x-ray absorption of a medium |
| $\chi$ | compensation factor for the Mn spin magnetic moment |
| $C$ | constant depending on the transition matrix elements |
| $c$ | out-of-plane lattice constant |
| $d$ | film thickness |
| $d_{hkl}$ | lattice plane distance |
| $\Delta$ | gap in the DOS |
| $D_{\uparrow/\downarrow}$ | density of majority/minority electrons at $E_F$ |
| $\vec{E}$ | electric field |
| $\vec{E}_b$ | bias electric field |
| $e$ | electron charge |
| $E_B$ | energy barrier |
| $E_F$ | Fermi energy |
| $E_{kin}$ | kinetic energy |
| $\varepsilon$ | strain |
| $\eta$ | post-edge jump height |
| $f_j$ | atomic scattering factor |
| $F_{hkl}$ | structure factor |
| $g$ | Lande g-factor |
| $\Gamma$ | TMR effect at 300 K to TMR effect at 15 K ratio |

$\gamma$ gyromagnetic ratio

$\vec{H}_K$ effective anisotropy field

$\vec{H}_c$ coercive field or coercivity

$\vec{H}$ magnetic field

$\vec{H}_b$ bias magnetic field

$\vec{H}_D$ demagnetization field

$\vec{H}_{\mathrm{eff}}$ effective magnetic field

$\vec{H}_{\mathrm{ext}}$ external magnetic field

$\vec{H}_s$ magnetic stray field

$\hbar$ reduced Planck constant

$(hkl)$ Miller indices

$I$ current

$\vec{I}_b$ bias current

$I_0$ zero current

$I_{hkl}$ total peak intensity

$I^{\pm}$ transmission spectra for parallel and antiparallel orientations of magnetic field and x-ray beam direction

$\vec{j}$ current density

$\vec{j}_c$ critical current density

$j$ total angular momentum quantum number

$K$ anisotropy energy

$k_B$ Boltzmann constant

$k_{||}$ in-plane wave vector

$K_S$ Scherrer or shape factor

$L$ Langevin function

$l$ azimuthal quantum number (angular momentum)

$\lambda$ wavelength of the incoming light

$m_{orb}$ orbital magnetic moment

$m_{spin}$ spin magnetic moment

$ML$ monolayer

$m^{tot}$ total magnetic moment

$\vec{M}_r$ remanence magnetization

$\vec{M}_s$ saturation magnetization or magnetization

$M$ molar mass

$\mathrm{\mu_B}$ Bohr magneton

$\mu_0$ vacuum permeability

$\mu^{\pm}$ linear XA coefficients for parallel and antiparallel orientations of magnetic field and x-ray beam direction

$N_A$ Avogadro constant

$n$ electron density

$N$ number of particles

$\tilde{n}$ complex refractive index for monochromatic x-rays

$N_h$ number of holes

$\omega_D$ Debye frequency

$p$ XMCD integral for the $L_3$ edge

$\Phi$ rotation angle

$\mathrm{\phi}_0$ magnetic flux quanta

$p$ spin polarization

$p_{h\nu}$ beam polarization

$\Psi$ tilt angle

$q$ XMCD integral for the whole range $L_3 + L_2$

$R_S$ anomalous Hall coefficient

$R_H$ ordinary Hall coefficient

$r$ XAS integral

$r_0$ Bohr radius

$R_{\uparrow\downarrow}$ MTJ resistance for antiparallel-aligned electrodes

$R_{\uparrow\uparrow}$ MTJ resistance for parallel-aligned electrodes

$\rho$ density of medium

$S_b$ background of the XAS

$s$ spin quantum number

$S$ squareness ratio

$S_{max}$ XMCD amplitude

$\sigma$ x-ray dispersion of a medium

$\vec{\tau}$ current-induced torque

$\tau$ grain size

$\tau_0$ characteristic length of time

$\tau_M$ measuring time

$\tau_N$ Néel relaxation time

$T$ temperature

$T_B$ blocking temperature

$T_\chi$ coercivity crossover temperature

$T_C$ Curie temperature

$T_N$ Néel temperature

$T_c$ transition temperature into the superconducting state

$\vartheta$ angle between two ferromagnetic layers

$\theta$ angle of incidence regarding substrate or magnetization direction

$\theta_C$ critical angle of incidence

$U$ voltage

$U_b$ bias voltage

$V^*$ electron phonon interaction

$V$ volumen of the storage layer

$Z$ nuclear charge

$\zeta$ spin-transfer efficiency

# *Contents*

# *Introduction*

In 1898 Valdemar Poulsen, inspired by the telephone, introduced the idea of magnetic recording and invented a mechanism for the read and write process of an acoustic signal. Consequently, the magnetic wire recorder is the precursor of the current magnetic recording systems. Since then a lot of investigations and improvements have been made. The first commercial computer with a moving-head hard disk drive (HDD) was the *IBM 305 RAMAC* that was shipped in 1956. The RAMAC used an inductive head for reading and writing and contains fifty disks with a diameter of 610 mm. Back then the price was \$10 000 000 /Gbyte. A great step forward was made when the anisotropic (AMR)[1] and giant magnetoresistance (GMR)[2] effects were introduced into HDD development. In 1990 the AMR head based *IBM 9345 HDD* was built with eight 130 mm disks. A GMR based head was implemented in 1997 (*IBM DTTA-351680*). Again the diameter of the HDD was further decreased to 88.9 mm (3.5 in). With the GMR effect the research area called *spintronics* entered HDD development. Spintronics is a technology that exploits both the intrinsic spin and the electric charge of an electron. The evolution of HDD was impressive, compared to the *RAMAC* the present storage density was shrunk by a factor of 20 000 and the price dropped to \$0.04 /Gbyte.

In contrast to secondary storage (HDD), primary storage is based on recording via charge carriers. Currently, *static random access memory* (SRAM) and *dynamic random access memory* (DRAM) are controlling the market. The SRAM is built up of six complementary metal-oxide-semiconductor (CMOS) transistors (flip-flop). Four of the transistors store the data in the SRAM cell, whereas the two other transistors control the read and write process. This complex structure is the reason for the larger chip area compared to DRAM cells (cf. Table 1). However, the read and write process is faster compared to the DRAM. The conventional DRAM cell is built up of a transistor and a capacitor. The lat-

[1] W. Thomson. In: *Proceedings of the Royal Society of London* (1856)

[2] M. N. Baibich et al. In: *Phys. Rev. Lett.* 61 (21 1988); G. Binasch et al. In: *Physical Review B* 39.7 (1989)

| Category | Parameter | SRAM | DRAM | MRAM |
|---|---|---|---|---|
| Cost | Cell area | 3.7 µm$^2$ | 0.56 µm$^2$ | 0.7 µm$^2$ to 1.4 µm$^2$ |
| | Process cost adder | 0 % | 25 % | 25 % |
| Performance | Read access | 3.3 ns | 13 ns | 5 ns to 20 ns |
| | Write cycle | 3.4 ns | 20 ns | 5 ns to 20 ns |
| Power | Data retention | 0.6 nA per bit at 85 °C | 0.2 nA per bit at 85 °C | 0 |
| | Read active | 15 pC per bit | 7 pC per bit | 7 pC per bit |
| | Write active | 15 pC per bit | 7 pC per bit | 45 pC per bit |
| Miscellaneous | Write endurance | Unlimited | Unlimited | Unlimited |

Table 1: Parameter values for a variety of embedded memory technologies at the 180 nm technology node.[3]

ter stores the data, whereas the transistor controls the reading and writing of data. Thus the DRAM captivates by its simple architecture. However, due to the leakage of the capacitor the information fades in a few milliseconds. Hence, a refresh cycle every 32 ms or 64 ms is needed. The advantages of the DRAM are low costs and high storage density. Drawbacks are shorter access time compared to the SRAM and the constantly required refresh cycles. Additionally, both types of RAM exhibit the main disadvantages of a volatile memory.

To overcome the obstacles of a volatile memory new attempts were made by searching for effects appropriate for data storage. The four most significant effects and their type of RAM are:

1. phase change effect (PCRAM),
2. ferroelectric effect (FeRAM),
3. resistive effect in dielectrics (RRAM), and
4. magnetoresistive effects (MRAM).

Recently, Yole Développement[4] announced that the RRAM and MRAM are the main substitutes for Flash memory and DRAM.

In the following chapters we will take a closer look at the MRAM cell and its underlying concept. The key component of an MRAM cell is the magnetic tunnel junction (MTJ) that stores the information. Analogously to the DRAM cell, a transistor controls the read and write access. The MTJ consists of two ferro(i)magnetic layers, called electrodes, separated by an insulating thin film. The electrodes are separated in a hard-magnetic layer called reference layer (RL) and in a soft-magnetic layer called free layer (FL). By applying a voltage to the MTJ electrons will tunnel from

[3] W. J. Gallagher and S. S. P. Parkin. In: *IBM Journal of Research and Development* 50.1 (2006)

[4] http://www.yole.fr

the RL over the barrier into the FL or vice versa, depending on the polarity of the current. Electrons passing the RL will be polarized along the magnetization direction of the electrode (cf. Figure 1). Therefore, a spin-polarized current is achieved. The spin is conserved during the tunneling process because the spin diffusion length is greater than the barrier thickness. If the FL exhibits the same magnetization direction as the RL the electrons will tunnel into the FL. However, if the magnetization direction of the FL is opposed to the RL direction the tunneling electrons are unable to pass through the FL. Thus the MTJ reveals low resistance in the parallel state and high resistance in the antiparallel state. Jullière[5] discovered this phenomenon named tunnel magnetoresistance (TMR) effect in 1975. The difference in resistance is based on the spin-polarized electronic structure of ferromagnets. Transition metals like Co, Fe, and Ni exhibit differences in the number of majority and minority electrons (cf. Figure 2). This leads to a spin-polarized electronic structure. An important factor for the TMR effect is the density of states (DOS) at the Fermi energy $E_F$. In case of a different DOS at $E_F$ the electrical conductance for the majority and minority electrons is divergent. This difference in the DOS is the reason for the spin-polarized current. Spin polarization $p$ is defined by $p = (D_\uparrow - D_\downarrow)/(D_\uparrow + D_\downarrow)$, where $D_{\uparrow/\downarrow}$ is the density of majority (spin up)/minority (spin down) electrons at $E_F$. Now considering an MTJ with two parallel-aligned electrodes. In this particular case, more electrons with spin up tunnel from one electrode into the other. Therefore, the spin channel for spin up electrons carries a large current, whereas the spin channel for spin down electrons carries only a small amount. If we now switch one of the electrodes into the antiparallel state, the DOS at the Fermi energy changes. Now both spin channels carry only a small amount of current and thus the resistance of the MTJ in the antiparallel state is higher. Jullière himself related the TMR effect to the spin polarizations of the electrodes, $p_1$ and $p_2$. He defined the TMR effect amplitude by $\text{TMR} = 2p_1p_2/(1+p_1p_2)$. A more commonly known definition is $\text{TMR} = (R_{\uparrow\downarrow} - R_{\uparrow\uparrow})/R_{\uparrow\uparrow}$, with $R_{\uparrow\downarrow}/R_{\uparrow\uparrow}$ being the MTJ resistance for antiparallel-/parallel-aligned electrodes.[6] As can be seen from the equation for the TMR effect, a high spin polarization is required to achieve high TMR ratios. Materials with 100 % spin polarization are called half-metallic. The half-metallic characteristic has been predicted for oxide compounds[7] like $Fe_3O_4$ and $CrO_2$, perovskites[8] like $LaSrMnO_3$, zinc-blende-type[9] CrAs, and several Heusler compounds[10].

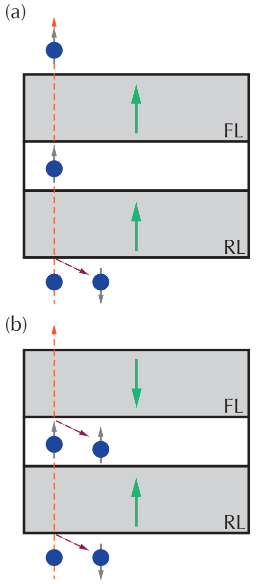

Figure 1: Schematic sketch of TMR effect in MTJ's. (a) Magnetization directions of the FL and RL are parallel. Thus, spin-polarized electrons can pass through both layers. (b) Magnetization directions are antiparallel FL (RL) does not allow electrons of spins aligned along RL (FL). Therefore, a higher electrical resistance is obtained.

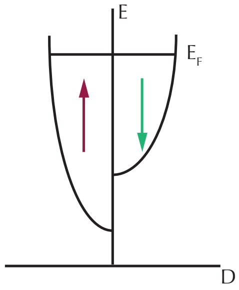

Figure 2: Density of states (DOS) of a ferromagnet.

[5] M. Jullière. In: *Physics Letters A* 54.3 (1975)

[6] A more distinct derivation is given in the first chapter.

By replacing the previously used amorphous Al–O barrier[11] by a crystalline MgO insulator[12] the TMR ratios increased drastically. The coherent tunneling induced by the MgO barrier is the main reason for the high TMR ratios. At room temperature (RT) a TMR effect of 604 % was reported by Ikeda et al.[13] in in-plane magnetized Co-Fe-B tunnel junctions. However, out-of-plane magnetized Co-Fe-B tunnel junctions achieved a TMR ratio of 124 % at RT.[14]

Nonetheless, to write information in the MRAM cell, i.e., in the MTJ, the alignment of the ferro(i)magnetic layer has to be changed. The simplest solution is an external magnetic field. Therefore, two additional conducting paths called writing lines have to be added (cf. Figure 3). By supplying a current in the writing lines a rotational magnetic field around them is induced (Ampere's law $\nabla \times \vec{B} = \mu_0 \vec{j}$)[15]. The field can manipulate the alignment of the electrodes. Due to the constant miniaturization process in spintronic devices, the magnetic field induced by the writing line becomes insufficient since the storage cell diameter decreases below micrometer size. To overcome this obstacle we have to consider Newton's third law of motion:

> *"When one body exerts a force on a second body, the second body simultaneously exerts a force equal in magnitude and opposite in direction on the first body."*

Adapted to our situation it means when the alignment of the ferro(i)magnetic layer has an impact on the current, the current has an impact on the alignment of the electrodes. The effect of current-induced magnetization switching (CIMS) is called spin-transfer torque (STT) effect and was independently predicted by Slonczewski[16] and Berger[17] in 1996. In 2004 a milestone was reached after Huai et al.[18] reported the first STT switching in $Al_2O_3$ based in-plane MTJ's. The critical current density $\vec{j}_c$ was determined to 8 MA cm$^{-2}$. Furthermore, Meng et al.[19] reported STT switching in Co-Fe-B based perpendicular magnetic tunnel junctions (pMTJ's). They obtained a critical current density of 2.1 MA cm$^{-2}$. Before we discuss the possibilities of lowering $\vec{j}_c$, we will take a closer look at the STT effect itself. For this reason, we are going to start with a typical MTJ structure, the bottom layer is the RL fixed during the entire process. The top layer is the FL, which will change its direction when a voltage is applied (cf. Figure 4). The more illustrative process is from the antiparallel state into the parallel state. By applying a voltage randomly-polarized electrons passing the RL will be polarized in the direction of the

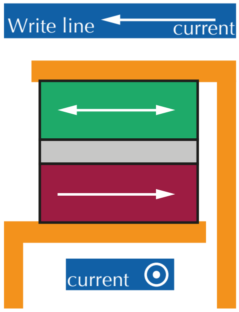

Figure 3: Schematic sketch of an MRAM device with two separate writing lines for magnetization switching.

---

[7] X. W. Li et al. In: *Applied Physics Letters* 73.22 (1998); J. M. D. Coey and M. Venkatesan. In: *Journal of Applied Physics* 91.10 (2002)

[8] W. E. Pickett and J. S. Moodera. In: *Physics Today* 54.5 (2001)

[9] H. Akinaga et al. In: *Japanese Journal of Applied Physics* 39.11B (2000)

[10] R. A. de Groot et al. In: *Physical Review Letters* 50.25 (1983)

[11] J. S. Moodera et al. In: *Physical Review Letters* 74.16 (1995)

[12] S. S. P. Parkin et al. In: *Nature Materials* 3.12 (2004)

[13] S. Ikeda et al. In: *Applied Physics Letters* 93.8 (2008)

[14] S. Ikeda et al. In: *Nature Materials* 9.9 (2010)

[15] Where $\vec{B}$ denotes the magnetic field, $\mu_0$ the vacuum permeability and $\vec{j}$ the current density.

[16] J. C. Slonczewski. In: *Journal of Magnetism and Magnetic Materials* 159 (1996)

[17] L. Berger. In: *Physical Review B* 54.13 (1996)

[18] Y. Huai et al. In: *Applied Physics Letters* 84.16 (2004)

RL magnetization. Now the electrons reach the FL, due to the soft-magnetic properties the spin carried by the electrons exerts a torque on the magnetization and switches its direction into the parallel state. The change of the magnetization direction from the parallel into the antiparallel state is more complex. For this purpose, the polarity of the voltage has to be changed so that electrons pass through the FL first. The temperature of the MTJ increases due to the applied voltage, whereas the temperature increment depends on the pulse duration. Thermal fluctuations cause a tilt by a small angle of the magnetization direction. Thus the direction of the FL is not perfectly parallel to the RL. The passing electrons will be polarized and tunnel through the barrier. When the electrons reach the RL they will be reflected and the spin polarization changes in the opposite direction. These electrons exert a torque on the FL and change its direction into the antiparallel state.[20]

The first STT-MRAM devices were already produced by Everspin[21] and Toshiba[22]. The latter reported a test chip that consumes 80 % less power than an SRAM chip. To further extend its applicability $\vec{j}_c$ needs to be lowered. The critical current density is defined as

$$\vec{j}_c = \frac{2\alpha e}{\hbar\zeta}\vec{M}_s d(\vec{H}_K^{\parallel} \pm \vec{H}_{\text{ext}} \pm \vec{H}_D), \tag{1}$$

where $e$ denotes electron charge, $\alpha$ the damping constant, $\vec{M}_s$ saturation magnetization, $d$ the thickness of the ferro(i)magnetic electrode, $\hbar$ the reduced Planck constant, $\vec{H}_{\text{ext}}$ is the external field, $\vec{H}_K$ is the effective anisotropy field including magnetocrystalline anisotropy and shape anisotropy, $\vec{H}_D$ is the demagnetization field, and $\zeta$ is the spin-transfer efficiency

$$\zeta = \frac{p}{2(1 + p^2\cos(\vartheta))}, \tag{2}$$

where $p$ denotes the spin polarization and $\vartheta$ the angle between the two ferromagnetic layers. The demagnetization field $\vec{H}_D$ depends on the magnetization orientation. For in-plane magnetized materials $\vec{H}_D = \mu_0\vec{M}_s/2$ holds. Out-of-plane magnetized materials usually reveal a higher anisotropy energy than in-plane magnetized materials, thus $\vec{H}_D$ can be reduced to $-\vec{M}_s$. The anisotropy energy is given by the following Equation

$$K = \frac{\vec{M}_s\vec{H}_K}{2}. \tag{3}$$

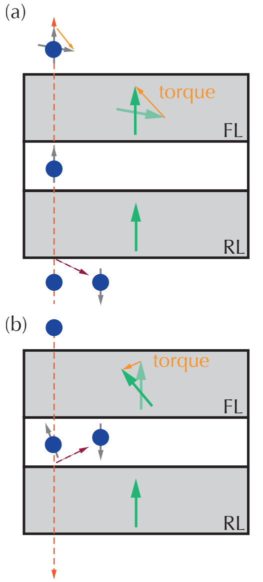

Figure 4: Schematic sketch of the STT effect. (a) To achieve the parallel state electrons tunnel from the RL into the FL. (b) Electrons tunneling from the FL into the RL favor the antiparallel state.

---

[19] H. Meng et al. In: *Journal of Physics D: Applied Physics* 44.40 (2011)

[20] A more distinct derivation will be given in the last chapter.

[21] http://www.everspin.com

[22] http://www.toshiba.co.jp

In order to lower $\vec{j}_c$, the following requirements should be fulfilled:

1. low magnetic damping $\alpha$
2. high spin polarization $p$
3. low magnetization $\vec{M}_s$
4. small element size $d$
5. low anisotropy field $\vec{H}_K$

The last item cannot be realized, due to the criterion for a 10-year non-volatility

$$KV > 60k_BT \tag{4}$$

with $V$ the volume of the storage (free) layer, $k_B$ the Boltzmann constant, and $T$ the temperature. Because of the intended decrease of $V$, $K$ has to be increased, in order to retain the data stored in the memory for more than ten years.

A FIRST ATTEMPT would be to search for new materials that fulfill these basic requirements. Magnetic materials with an easy magnetization axis parallel to the surface are unsuitable for the intended miniaturization process in spintronic devices. Due to the lower anisotropy energy, compared to out-of-plane magnetized materials, the superparamagnetic limits are reached. Additionally, a lower storage density could be obtained for in-plane magnetized ferro(i)magnets.

A new material class that shows promising characteristics are Mn-based tetragonally distorted Heusler compounds with an easy magnetization axis pointing perpendicular to the film plane. The most promising materials are $\mathrm{Mn_{3\text{-}x}Ga}$, $\mathrm{Mn_{3\text{-}x}Co_xGa}$, and $\mathrm{Mn_{3\pm x}Ge}$. Two interesting crystallographic phases are the $L1_0$ and $D0_{22}$ structures for the $\mathrm{Mn_{3\text{-}x}Ga}$ compound and the $D0_{22}$ phases for $\mathrm{Mn_{3\text{-}x}Co_xGa}$ and $\mathrm{Mn_{3\pm x}Ge}$ (cf. Figures 5 and 6). These compounds also reveal a high Curie temperature $T_C$, which is required for spintronic devices. Nonetheless, the investigation of new materials contains the following questions and risks:

- preparation method acceptable for industrial application
- crystallization in the intended phase possible in thin films
- coherent interfaces between the ferromagnet and the barrier material

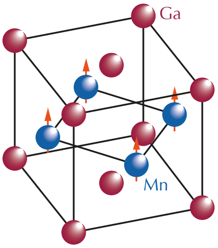

Figure 5: Schematic sketch of the $L1_0$ phase for the Mn-Ga compound.

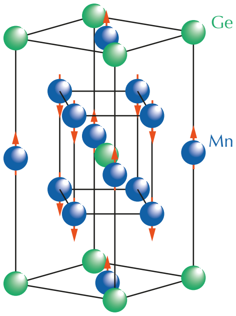

Figure 6: Schematic sketch of the $D0_{22}$ phase for the $\mathrm{Mn_{3\pm x}Ge}$ compound.

- low roughness of the bottom layer
- suppressed formation of oxide at the barrier interface

The sputter deposition of $Mn_{3\text{-}x}Ga$ requires a Mn-Ga composite target, due to the low melting point of Ga (28.9 °C). A question would be if the stoichiometry of the target is constant over time or if the Ga volatilizes. Another point is the oxidation of Mn at the barrier interface. In-plane-magnetized Mn-based Heusler compounds like $Co_2MnSi$ are known for the formation of Mn–O when in contact with an MgO barrier.[23]

To overcome the remaining questions above, further investigations of known materials, like $Co_{40}Fe_{40}B_{20}$, are promising. Here, the preparation conditions are simple and the material properties are well understood. $Co_{40}Fe_{40}B_{20}$ is a ferromagnetic (FM) material that exhibits an out-of-plane magnetization direction for film thicknesses below 1.5 nm.[24] A crucial aspect to achieve a perpendicular magnetocrystalline anisotropy (PMA) is the deposition of an MgO layer next to the Co-Fe-B film. Thus hybridization of the $2p$ orbitals of the O and the $3d$ orbitals of the Co-Fe is obtained which results in an out-of-plane magnetization direction. During the post-annealing process the B diffuses away from the barrier. Thus a clean Co-Fe interface with high spin polarization arises. Furthermore, Co-Fe-B based MTJ's with CIMS were already reported by several groups.[25] Instead of searching for new materials with appropriate properties a temporary variation, for example of the anisotropy energy $K$, could lead to a low $\vec{j}_c$. This can be accomplished by an external electric field $\vec{E}$.[26] If the ferromagnetic electrode is thin enough an external field $\vec{E}_b$, induced by a high voltage over the barrier, leads to a depletion or accumulation of charge carriers at the barrier interface.[27] The loss of charge carriers results in a higher coercive field $\vec{H}_c$, whereas the gain of electrons results in a lower $\vec{H}_c$. This effect can be used for STT switching, while lowering $K$ with a high voltage pulse, a secondary current can switch the magnetization direction.[28] Thus surprisingly low critical current densities can be achieved. This $\vec{E}$-field effect is promising for STT-MRAM devices with low power consumption.

In this work we investigated different Mn-based, tetragonally distorted Heusler compounds. We analyzed the magnetic, crystallographic, and surface properties of the Heusler thin films. We are going to describe the optimization of the Heusler film to

[23] J. Schmalhorst et al. In: *Physical Review B* 75.1 (2007)

[24] S. Ikeda et al. In: *Nature Materials* 9.9 (2010)

[25] S. Ikeda et al. In: *Nature Materials* 9.9 (2010); H. Meng et al. In: *Journal of Physics D: Applied Physics* 44.40 (2011)

[26] H. Ohno et al. In: *Nature* 408.6815 (2000)

[27] W. G. Wang et al. In: *Nature Materials* 11.1 (2011)

[28] S. Kanai et al. In: *Applied Physics Letters* 104.21 (2014)

achieve highly oriented epitaxial growth, low surface roughness, low magnetic moment and a high anisotropy constant. Furthermore, the interface between the respective bottom electrode and the MgO barrier was investigated by element-specific, surface-sensitive x-ray absorption spectroscopy (XAS) and x-ray magnetic circular dichroism (XMCD). Additionally, we analyzed the impact of a metallic TiN buffer layer on the properties of the $Mn_{3-x}Ga$ compound. We investigated the transport properties of full MTJ's between 15 K and 300 K. Auger electron spectroscopy (AES) measurements were carried out in order to determine the interdiffusion in MTJ's.

Beyond the exploration of new materials we investigated commonly known $Co_{40}Fe_{40}B_{20}$ based pMTJ's. We prepared full MTJ stacks with different MgO barrier thicknesses. Transport measurements were carried out between 15 K and 330 K. The transport properties will be discussed in terms of temperature and bias voltage dependence. The variation of the PMA in presence of an $\vec{E}_b$-field will be examined. This effect will be used in an $\vec{E}$-field-supported, $\vec{H}$-field-induced switching mode.

# *The binary Mn-Ga compound*

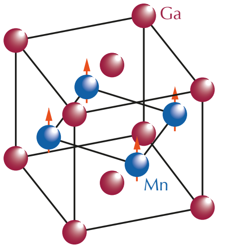

Figure 7: Schematic sketch of the $L1_0$ phase for the Mn-Ga compound.

*In this chapter the preparation of $Mn_{3-x}Ga$ ($1.5 \leq x \leq 0.1$) thin films with perpendicular magnetic anisotropy will be laid out. Different compositions were prepared and studied with respect to their crystallographic and magnetic properties. Accordingly, the interface was studied in relation to the formation of Mn–O. The surface roughness was examined due to the intended integration into magnetic tunnel junctions. Further, we investigated the applicability of $Mn_{3-x}Ga$ thin films in magnetic tunnel junctions. In the last section of this chapter the impact of a TiN seed layer on the $Mn_{3-x}Ga$ properties will be analyzed.*

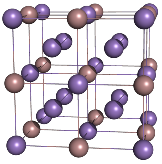

Figure 8: Cubic $D0_3$ structure of $Mn_{3-x}Ga$.

## *Stoichiometry dependence of Mn-Ga*

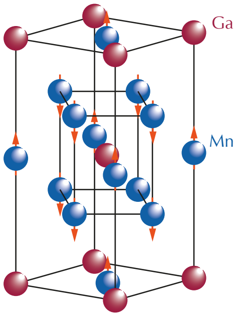

Figure 9: Schematic sketch of the $D0_{22}$ phase for the $Mn_{3-x}Ga$ compound.

The binary $Mn_{3-x}Ga$ compound exists in different crystallographic structures. The four commonly known are: the tetragonal $L1_0$, the cubic $D0_3$, the tetragonal $D0_{22}$, and the hexagonal $D0_{19}$ (cf. Figures 8 to 9). To achieve the respective phases the deposition temperature and composition have to be adjusted. Each crystal structure shows different magnetic properties. A distinction is drawn between phases with in-plane magnetization direction and out-of-plane magnetization direction. The in-plane magnetized $D0_3$ phase of $Mn_3Ga$ is unstable but predicted to be a half-metallic, fully compensated ferrimagnet.[29] However, the more interesting crystal structures for pMTJ's are the two tetragonally distorted $L1_0$ and $D0_{22}$ phases. The $L1_0$ (CuAu) type phase could be obtained for Mn concentration below 65 at % ($Mn_{1.8}Ga$) after annealing at 400 °C.[30] In case of a $Mn_1Ga_1$ compound a ferromagnetic order is present with a magnetic moment of $2.5\,\mu_B$ per Mn atom.[31] By increasing the Mn concentration, the additional atoms occupy the Ga positions and couple antiferromagnetically with the Mn atoms at the initial positions. This antiferromagnetic coupling results in partial compensation of the magnetic moments. For $Mn_{1.27}Ga$ a magnetic moment per Mn atom of $1.7\,\mu_B$ was determined.[32]

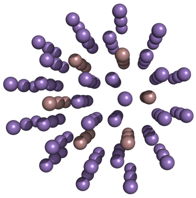

Figure 10: Hexagonal distorted $D0_{19}$ phase of $Mn_{3-x}Ga$.

[29] S. Wurmehl et al. In: *Journal of Physics: Condensed Matter* 18.27 (2006)

The in-plane and out-of-plane lattice constants for MnGa are reported to be $a$, $b = 3.897\,\text{Å}$ and $c = 3.625\,\text{Å}$. An increasing Mn content lead to a decreasing $c$ axis. The anisotropy constant was determined to be $K = 2.6 \times 10^6\,\text{J}\,\text{m}^{-3}$.[33] A low magnetic damping of $\alpha = 0.008$ was reported for $\text{Mn}_{1.54}\text{Ga}$ by Mizukami et al.[34] Furthermore, Zhu et al.[35] reported a theoretical spin polarization of 71 %.

In order to achieve the tetragonally distorted $D0_{22}$ ($\text{Al}_3\text{Ti}$) structure, a Mn concentration between 66 at % and 74 at % is required and the sample has to be annealed at 450 °C.[36] The crystallographic $D0_{22}$ structure is similar to the $L1_0$ phase, with the bulk lattice constants $a = 3.9049\,\text{Å}$ and $c = 7.1724\,\text{Å}$ ($2c_{L1_0} \approx c_{D0_{22}}$) for $\text{Mn}_{2.03}\text{Ga}$. The magnetic moments are $m_I = 2.8\,\mu_\text{B}$ and $m_{II} = -1.6\,\mu_\text{B}$ on the Wyckoff positions $2b$ and $4d$, respectively. The negation indicates the antiferromagnetic coupling of the sublattices.[37] By increasing the Mn content a lower total magnetic moment is achieved due to compensation. Furthermore, the additional Mn atoms lead to a decrease of the $c$ lattice plane, whereas the $a$,$b$ plane remains almost unaltered.[38] A Curie temperature of 770 K for $\text{Mn}_{2.03}\text{Ga}$ was reported by Niida et al.[39] In case of a higher Mn concentration ($\text{Mn}_{2.57}\text{Ga}$) the $D0_{22}$ starts to decompose at 770 K. The decomposition results in an irreversible decrease of magnetization. Therefore the Curie temperature is evidently higher. Winterlik et al.[40] reported a theoretical estimated spin polarization of 88 % for $\text{Mn}_3\text{Ga}$. A spin polarization of 58 % was determined via point-contact Andreev reflection by Kurt et al.[41] for $\text{Mn}_3\text{Ga}$. Mizukami et al.[42] reported a low magnetic damping of $\alpha = 0.015$ and a high anisotropy constant of $K = 1.5 \times 10^6\,\text{J}\,\text{cm}^{-2}$ for $\text{Mn}_{2.12}\text{Ga}$ thin films.

The reported properties of both tetragonally distorted phases, $L1_0$ and $D0_{22}$, make them promising candidates to serve as electrodes in MTJ's. Especially, the low magnetic moment, low magnetic damping, high spin polarization and high anisotropy constant increase their applicability in STT-MRAM.

IN A FIRST ATTEMPT WE INVESTIGATED VARIOUS $\text{Mn}_{3\text{-x}}\text{Ga}$ compositions. Our samples were prepared in an ultra-high vacuum (UHV) Bestec co-deposition sputtering tool. The variation in the stoichiometry was obtained by co-sputtering from a Mn-Ga composite target and a Mn target.[43] By changing the power applied to the Mn target, different compositions were achieved. The thin films were deposited on (001) $\text{SrTiO}_3$ ($a_{\text{SrTiO}_3} = 3.905\,\text{Å}$) and (001) MgO ($a_\text{MgO} = 4.21\,\text{Å}$) substrates, due to low lattice mis-

[30] H. Niida et al. In: *Journal of Applied Physics* 79.8 (1996)

[31] A. Sakuma. In: *Journal of Magnetism and Magnetic Materials* 187.1 (1998)

[32] M. Hasegawa and I. Tsuboya. In: *Journal of the Physical Society of Japan* 20 (1965)

[33] A. Sakuma. In: *Journal of Magnetism and Magnetic Materials* 187.1 (1998)

[34] S. Mizukami et al. In: *Physical Review Letters* 106.11 (2011)

[35] L. J. Zhu et al. In: *Applied Physics Letters* 102.13 (2013)

[36] H. Niida et al. In: *Journal of Applied Physics* 79.8 (1996); H. Niida et al. In: *Journal of the Physical Society of Japan* 52.5 (1983)

[37] H. Niida et al. In: *Journal of Applied Physics* 79.8 (1996); J. Winterlik et al. In: *Physical Review B* 77.5 (2008)

[38] J. Winterlik et al. In: *Physical Review B* 77.5 (2008)

[39] H. Niida et al. In: *Journal of Applied Physics* 79.8 (1996)

[40] J. Winterlik et al. In: *Physical Review B* 77.5 (2008)

[41] H. Kurt et al. In: *Physical Review B* 83.2 (2011)

[42] S. Mizukami et al. In: *Physical Review Letters* 106.11 (2011)

[43] Three composite targets were used with different Mn-Ga stoichiometries.

match and common usage (cf. Table 2). The different deposition temperatures ranged from 520 °C to 595 °C.[44] To achieve equal preparation conditions for our samples, the heating and cooling rates were equal and the nominal film thickness ranged from 20 nm to 40 nm. On top a 2.3 nm thick MgO film was sputter deposited or e-beam evaporated to prevent the stack from oxidizing. In this way, we were able to investigate the influence of an MgO barrier on the Mn-Ga. The Ar pressure during the deposition was set to $1.3 \times 10^{-3}$ mbar. The base pressure ranged from $2 \times 10^{-8}$ mbar to $5 \times 10^{-10}$ mbar, here $5 \times 10^{-10}$ mbar is the lower limit of the vacuum gauge.

| buffer | mismatch |
|---|---|
| $SrTiO_3$ | 0.12 % |
| MgO | 7.13 % |
| Pt | 0.26 % |
| Pd | 0.51 % |
| Cr* | 3.93 % |

Table 2: Mismatch between $Mn_{3-x}Ga$ and various substrates/buffer layer. * for a 45 deg rotated film growth.

The properties of the $Mn_{3-x}Ga$ thin films were obtained by the following measuring techniques: x-ray fluorescence (XRF) measurements to determine the stoichiometry, x-ray reflectivity (XRR) and atomic force microscopy (AFM) were used to investigate the surface roughness since it is important for later performance of MTJ's, x-ray diffraction (XRD) measurements were carried out to identify the crystal structure and the magnetic properties were investigated by a superconducting quantum interference device (SQUID)[45]. In order to gain insight into the chemical properties at the $Mn_{3-x}Ga$/MgO interface, x-ray absorption spectroscopy (XAS) and x-ray magnetic circular dichroism measurements (XMCD) were carried out. Finally, temperature dependent transport measurements were performed on $Mn_{3-x}Ga$ based MTJ's with different counter electrodes.

## *X-ray fluorescence measurements*

As mentioned above, a change in the stoichiometry was achieved by co-sputtering from different composite targets and a Mn target. Three Mn-Ga composite targets were available:

1. $Mn_{45}Ga_{55}$ to achieve the $L1_0$ structure,
2. $Mn_{50}Ga_{50}$ to obtain the $L1_0$ and $D0_{22}$ structure[46], and
3. $Mn_{60}Ga_{40}$ to realize the $D0_{22}$ crystal phase.

We determined the stoichiometry via XRF measurements, performed with a Philips X'pert pro diffractometer. A copper anode that emits a wavelength of $\lambda = 1.540\,56$ Å (Cu $K_{\alpha_1}$) was used. The sample was placed in a He atmosphere. The observed stoichiometries are displayed in Table 3.[47] By comparing the results obtained one recognizes a small discrepancy between layers on MgO and on $SrTiO_3$, the Mn concentration of thin films on MgO

---

[44] Differences in the deposition temperature, due to Bestec heater modification.

[45] Measurements were carried out at the Max-Planck-Institute for Chemical Physics of Solids, Dresden

[46] due to composition variation over time

[47] In what follows we will only refer to the first decimal place of the stoichiometry.

| stoichiometry | crystal phase | sputtering method | temperature | substrate |
|---|---|---|---|---|
| $Mn_{1.50(8)}Ga$ | $L1_0$ | $Mn_{45}Ga_{55}$ | 550 °C | $SrTiO_3$ |
| $Mn_{1.60(6)}Ga$ | $L1_0$ | $Mn_{45}Ga_{55}$ | 550 °C | MgO |
| $Mn_{1.63(6)}Ga$ | $L1_0$ | $Mn_{50}Ga_{50}$ | 520 °C | $SrTiO_3$ |
| $Mn_{1.82(5)}Ga$ | $L1_0$ | $Mn_{45}Ga_{55}$ + Mn (40 W) | 520 °C | $SrTiO_3$ |
| $Mn_{2.13(3)}Ga$ | $D0_{22}$ | $Mn_{45}Ga_{55}$ + Mn (40 W) | 520 °C | MgO |
| $Mn_{2.29(4)}Ga$ | $D0_{22}$ | $Mn_{45}Ga_{55}$ + Mn (80 W) | 520 °C | $SrTiO_3$ |
| $Mn_{2.45(16)}Ga$ | $D0_{22}$ | $Mn_{60}Ga_{40}$ | 595 °C | $SrTiO_3$ |
| $Mn_{2.83(7)}Ga$ | $D0_{22}$ | $Mn_{60}Ga_{40}$ | 550 °C | MgO |

Table 3: Overview of the prepared samples and their crystallographic phase. The method describes the preparation process, sputtered from a composite target or sputtered from a composite target and an additional Mn target. The stoichiometry was investigated by XRF measurements.

was higher compared to thin films on $SrTiO_3$. One reason for this composition deviation could be different sticking coefficients for Mn or Ga on the substrates. To determine the sticking coefficients, thin films of different thicknesses have to be deposited at various temperatures. However, another plausible cause could be found in the measurement principle. XRF measurements are based on the photoionisation of an electron from an inner core shell. An electron from a higher core level fill the created hole under emission of a light quantum with an energy equal to the recombination energy. In addition, the light quantum emitted could excite an Auger electron. The recombination probability of an outer-shell or valence electron with an inner-shell hole is proportional to the square of the nuclear charge $Z^2$. Therefore, the efficiency of luminescence is rather low for materials with small $Z$. For light elements $Z < 30$ with binding energies below 2 keV the Auger process dominates the fluorescence process. Table 4 shows the electron binding energies of the $K\,1s$ core shell of the el-

| element | energy $K\,1s$ |
|---|---|
| Mn | 6.539 keV |
| Ga | 10.367 keV |
| Mg | 1.303 keV |
| Sr | 16.105 keV |
| Ti | 4.966 keV |

Table 4: Electron binding energies of different elements in their natural forms.

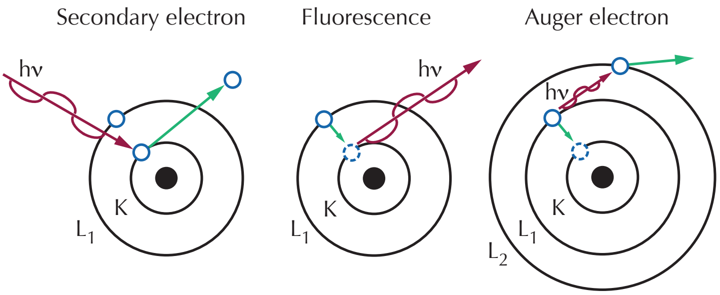

Figure 11: Illustration of a) photoemission, b) fluorescence, and c) Auger process.

ements used. Mg exhibits the lowest binding energy of 1.303 keV, thus the Auger process dominates over the luminescence process. However, the energy of an Auger electron is not high enough to excite an electron from the Mn inner-core shell. Despite the Auger electron, the secondary electron from the initial excitation could lead to ionization of additional Mn atoms. With an incident photon energy of 35 keV and a binding energy of 1.303 keV, the resulting energy of the secondary electron is high enough to excite additional atoms. This is also the case for secondary electrons of the $SrTiO_3$ substrate, but perhaps the probability of excitations by secondary electrons from Sr or Ti is lower compared to MgO substrates. Furthermore, the penetration length for XRF is around 1 μm. Thus the substrate plays an important role for thin films in the nm regime. To reduce the errors caused by impurities in the substrate, the thin film should have a thickness of at least 100 nm. By preparing a sample with a sufficient thickness the discrepancy caused by the sticking coefficient and the impurities in the substrate should be negligible. Therefore, a plausible explanation of the different $Mn_{3\text{-}x}Ga$ compositions on MgO and $SrTiO_3$ is the low nominal film thickness. In the further discussion will we only refer to the stoichiometry of the $Mn_{3\text{-}x}Ga$ thin films on $SrTiO_3$, except where indicated in the text.

The target stoichiometry showed strong variation over time, i.e., the composition was different at each sputtering time. Ga melts at 28.9 °C, during sputtering the target exceeds this temperature. Therefore, it is plausible that the Ga in the target vaporizes and the Mn concentration increases. Quite on the contrary, XRF measurements revealed that the Mn to Ga ratio decreased, i.e., the

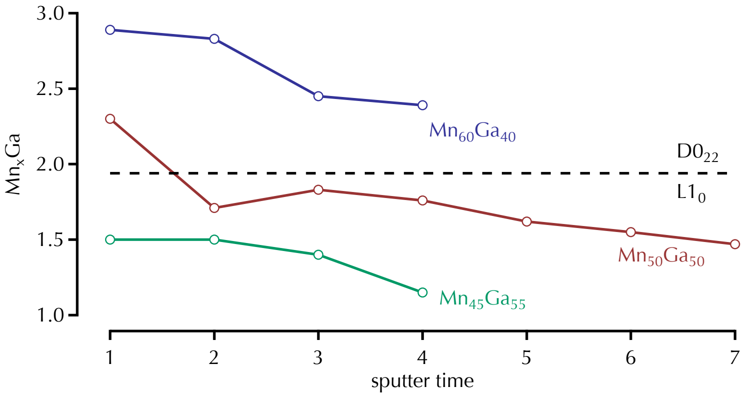

Figure 12: Illustration of target concentration variation over time for $Mn_{3\text{-}x}Ga$ thin films on MgO and $SrTiO_3$.

Mn concentration decreased. However, it cannot be ruled out that the amount of Ga also decreased. In Figure 12 the composition change over time is displayed. All samples were deposited on $SrTiO_3$ substrates and revealed thicknesses of around 30 nm. The composition of the $Mn_{60}Ga_{40}$ target changed in a range where the $D0_{22}$ phase is still obtainable. The composition of the $Mn_{50}Ga_{50}$ target started in the $D0_{22}$ regime and ended in the $L1_0$ regime. The $Mn_{45}Ga_{55}$ target remained in the $L1_0$ composition range. Therefore, the fabrication of thin films with the same stoichiometry could only be obtained by co-deposition with a Mn target. However, this lowers the applicability and involves obstacles that will be discussed in the next subsection, *x-ray reflectivity investigations*.

## *X-ray reflectivity investigations*

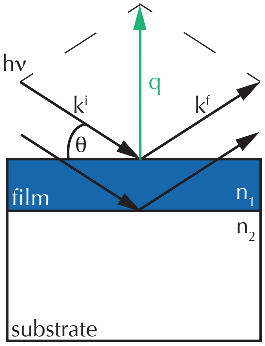

Figure 13: XRR measurement sketch. With $n_{1,2}$ the refractive index of the thin film and substrate and $\theta$ the angle of the incoming x-ray beam.

After gaining insight into the composition of our thin films, we determined the respective layer thickness and thus the deposition rate of the target. Therefore, interface sensitive XRR measurements were carried out. This measurement technique is based on the reflection of an incoming x-ray at the sample interfaces. The resulting interference of the outcoming, i.e., reflected x-rays provides information about the film thickness. The major advantages of this measuring method are its non-destructivity and its applicability to amorphous materials as long as the interfaces are distinct enough. The angle of incidence $\theta$ is between 0 deg and 5 deg. The complex refractive index for monochromatic x-rays is smaller than one and given by

$$\tilde{n} = 1 - \sigma + i\beta, \tag{5}$$

with $\sigma$ the dispersion and $\beta$ the absorption of the medium. For x-rays $\sigma$ and $\beta$ are in the range of $10^{-5}$ and $10^{-6}$, respectively. In the small angle regime a total reflection of the x-ray is observed. After overcoming a critical angle $\theta_C$ the x-ray penetrates the sample surface and is reflected at the interface between film and substrate. The critical angle $\theta_C$ is element-specific and provides information about the density of the respective film.[48] By applying the Snellius law and the approximation

$$1 - \sigma = \cos\theta_C \approx 1 - \frac{\theta_C^2}{2}, \tag{6}$$

we get the following relation for $\theta_C$

$$\theta_C \approx \sqrt{2\sigma}. \tag{7}$$

---

[48] By neglecting absorption ($\beta = 0$)

Furthermore, the relation between dispersion and density can be specified by looking at the coupling between the outer electrons and the high-frequency excitation of the x-rays. Thus the following relation for the density $\rho$ can be determined

$$\rho \approx \frac{2\pi M\sigma}{r_0 N_A Z\lambda} \tag{8}$$

where $M$ denotes the molar mass, $Z$ the atomic number, $r_0$ the Bohr radius, $N_A$ the Avogadro constant and $\lambda$ the wavelength of the incoming light. As already mentioned above, after the angle of the incoming light exceeds $\theta_C$ the x-ray penetrates the sample and is reflected at the film/substrate interface. The reflected beam at the film/substrate interface interferes with the reflected beam on the surface. The number of oscillations provides information about the film thickness $d$. We will consider the Blanton relation, that is given by

$$d = \frac{\lambda(m-n)}{2(\sin(\theta_m) - \sin(\theta_n))} \tag{9}$$

where $\theta_m$ and $\theta_n$ denote the $m^{th}$ and $n^{th}$ maxima or minima of the oscillations. The decrease of intensity depends on the surface or interface roughness.[49] The x-ray undergoes a diffuse reflexion on the rough surface or interface which lowers the reflected intensity.[50] Even in multilayer structures the respective film roughness could be examined. To obtain these data, the XRR scan is fitted numerically with the Parratt[51] formalism. With this formalism the fitting of multiple layers is also possible.

In Figure 14 XRR scans of $Mn_{3\text{-}x}Ga$ thin films on $SrTiO_3$ and

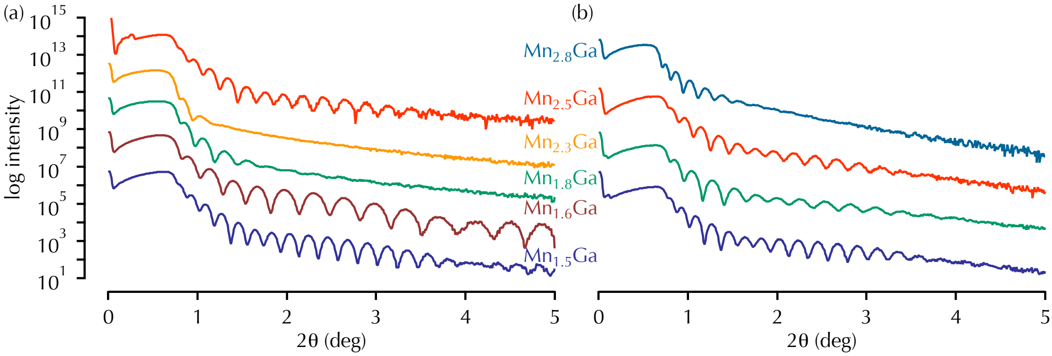

Figure 14: XRR data of different $Mn_{3\text{-}x}Ga$ thin films deposited on (a) $SrTiO_3$ and (b) MgO substrates. The samples that were prepared under same conditions have the same color. The depositions conditions can be found in Table 3. It has to be mentioned that the $Mn_{1.6}Ga$ thin film on $SrTiO_3$ (red curve) has an additional 0.8 nm thick $Co_{40}Fe_{40}B_{20}$ interlayer.

[49] Here the interface between film and substrate is referred to as interface.

[50] L. Spieß et al. Vol. 2. Vieweg+ Teubner, Wiesbaden, 2005

[51] L. Parratt. In: *Physical Review* 95.2 (1954)

| stoichiometry | thickness (nm) | roughness (nm) | density ($g\,m^{-3}$) | substrate |
|---|---|---|---|---|
| $Mn_{1.5}Ga$ | 36.28(5) | 0.89(5) | 7.20(5) | $SrTiO_3$ |
| $Mn_{1.5}Ga$ | 35.90(5) | 1.00(5) | 7.30(5) | MgO |
| $Mn_{1.6}Ga$ | 22.98(5) | 0.51(5) | 6.90(5) | $SrTiO_3$ |
| $Mn_{1.8}Ga$ | 25.73(5) | 1.27(5) | 7.02(5) | $SrTiO_3$ |
| $Mn_{1.8}Ga$ | 27.49(5) | 0.95(5) | 7.17(5) | MgO |
| $Mn_{2.3}Ga$ | 24.40(5) | 2.21(5) | 6.72(5) | $SrTiO_3$ |
| $Mn_{2.5}Ga$ | 33.47(5) | 0.99(5) | 7.10(5) | $SrTiO_3$ |
| $Mn_{2.5}Ga$ | 33.04(5) | 0.60(5) | 7.20(5) | MgO |
| $Mn_{2.8}Ga$ | 39.10(5) | 2.16(5) | 5.80(5) | MgO |

Table 5: Obtained film thickness, film roughness and density of $Mn_{3\text{-}x}Ga$ samples on $SrTiO_3$ and MgO substrates by fitting the XRR scans via the Parratt algorithm (cf. Figure 14).

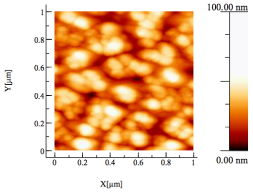

Figure 15: AFM picture of a $Mn_{2.4}Ga$ thin film on a $SrTiO_3$ substrate. The deposition temperature was set to 550 °C. The rms roughness obtained was about 15 nm.

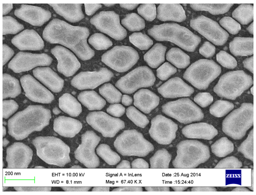

Figure 16: SEM picture of a $Mn_{2.4}Ga$ thin film on a $SrTiO_3$ substrate. The deposition temperature was set to 595 °C.

MgO substrates are depicted. Here, a comparison between samples deposited by co-deposition and deposited from only a composite target is made. A qualitative look shows a higher roughness for samples prepared by co-deposition. The respective thin film thicknesses, roughnesses and densities are listed in Table 5. The film thicknesses are between 20 nm and 40 nm. The important characteristic is film roughness. To enable STT switching in MTJ's the MgO barrier thickness needs to be decreased to below 1 nm. For this reason, a bottom layer with roughness above 1 nm reduces the applicability of the MTJ, due to pinholes through the barrier. The obtained data show an increase in Mn-Ga film roughness with increasing power applied to the Mn sputtering target. For $Mn_{2.3}Ga$, the roughness is 2.2 nm and therefore higher as the barrier thickness for STT-MTJ's. Hence, the co-deposition method is inappropriate for obtaining higher Mn concentrations. To overcome this obstacle a composite target with higher Mn concentration ($Mn_{60}Ga_{40}$) was used. The film roughness could be reduced below 1 nm for $Mn_{2.5}Ga$ thin films. Consequently, the integration of thin films from a composite target into MTJ's is promising, even when the barrier thickness is decreased to enable STT switching.

After several sputter times, the above-mentioned stoichiometry variation of the composite targets led to an island like growth of the Mn-Ga thin films. AFM measurements revealed a root mean square (rms) surface roughness of about 15 nm for a thin film deposited at 550 °C from the $Mn_{60}Ga_{40}$ target on $SrTiO_3$. In addition, a scanning electron microscope (SEM) picture of an analogous sample deposited at 595 °C is illustrated in Figure 16. The determined film stoichiometry was $Mn_{2.39(9)}Ga$. Thus the composition of the target changed and the roughness of the prepared thin film increased. Because of the island growth it was not possible to determine a roughness value from the XRR measurements. This stoichiometry variation and the increasing surface roughness are crucial obstacles in the preparation of Mn-Ga based MTJ's.

## X-ray diffraction analysis

The crystallographic structure of the $Mn_{3\text{-}x}Ga$ samples was investigated via x-ray diffraction (XRD) measurements, realized by a Philips X'pert pro diffractometer (Cu $K_\alpha$ $\lambda = 1.5419$ Å). To investigate polycrystalline samples the Bragg-Brentano configuration ($\theta/2\theta$) was used (cf. Figure 17). In comparison to x-ray reflection, the x-ray diffraction occurs at higher angles and is based on the diffraction of the incoming x-ray in the lattice. An incident beam emitted from a copper anode is scattered from the atoms of the material. The constructive interference can be described by Bragg's law[52]:

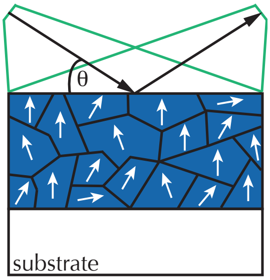

Figure 17: Bragg Brentano measurement setup. The arrows indicate the growth directions of the crystallites, i.e., the grains.

$$n\lambda = 2d_{hkl}\sin\theta \tag{10}$$

with $n$ an integer number, $\lambda$ the x-ray radiation wavelength, $d_{hkl}$ the lattice plane distance and $\theta$ the angle between incident beam and lattice plane. Figure 18 shows the reflection of incident x-rays on two neighboring lattice planes, separated by a distance $d_{hkl}$. The path difference is $2d_{hkl}\sin\theta$. With an angle of constructive interference $\theta$ the plane distance is given by

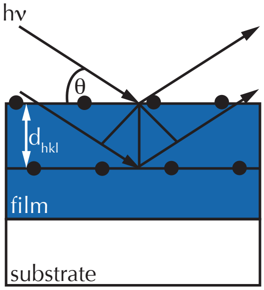

Figure 18: XRD measurement sketch.

$$d_{hkl} = \frac{n\lambda}{2\sin\theta}. \tag{11}$$

Hence, the out-of-plane lattice constant of the investigated material can be calculated by:

$$c = \sqrt{h^2 + k^2 + l^2}\, d_{hkl}. \tag{12}$$

The total intensity $I_{hkl}$ of each peak, which is counted by the detector, is related to the crystallographic structure factor $F_{hkl}$,

$$I_{hkl} \propto |F_{hkl}|^2. \tag{13}$$

The structure factor can be expressed by

$$F_{hkl} = \sum_{j=1}^{m} f_j \exp(2\pi i(hu_j + kv_j + lw_j)), \tag{14}$$

---

[52] N. W. Ashcroft and N. D. Mermin. Brooks/Cole, Thomson Learning, 2005

with $f_j$ the atomic scattering factor of the $j^{th}$ atom of the unit cell and $u_j$, $v_j$, and $w_j$ the respective coordinates of the atom. $(hkl)$ are the Miller indices and $m$ the number of atoms in the unit cell. Only planes with either all even or all odd Miller indices lead to a non-vanishing reflected intensity. The determined peaks can be subdivided into fundamental and super lattice peaks. The fundamental peaks also appear in the presence of disorder. The super lattice peaks are sensitive to disorder. The $D0_{22}$ structure factors can be written as:

$$F^2_{004} = (f_A + f_B + f_C + f_D)^2 \tag{15}$$

$$F^2_{002} = (f_A - f_B - f_C + f_D)^2 \tag{16}$$

$$F^2_{011} = (-f_A - f_B - f_C + f_D)^2 \tag{17}$$

where $f_{A,B,C,D}$ is defined as the atomic scattering factor of the sublattices. In case of a perfectly ordered $D0_{22}$-$\mathrm{Mn_{3\text{-}x}Ga}$ crystal, $A, B, C$ correspond to Mn and $D$ to Ga. For a Mn-Co-Ga crystal the $A, B, C$ sublattices will be filled by Mn and Co. Furthermore, for the $\mathrm{Mn_{3\pm x}Ge}$ structure the distribution of the Mn and Ge atoms is analogous to $\mathrm{Mn_{3\text{-}x}Ga}$. The structure factor $F^2_{004}$ is characterized by the sum of all atomic scattering factors. For this reason, even in the presence of disorder, the resulting peak intensity will not vanish. The (004) peak is a fundamental reflex. In contrast to the (004) peak, the intensity of the (002) and (011) reflexes vanishes in the presence of disorder. Therefore these reflexes are super lattice peaks.

The $L1_0$ structure factors shows a different relation:

$$F^2_{002} = (f_A + f_B + f_C + f_D)^2 \tag{18}$$

$$F^2_{001} = (f_A + f_B - f_C - f_D)^2 \tag{19}$$

$$F^2_{011} = (f_A - f_B + f_C - f_D)^2 \tag{20}$$

For a perfect $L1_0$ crystal $A, B$ corresponds to Ga and $C, D$ to Mn. Here, the $F^2_{002}$ structure factor is the fundamental reflex and the $F^2_{001}$ peak the super lattice reflex. In a perfectly ordered crystal, the (011) intensity vanishes. Since in the $L1_0$ structure the (011) peak is forbidden its appearance is proof of the $D0_{22}$ structure.

The broadening $B$ of the peaks is caused by the instrument itself and by the sample. The instrument exhibits a Gaussian peak broadening, whereas the size of the crystallites and the strain within the crystallites result in a Lorentzian broadening. Therefore, the width can be written as

$$B^2 = B_i^2 + B_s^2, \tag{21}$$

with $B_i$ the instrumental and $B_s$ the sample induced width. The sample induced width can be expressed by

$$B_s = \frac{K_S \lambda}{\tau \cos\theta} + 4\varepsilon \tan\theta. \tag{22}$$

The first factor on the right side corresponds to the grain size $\tau$ and the second term to the strain $\varepsilon$, $K_S$ is the Scherrer factor or shape factor and $\lambda$ the wavelength. This relation is called Williamson-Hall[53] analysis. Thus the grain size $\tau$ can be estimated by applying the Scherrer equation

$$\tau = \frac{K_S \lambda}{B_s \cos\theta}, \tag{23}$$

with $K_S$ the shape factor, $\lambda$ the x-ray wavelength, and $B_s$ the full width at half maximum (FWHM) of the observed peak. The shape factor $K_S$ is close to unity and depends on the shape of the crystallite. An approximation can be made when using the FWHM, then $K_S$ is 0.89.[54] In addition, the strain $\varepsilon$ can be estimated with the following equation

$$\varepsilon = \frac{B_s}{4\tan\theta}. \tag{24}$$

The XRD scans of several $Mn_{3-x}Ga$ layers on MgO and $SrTiO_3$ are shown in Figure 20. Because of the varying $Mn_{3-x}Ga$ stoichiometries on MgO and $SrTiO_3$ substrates, we arranged the XRD scans by the same deposition conditions, i.e., deposition temperature and applied power. Samples on $SrTiO_3$ substrates

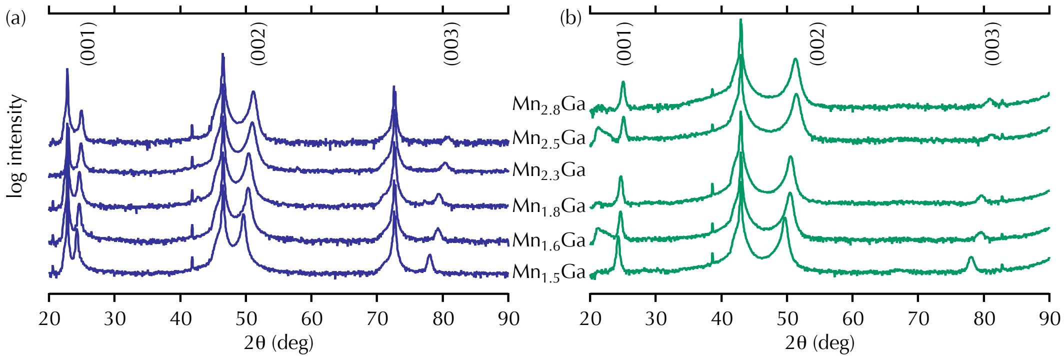

Figure 20: XRD scans of different $Mn_{3-x}Ga$ thin films deposited on (a) $SrTiO_3$ (blue) and (b) MgO (green) substrates. The deposition temperature was chosen between 520 °C and 595 °C. The reflex nomenclature corresponds to the $L1_0$ phase. For the $D0_{22}$ structure the following nomenclature is used: $2(hkl)_{L1_0}$.

[53] G. K. Williamson and W. H. Hall. In: *Acta metallurgica* (1953)

[54] L. Spieß et al. Vol. 2. Vieweg+ Teubner, Wiesbaden, 2005

exhibit six reflexes, three due to the substrate and three from the Mn-Ga thin film. Four reflexes are visible for samples on MgO substrates, one from the substrate itself and three from the Mn-Ga layer. First we will consider the samples with a Mn concentration below 65 at %, according to the layer composition on the $SrTiO_3$ substrates. All thin films, independently of the substrate, reveal the fundamental (002) reflex and the super lattice reflexes (001) and (003). Thus, the tetragonally distorted $L1_0$ structure was proved. For Mn rich samples, the XRD scans show the fundamental (004) reflex and the super lattice (002) and (006) reflexes. Therefore, the $D0_{22}$ structure was also achieved. With increasing Mn content the peak positions are shifted to higher $\theta$ angles. Thus the $c$ lattice constant increases with decreasing Mn content. This increase of $c$ is based on the irregular removal of the Mn atoms from the Wyckoff positions $2b$ and $4d$.[55] The thin film reflexes for samples on MgO are shifted to higher angles, pointing to a lower $c$ lattice constant compared to samples on $SrTiO_3$. The lower $c$ parameter for samples on MgO is based on the lateral expansion, due to the higher lattice mismatch between thin film and substrate. Only reflexes of the $L1_0$ and $D0_{22}$ phase were found, thus a highly oriented single phase was grown. The distinction between the two crystallographic phases is based on the Mn concentration. Additionally, Eulerian cradle measurements could be carried out to investigate the appearance of the (011) reflex.

| reflex | theta (deg) |
|---|---|
| (001) | 22.78 |
| (002) | 46.48 |
| (003) | 72.58 |

Table 6: $SrTiO_3$ substrate reflexes for Cu $K_\alpha$ $\lambda = 1.5419$ Å.

In Figure 21 an enlarged section of the (001) reflex of a $Mn_{1.5}Ga$ thin film on $SrTiO_3$ is illustrated. The appearance of Laue oscillations is clear evidence of a high crystalline order. They are

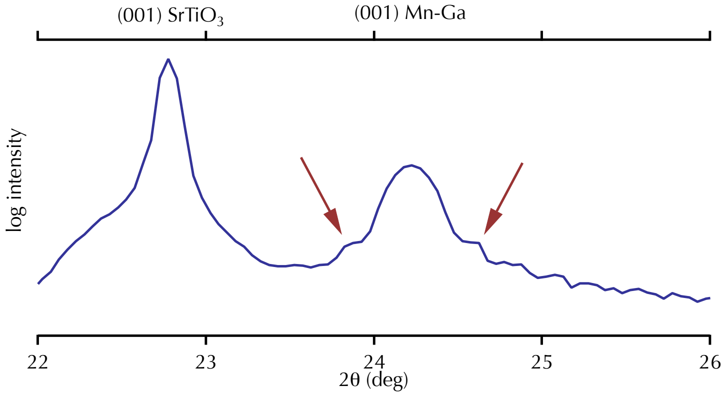

Figure 21: Enlarged section of the (001) reflex of a $Mn_{1.5}Ga$ thin film on a $SrTiO_3$ substrate (cf. Figure 20 (a)). Visible Laue oscillations are marked by red arrows.

[55] J. Winterlik et al. In: *Physical Review B* 77.5 (2008)

based on the interference of the diffracted x-ray from parallel crystal planes. However, only the samples that were deposited from the $Mn_{45}Ga_{55}$ or the $Mn_{50}Ga_{50}$ target show Laue oscillations if prepared on a $SrTiO_3$ substrate. Samples prepared by a co-sputtering process and/or on an MgO substrates revealed an absence of Laue oscillations.

AFTER INVESTIGATING THE GENERAL CRYSTALLOGRAPHIC PROPERTIES we analyzed the peak characteristics of the obtained XRD scans. The lattice constant $c$, the full width at half maximum (FWHM) and the textured order depending on the stoichiometry will be discussed. The latter is defined by

$$\text{textured order} = \frac{\text{net area}}{\text{layer thickness}}. \tag{25}$$

Since the peak intensity is proportional to the thin film thickness, the obtained net area is normalized to the respective film thickness.

In Figure 22 the dependence of the out-of-plane lattice parameter on the Mn-Ga composition is depicted. The lattice constant was determined by averaging the obtained $c$ parameter from the (001) and (002) reflex, or in case of a $D0_{22}$ crystal the (002) and (004). The $c$ parameter decreases with increasing Mn content for both crystal phases. This behavior is based on the irregular removal of Mn atoms from the $2b$ and $4d$ Wyckoff positions. Thin

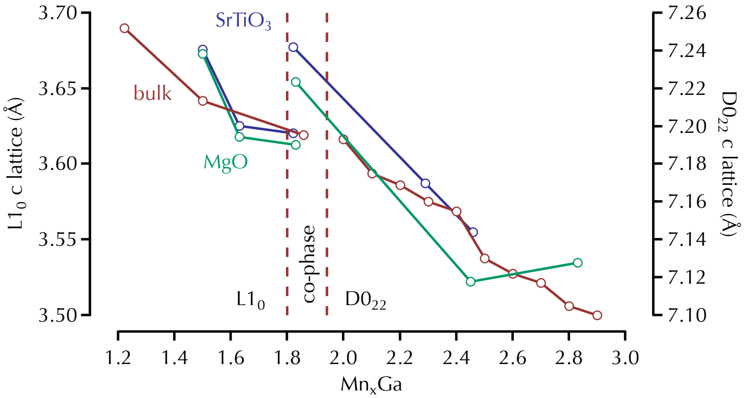

Figure 22: Dependence of the $c$ lattice parameter on the thin film composition on $SrTiO_3$ (blue) and MgO (green) substrates. The deposition temperature was 520 °C. The dashed red lines indicate the borders of the $L1_0$ and $D0_{22}$ phases. The red curves illustrate the reported bulk lattice constants from Winterlik et al. for the $D0_{22}$ and from Bither et al. for the $L1_0$ phase.[56]

films prepared on MgO substrates exhibit a lower *c* lattice constant, except for two samples, due to the *a*, *b* lattice mismatch of 7.13 %. For comparison we added the reported *c* parameters for $L1_0$ and $D0_{22}$ bulk samples.[57] The values obtained for samples on $SrTiO_3$ accord well with the literature data. However, samples on MgO substrates show a deviation from the reported values. Between $Mn_{1.8}Ga$ and $Mn_{1.94}Ga$ a co-phase of the $L1_0$ and $D0_{22}$ structures was reported by Niida et al.[58] Therefore the real crystallographic structure of the $Mn_{1.8}Ga$ thin film is not known, but the *c* parameter matches the reported value for the $L1_0$ phase.[59]

In the following we will investigate the FWHM of the super lattice and fundamental peaks. By neglecting the strain $\varepsilon$ we get a qualitative look at the grain size $\tau$. In Figure 24 (a) the FWHM of the super lattice (001) and (002) reflexes of the $L1_0$ and $D0_{22}$ crystal structure is illustrated. In addition, Figure 24 (b) depicts the FWHM of the fundamental $L1_0$ and $D0_{22}$ reflexes, i.e., the (002) and (004) peaks.[60] Thin films on MgO show no distinct behavior, neither for the super lattice nor for the fundamental reflex. Samples on $SrTiO_3$ substrates exhibit an almost constant FWHM of the super lattice reflex. Furthermore, the FWHM of the fundamental reflex shows a small increase with increasing Mn content, but decreases again for $Mn_{2.5}Ga$. Zhu et al.[61] reported the preparation of $Mn_xGa$ thin films ($x = 0.76$ to 2.6) with perpendicular magnetic anisotropy on (001) GaAs substrates. The obtained FWHM of the fundamental reflex are higher than 0.6 deg. Therefore, we obtained a higher crystallinity for $Mn_{3\text{-}x}Ga$ thin films on $SrTiO_3$ and MgO.

To estimate the grain size $\tau$ from the FWHM, the shape factor

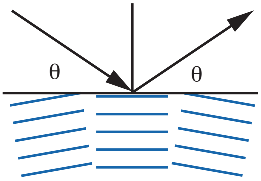

Figure 23: Schematic principle of mosaicism in a crystal.

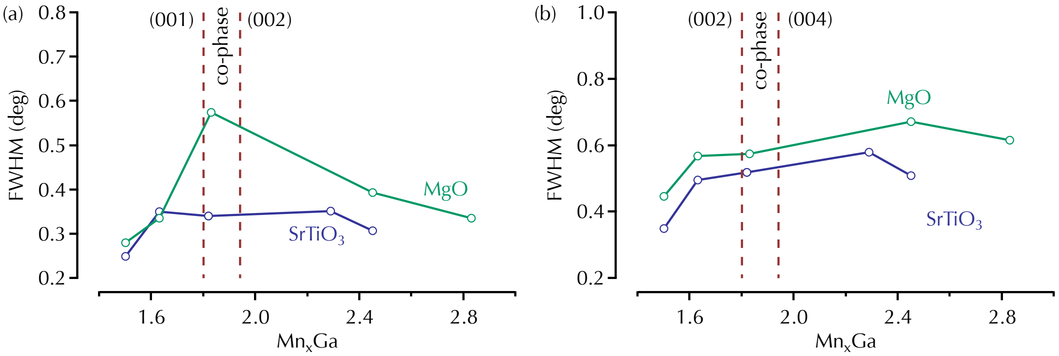

Figure 24: (a) FWHM of the (001) super lattice $L1_0$ reflex and the (002) super lattice $D0_{22}$ reflex. (b) FWHM of the (002) fundamental $L1_0$-reflex and the (004) fundamental $D0_{22}$-reflex. The $Mn_{3\text{-}x}Ga$ thin films were deposited on $SrTiO_3$ (blue) and MgO (green) substrates.

[56] J. Winterlik et al. In: *Physical Review B* 77.5 (2008); T. A. Bither and W. H. Cloud. In: *Journal of Applied Physics* 36.4 (1965)

[57] T. A. Bither and W. H. Cloud. In: *Journal of Applied Physics* 36.4 (1965); J. Winterlik et al. In: *Physical Review B* 77.5 (2008)

[58] H. Niida et al. In: *Journal of Applied Physics* 79.8 (1996)

[59] T. A. Bither and W. H. Cloud. In: *Journal of Applied Physics* 36.4 (1965)

[60] Caution, do not mix up the $L1_0$ and $D0_{22}$ (002) reflexes!

[61] L. J. Zhu et al. In: *Applied Physics Letters* 102.13 (2013)

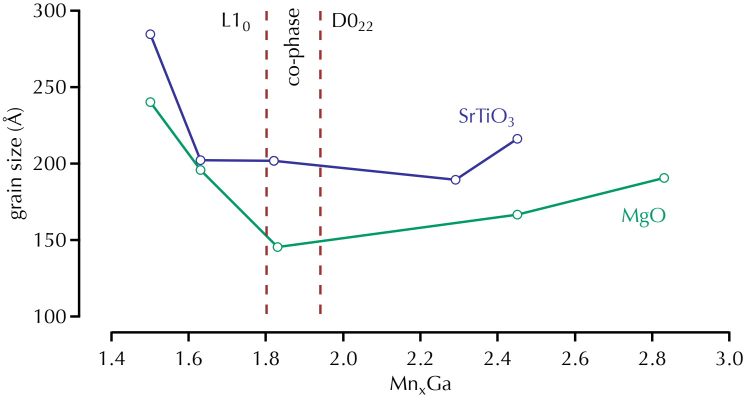

Figure 25: Estimated grain size for $Mn_{3-x}Ga$ thin films on $SrTiO_3$ (blue) and MgO (green) substrates as a function of the thin film stoichiometry.

$K_S$ is required. The factor $K_S$ tells us if mosaicism (cf. Figure 23) or globular crystal shapes are present. By using the FWHM a shape factor of 0.89 could be assumed.[62] The average grain size, estimated from the (001) and (002) reflex for $L1_0$ and the (002) and (004) for the $D0_{22}$ phase, is shown in Figure 25. Because the grain size depends on the reciprocal of the FWHM, the largest grains are obtained for samples with the smallest FWHM. For this reason, thin films on $SrTiO_3$ substrate exhibit largest grains between 190 Å and 290 Å. Thin films on MgO reveal marginal lower grain sizes for samples prepared from a composite target. However, one has to keep in mind that broadening from the strain and other factors were neglected. Therefore, the real grain size could differ from the obtained values.

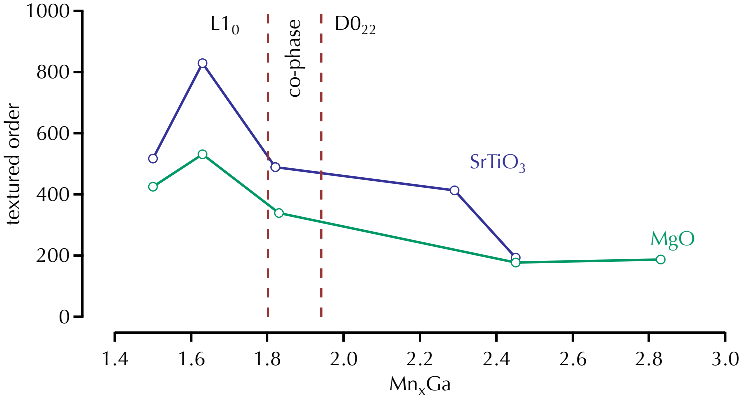

Figure 26: Textured order of $Mn_{3-x}Ga$ thin films on $SrTiO_3$ (blue) and MgO (green) as a function of the thin film stoichiometry.

---

[62] L. Spieß et al. Vol. 2. Vieweg+ Teubner, Wiesbaden, 2005

The last characteristic obtained from the XRD scan is the textured order, as defined in Equation (25). Figure 26 depicts the obtained textured order values as a function of the stoichiometry. The highest values are achieved for thin films on $SrTiO_3$ with a maximum of 830 for $Mn_{1.6}Ga$. In addition, the $Mn_{1.6}Ga$ sample reveals a $c$ lattice constant that is only marginally different from that of a bulk sample with equal composition. Furthermore, Laue oscillations are clearly visible (cf. subsection *The Co-Fe-B interlayer*) and thus this sample appears to be a perfectly crystalline thin film.

To sum up, $Mn_{3\text{-}x}Ga$ thin films on $SrTiO_3$ show a higher crystalline quality than thin films deposited on MgO. Of course, this relation was expected due to the low lattice mismatch of 0.12 % between the Mn-Ga crystal and the $SrTiO_3$ substrate. The effects on the crystal structure of the Mn-Ga induced by the lattice mismatch of 7.13 % between thin films and MgO were clearly seen in the $c$ lattice constant, the FWHM, and the textured order. In addition, samples prepared from the $Mn_{45}Ga_{55}$ and $Mn_{50}Ga_{50}$ composite targets reveal the lowest FWHM, largest grain sizes and highest textured orders. In combination with the obtained roughness values, these thin films are most promising for integration into MTJ's.

### *Magnetic properties of Mn-Ga*

The magnetic properties of selected samples were investigated by means of a superconducting quantum interference device (SQUID)[63] with an external magnetic field of up to ±7 T.

The SQUID is based on the quantization of the magnetic flux and the Josephson effect.[64] In a superconducting loop, the magnetic flux must be an integer number of the magnetic flux quanta $\phi_0$. The Josephson effect describes the tunneling of Cooper pairs in a superconductor/insulator/superconductor trilayer system. Here again, a voltage is generated across the junctions that is proportional to the magnetic flux. A magnetic flux variation of $10^{-6}\ \phi_0$ can be determined. That corresponds to a field change of $10^{-15}$ T for a sample with an area of $1\,\mathrm{mm}^2$.

In Figure 27 the in-plane and out-of-plane SQUID measurements of a $Mn_{1.5}Ga$ and a $Mn_{2.8}Ga$ thin film on MgO are illustrated. For both samples the deposition temperature was 550 °C. The dia-/paramagnetic background is subtracted by a line. The $L1_0$-ordered sample shows a magnetization of $514(1)\,\mathrm{kA\,m^{-1}}$. Köhler et al. reported a magnetization of $600\,\mathrm{kA\,m^{-1}}$ for a 20 nm

[63] R. C. Jaklevic et al. In: *Physical Review Letters* 12.7 (1964)

[64] B. D. Josephson. In: *Physics Letters* 1.7 (1962)

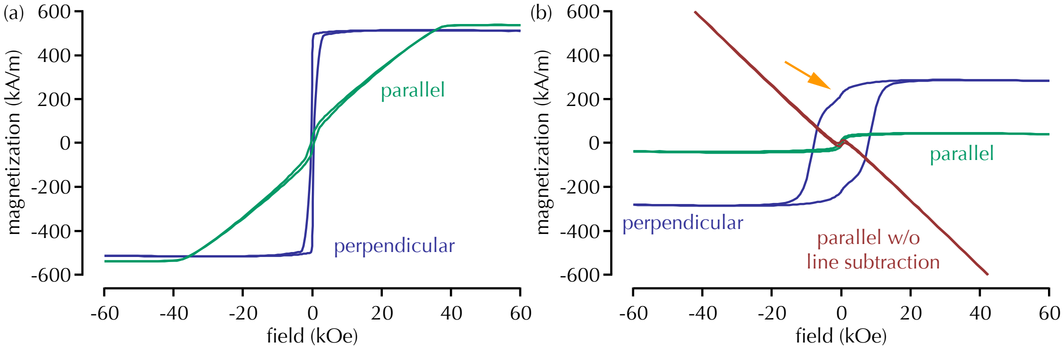

Figure 27: SQUID magnetization loops of a (a) $L1_0$- and a (b) $D0_{22}$-ordered $Mn_{3\text{-}x}Ga$ thin film on MgO. The external magnetic field was applied parallel (green) and perpendicular (blue) to the sample surface. To eliminate the dia-/paramagnetic background a line subtraction was performed (cf. blue and green curves). The red curve shows the magnetization loop for the $D0_{22}$ sample with parallel field direction without line subtraction. The $D0_{22}$ structure reveals a step like hysteresis loop (indicated by the orange arrow).

thick $L1_0$-ordered $Mn_{1.86}Ga$ thin film on MgO with a Cr buffer.[65] The lower magnetization of our sample is induced by a higher crystalline order and thus a higher compensation of the magnetic moments. The external magnetic field is high enough to saturate both samples in the out-of-plane direction. At a field of approximately 4 T the in-plane hysteresis of the $Mn_{1.5}Ga$ thin film saturates. An estimation of the anisotropy energy $K$ can be made by using the following Equation from the Stoner-Wohlfarth[66] model

$$K = \frac{\vec{H}_K \vec{M}_S}{2} \tag{26}$$

with $\vec{H}_K$ being the anisotropy field and $\vec{M}_S$ the saturation magnetization. The determined value is $K = 0.97(2) \times 10^6\,\mathrm{J\,m^{-3}}$ and thus in the same order as the value reported by Köhler et al.[67] ($1.2 \times 10^6\,\mathrm{J\,m^{-3}}$) for the $Mn_{1.86}Ga$ compound on Cr buffered MgO. The higher Mn amount compared to our sample causes the higher anisotropy energy.

The magnetization of the $D0_{22}$ phase is lower ($283(1)\,\mathrm{kA\,m^{-1}}$) compared to the $L1_0$-ordered sample, due to the higher compensation of magnetic moments. Kurt et al.[68] reported a magnetization of $140\,\mathrm{kA\,m^{-1}}$ for a $Mn_3Ga$ thin film on MgO. The lower magnetization is based on the higher Mn concentration and thus on the higher compensation of magnetic moments. However, the $D0_{22}$ sample could not be saturated in the in-plane direction with a field up to 7 T (cf. Figure 27 (b) red curve). Hence, an anisotropy constant could not be estimated. In the Stoner-Wohlfarth model, the coercive field $\vec{H}_c$ and the anisotropy field $\vec{H}_K$ are equal. How-

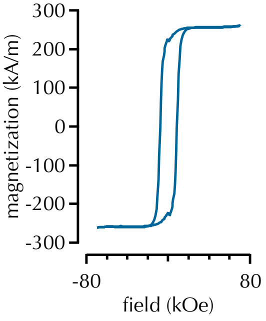

Figure 28: Out-of-plane measurement with subtracted in-plane loop of the $D0_{22}$-$Mn_{2.8}Ga$ sample.

---

[65] A. Köhler et al. In: *Applied Physics Letters* 103.16 (2013)

[66] E. C. Stoner and E. P. Wohlfarth. In: *Philosophical Transactions of the Royal Society of London. Series A. Mathematical and Physical Sciences* (1948)

[67] A. Köhler et al. In: *Applied Physics Letters* 103.16 (2013)

[68] H. Kurt et al. In: *Physical Review B* 83.2 (2011)

ever, Figure 27 (a) shows that this approximation is not possible here. In general, the formation of domain walls is a reason for that.

Another interesting feature is seen in the hysteresis loop, a step-like switching around zero field. Other groups obtained similar results, but none provided an explanation.[69] Jesche et al.[70] reported a step like hysteresis for $Li_2(L_{1\text{-}x}Fe_x)N$ and took its presence as an indicator of the partial turnover of magnetic moments at zero field. In our case, it is plausible that a second, soft-magnetic phase induces this step. By subtracting the in-plane hysteresis from the out-of-plane hysteresis, the step nearly vanishes and thus supports the assumption of a soft-magnetic phase (cf. Figure 28). Besides the magnetization, the coercive field also shows dependence on the stoichiometry. For Mn rich thin films the coercivity is 8.30(5) kOe and for Mn poor thin films 400(10) Oe. The rectangularity of a slope is measured by its squareness value, which is defined by $S = \vec{M}_r/\vec{M}_S$. Here $\vec{M}_r$ denotes the remanence magnetization. The $D0_{22}$-$Mn_{2.8}Ga$ thin film exhibits an $S$ of 0.78 and the $L1_0$-ordered thin film reaches a value of 0.80.

Figure 29 shows the hysteresis loop of a $Mn_{2.5}Ga$ thin film deposited at 595 °C on a $SrTiO_3$ substrate. The sample exhibits a magnetization of 295(1) kA m$^{-1}$. The magnetization is higher compared to that of the $Mn_{2.8}Ga$ thin film on MgO due to the lower Mn content and thus the lower compensation of the magnetic moments. Furthermore, the magnetization is higher compared to that reported by Wu et al.[71] for $Mn_{2.5}Ga$ on Cr buffered MgO substrate. They reported a value of 250 kA m$^{-1}$ for an annealing temperature of 400 °C. Most likely, the second, soft-

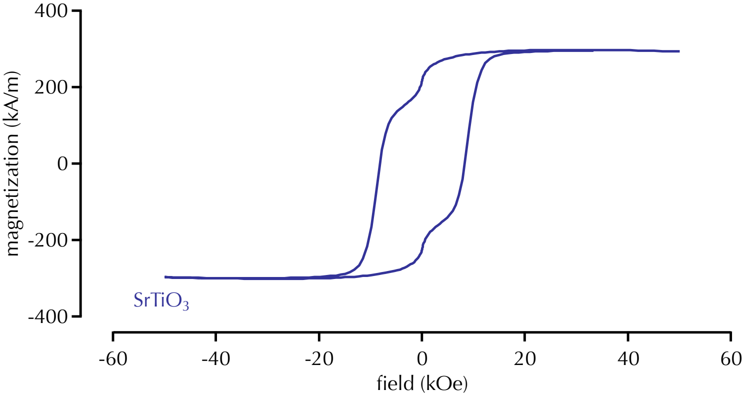

Figure 29: Hysteresis loop of a $Mn_{2.5}Ga$ thin film on $SrTiO_3$. The deposition temperature was 595 °C and the film thickness is 33.47 nm.

[69] W. Feng et al. In: *Journal of Applied Physics* 108.11 (2010); K. M. Krishnan. In: *Applied Physics Letters* 61.19 (1992); Z. Li-Jun et al. In: *Chinese Physics B* 22.11 (2013); L. Zhu and J. Zhao. In: *Applied Physics A* (2013)

[70] A. Jesche et al. In: *Nature Communications* 5 (2014)

[71] F. Wu et al. In: *Applied Physics Letters* 94.12 (2009)

magnetic phase is the reason for the higher magnetization of the $Mn_{2.5}Ga$ thin film on $SrTiO_3$. However, the coercivity is around 8.40(5) kOe and thus almost equal to the coercivity of the $Mn_{2.8}Ga$ sample on MgO. Furthermore, we obtained a $S$ of 0.74 for the $Mn_{2.5}Ga$ layer. This value is lower compared to the other samples and probably based on the second, soft-magnetic phase.

## *Soft x-ray absorption spectroscopy*

The Faraday and Kerr effects were the first phenomena that revealed interaction between polarized light and a magnetic medium. However, the applicability of polarized light is limited due to its wavelength. In 1985 Thole et al.[72] predicted the occurrence of linear x-ray magnetic dichroism (XMLD) and in 1987 Schütz et al.[73] reported an x-ray magnetic circular dichroism (XMCD) effect. The magnetic properties of transition metals and rare earths are based on the $3d$ and $4f$ valence electrons. The important absorption edges, the $L$-edge for transition metals and the $M$-edge for rare earths, are between 500 eV and 1500 eV. Therefore, soft x-ray light (0.1 keV to 5 keV) is sufficient for the investigation of magnetic properties and a viable alternative to neutrons.

X-ray absorption spectroscopy (XAS) is element specific and provides insight in the chemical properties, since core level binding energies depend on chemical state and atomic number. When a sample is irradiated an electron from the core level can be excited onto a higher unoccupied level above the Fermi energy (cf. Figure 31). In case of polarized x-rays (linear or circular) the magnetic properties can be analyzed. To compare the bulk and surface properties two different measuring modes were available. The bulk-sensitive luminescence mode (LM) is based on the excitation in the substrate. Secondary electrons from the thin film excite electrons in the substrate. The resulting luminescence yield is detected by a photodiode, with a spectral response from $\lambda = 190\,\mathrm{nm}$ to 1000 nm, behind the sample. Unfortunately, the luminescence mode is not applicable for all types of substrate, MgO works while $SrTiO_3$ not. Aguilar et al.[74] reported a single-emission band at 500 nm of $SrTiO_3$ at temperatures below 100 K. This result could not be reproduced, even at temperatures around 20 K an insufficient luminescence signal was observed. An advantage of the luminescence mode is its applicability on insulating samples. However, artifacts from the substrate will be seen in the obtained spectrum, like a second order Mg peak at 651.5 eV.

[72] B. T. Thole et al. In: *Physical Review B* 31.10 (1985)

[73] G. Schütz et al. In: *Physical Review Letters* 58.7 (1987)

[74] M. Aguilar and F. Agulló-López. In: *Journal of Applied Physics* 53.12 (1982)

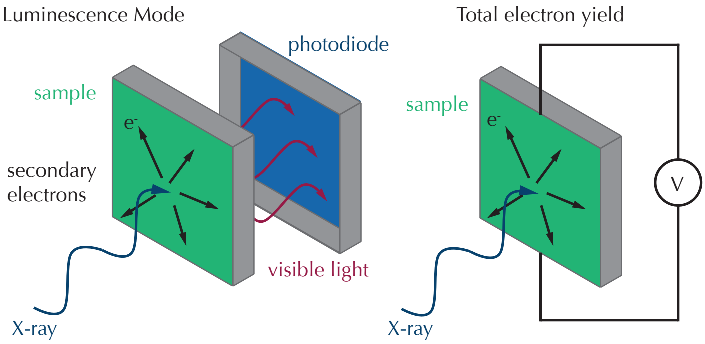

Figure 30: Schematic sketch of the two measuring methods (a) luminescence mode and (b) total electron yield.

The surface-sensitive total electron yield (TEY) provides information about the first 2 nm to 3 nm of the thin film. Here, a constant current is driven through the sample. By exciting local electrons from the core level, the free electrons occupy the positions available and the current increases. In this way, only conducting samples can be measured. Primarily, samples on $SrTiO_3$ substrate were measured in TEY mode. Thin films on MgO were analyzed in TEY and LM mode.

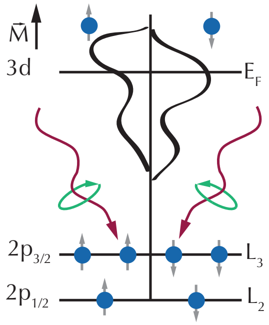

Figure 31: X-ray absorption from the $L_{2,3}$-edges into the $3d$ for left and right circularly polarized x-rays. $\vec{M}$ denotes the magnetic state of the sample.

Figure 31 illustrates the TEY for left and right circularly polarized light. The left circularly polarized x-rays lead to spin-up polarization of the photoelectrons at the $L_3$-edge via spin-orbit coupling ($j = l + s$).[75] Vice versa right circularly polarized light leads to spin-down polarization.[76] Due to the magnetization direction of the sample, more unoccupied spin-up $d$ states are available. Therefore, the absorption for left circularly polarized light is higher compared to right circularly polarized light because of the difference in the spin-up and spin-down $d$ valence band (cf. Figure 32). However, the absorption spectrum shows the opposite behavior at the $L_2$-edge due to reverse spin-orbit coupling ($j = l - s$). If the measuring method is the bulk-sensitive luminescence mode a slightly different attempt has to be made. The linear XA coefficients $\mu^{\pm}$ were obtained from the transmission spectra $I^{\pm}$, for parallel and antiparallel orientations of magnetic field and x-ray beam direction, and $I_0$. The intensities $I^{\pm}$ are defined by

$$I^{\pm} = I_0 \exp(-\mu^{\pm} d) \tag{27}$$

with $d$ the thin film thickness and $I_0$ the zero signal of the beam before penetrating the sample.[77] Thus, the linear coefficients are

---

[75] Here, $j$, $l$, and $s$ are the three quantum numbers.

[76] Instead of changing the polarization of the incoming beam, the magnetization state of the sample can be varied.

[77] Perturbations in the beam can be canceled by normalizing on $I_0$

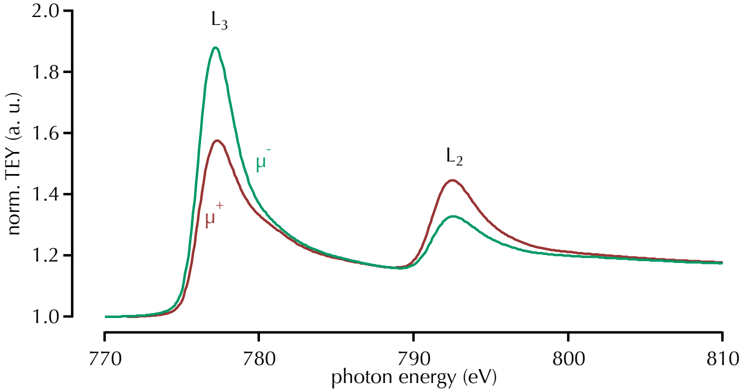

Figure 32: TEY of Co for left and right circularly polarized light, i.e., for parallel and antiparallel orientations of x-ray beam direction and magnetic field.

given by

$$\mu^{\pm} \propto -\ln\left(\frac{I^{\pm}}{I_0}\right) \tag{28}$$

Therefore, the XA and the XMCD spectra are given by

$$\mathrm{XAS} = \frac{\mu^{+} + \mu^{-}}{2}, \tag{29}$$

$$\mathrm{XMCD} = \mu^{+} - \mu^{-}. \tag{30}$$

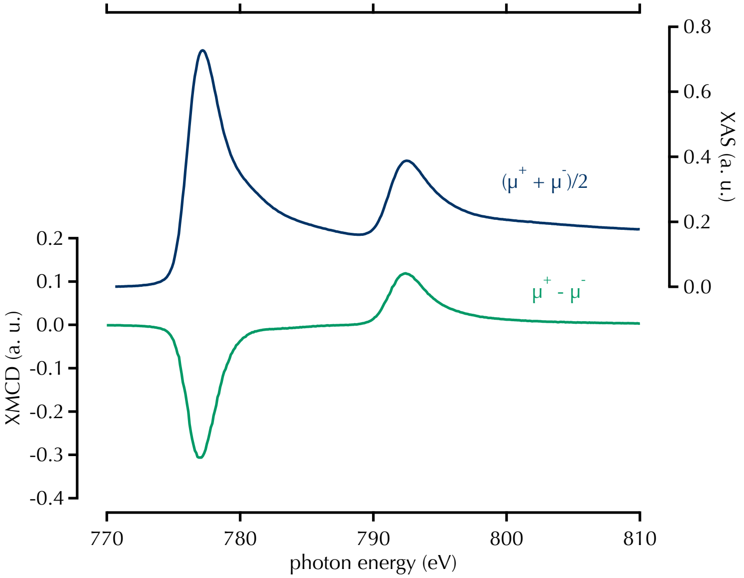

Figure 33: Exemplary Co-XA and XMCD spectrum.

The XA and XMCD spectra of the Co sample from Figure 32 are illustrated in Figure 33. In general, one can obtain the magnetic moment from XAS and XMCD data by using the approach of Chen et al.[78]

$$m_{orb} = -\frac{N_h}{p_{h\nu}\cos\theta}\frac{4q}{3r} \tag{31}$$

$$m_{spin} = -\frac{N_h}{p_{h\nu}\cos\theta}\frac{(6p-4q)}{r} \tag{32}$$

with $N_h$ the number unoccupied $3d$ states, i.e., holes, $p_{h\nu}$ the circular polarization degree and $\theta$ the angle between the magnetization direction of the sample and the x-ray beam direction. The integrals $p$, $q$, and $r$ are defined as

$$p = \int_{L_3} (\mu^+ - \mu^-)dE \tag{33}$$

$$q = \int_{L_3+L_2} (\mu^+ - \mu^-)dE \tag{34}$$

$$r = \int_{L_3+L_2} (\mu^+ + \mu^- - 2S_b)dE \tag{35}$$

where $S_b$ is the background that is often assumed as a no-free-parameter two-step-like function. The peak positions of the $L_3$ and $L_2$ white lines are the thresholds of the two-step like function. The height of the $L_3$ and $L_2$ was set to 2/3 and 1/3 of the average absorption coefficients in the post-edge region.[79]

This approach can be expanded by the attempt of Scherz[80], where assumptions about the number of $3d$ holes are not necessary. Here, the $r$-values that were taken from the XAS are defined as:

$$r = CN_h\eta, \tag{36}$$

$\eta$ is the post-edge jump height. $C$ is a constant depending on the transition matrix elements and connects the core and valence states involved in the $2p$- to $3d$-transitions, the values reported by Scherz[81] and Schmalhorst et al.[82] are illustrated in Table 7. Taking this relation into account, the orbital magnetic moment $m_{orb}$ and the spin magnetic moment $m_{spin}$ are given by:

$$m_{orb} = -\frac{1}{p_{h\nu}\cos\theta}\frac{4q}{6C\eta} \tag{37}$$

$$m_{spin} = -\frac{1}{p_{h\nu}\cos\theta}\frac{(6p-4q)}{6C\eta}. \tag{38}$$

By normalizing the post-edge jump height $\eta$, the remaining values are the constant $C$, the $p$- and $q$-values, the beam polarization

| Element | $C$ |
|---|---|
| Co | 7.8 eV |
| Fe | 6.6 eV |
| Mn | 6.0 eV |

Table 7: $C$ values for different transition metals.

[78] C. T. Chen et al. In: *Physical Review Letters* 75.1 (1995)

[79] C. T. Chen et al. In: *Physical Review Letters* 75.1 (1995); J. Schmalhorst et al. In: *Journal of Applied Physics* 105.5 (2009)

[80] A. Scherz. Ph.D. Thesis. Freie Universität Berlin, 2003

[81] A. Scherz. Ph.D. Thesis. Freie Universität Berlin, 2003

[82] J. Schmalhorst et al. In: *Journal of Applied Physics* 105.5 (2009)

$p_{h\nu}$ = 60(5) % and the angle between magnetization and x-ray beam direction $\theta = 0$ deg.[83] To calculate $m_{spin}$ for Mn the *jj* mixing cannot be neglected.[84] For this reason $m_{spin}^{\mathrm{Mn}}$ has been multiplied by the compensation factor $\chi = 1.5$.

The Mn-XA spectra of different $Mn_{3\text{-}x}Ga$ compositions on $SrTiO_3$ substrates, measured at Beamline 6.3.1, LBNL, Berkeley, are illustrated in Figure 34. The results were obtained in surface-sensitive TEY mode. The energies reported for the Mn-$L_3$- and Mn-$L_2$-edge are 638.7 eV and 649.9 eV. Our samples reveal a small discrepancy with respect to the literature data, due to the calibration of the beamline and the possible oxidation of the Mn. By taking a closer look at the XA spectra of the $Mn_{2.3}Ga$ thin film, we find an additional feature at photon energies above the $L_3$-edge. This feature is a clear indicator of the formation of Mn–O. Additionally, the $Mn_{1.9}Ga$ sample exhibits the same multiplet structure, but less distinct than for $Mn_{2.3}Ga$. It is difficult for both spectra to distinguish between MnO, $MnO_2$, and $Mn_2O_3$.[85] For $Mn_{1.5}Ga$ the feature is less distinct and for $Mn_{1.6}Ga$ it is not visible. Hence, the formation of Mn–O is higher for co-deposited

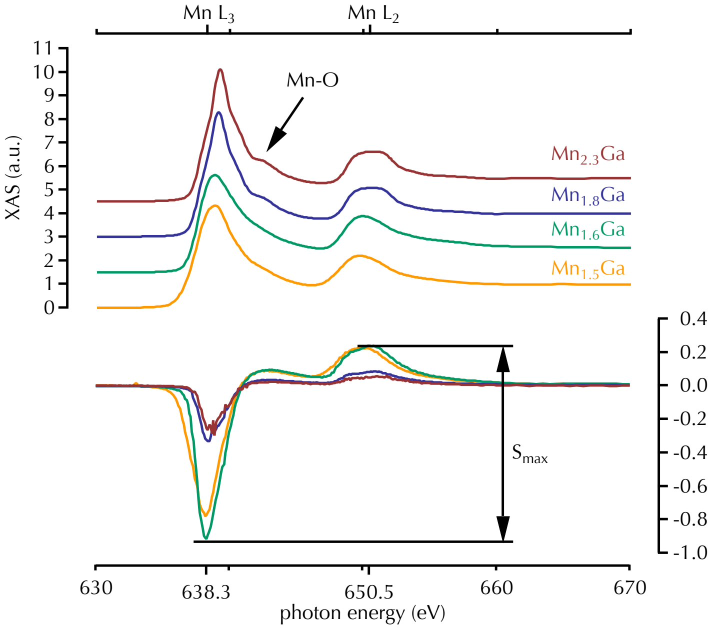

Figure 34: X-ray absorption and XMCD spectra for different $Mn_{3\text{-}x}Ga$ compositions on $SrTiO_3$ substrates. The deposition temperature was 520 °C. The measurement temperature was set to 300 K and the angle between x-ray direction and sample magnetization was 0 deg.

---

[83] Values for Beamline (BL) 6.3.1, LBNL, Berkeley, CA

[84] H. A. Dürr et al. In: *Physical Review B* 56.13 (1997); Y. Yonamoto et al. In: *Physical Review B* 63.21 (2001)

[85] S. Voss et al. In: *Physical Review B* 75.4 (2007)

samples. Most likely, the high surface roughness of co-deposited samples is the reason for the high degree of oxidation.[86] For clarification the XMCD spectra for the same compositions are shown in Figure 34. The XMCD amplitude $S_{max}$ is proportional to the magnetic moment that depends on the Mn oxidation state and the crystallographic structure. Mn poor thin films reveal a higher magnetic moment than Mn rich samples. For our samples, the $S_{max}$ value of $Mn_{1.6}Ga$ is higher compared to $Mn_{1.5}Ga$, which indicates a higher degree of oxidation of Mn for the latter. The Mn rich compositions show the lowest XMCD amplitudes, due to the higher compensation of the magnetic moment and the formation of Mn–O. By applying the sum rules on the XA and XMCD spectra in Figure 34, the magnetic moment can be determined.[87] Figure 35 presents the calculated magnetic moment as a function of the stoichiometry. The highest values were found for the $L1_0$ structure, with 1.96(3) $\mu_B$ and 1.98(3) $\mu_B$ for $Mn_{1.5}Ga$ and $Mn_{1.6}Ga$. Sakuma et al.[88] reported a value of 2.51 $\mu_B$ per Mn atom for $Mn_1Ga_1$ and Hasegawa and Tsuboya[89] estimated a magnetic moment of 1.7 $\mu_B$ per Mn atom for $Mn_{1.27}Ga$.[90] Thus, the values we obtained are in the same range as the reported ones. Winterlik et al.[91] reported a low magnetic moment of 0.43 $\mu_B$ for $Mn_{2.3}Ga$ bulk samples. The value obtained for our $Mn_{2.3}Ga$ thin film is comparable to those presented in the literature. However, oxidation and thus the decrease of the magnetic moment has to be kept in mind. Therefore, the magnetic thin film might have a higher magnetic moment compared to the bulk sample. The value of the $Mn_{1.8}Ga$ thin film is 0.68(5) $\mu_B$ per Mn atom, here again the oxidation of the Mn should not be neglected.[92] However,

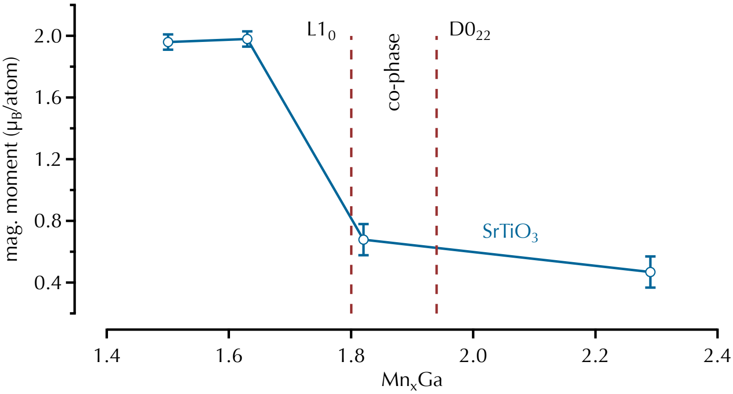

Figure 35: Magnetic moment obtained from XAS and XMCD measurements for different $Mn_{3-x}Ga$ stoichiometries on $SrTiO_3$ substrates.

[86] It should be mentioned that even a monolayer of Mn–O at the interface to the barrier results in a drastical decrease of the TMR effect due to the lower spin polarization.

[87] C. T. Chen et al. In: *Physical Review Letters* 75.1 (1995)

[88] A. Sakuma. In: *Journal of Magnetism and Magnetic Materials* 187.1 (1998)

[89] M. Hasegawa and I. Tsuboya. In: *Journal of the Physical Society of Japan* 20 (1965)

[90] M. Hasegawa and I. Tsuboya. In: *Journal of the Physical Society of Japan* 20 (1965)

[91] J. Winterlik et al. In: *Physical Review B* 77.5 (2008)

[92] The impact of the formation of Mn–O on the magnetic moment will be discussed in the next chapter.

the dependence of the magnetic moment on the stoichiometry shows a decrease with increasing Mn content. For this reason, the expected behavior was confirmed.

The formation of interfacial Mn–O is a fundamental problem. MnO is antiferromagnetic with a Néel temperature of $T_N = 118\,\mathrm{K}$. Above this temperature MnO acts like a paramagnet with low spin polarization. Hence, a low TMR effect is achieved. In the next section the insertion of ferromagnetic layers between the Mn-Ga and the barrier will be discussed.

## *The Co-Fe-B interlayer*

The previously mentioned formation of Mn–O at the barrier interface has to be suppressed. In fact, the last atomic layer between electrode and barrier is responsible for the TMR effect. More precisely, the spin polarization of the material next to the barrier. In case of Mn-Ga the theoretical spin polarization is around 88 %.[93] However, if the Mn oxidizes due to the deposition of MgO, an antiferromagnetic MnO layer below 118 K or a paramagnetic MnO layer above this temperature is next to the barrier. Thus, the TMR effect will be lowered. A common attempt to overcome the formation of Mn–O is the deposition of a 0.5 nm thick Mg layer between bottom electrode and barrier.[94] However, if the Mg does not fully oxidize a material with low spin polarization is placed between bottom electrode and barrier. Therefore, a considerable lower TMR effect will be achieved. Apart from the oxidation issue, the lattice mismatch between the Mn-Ga layer and the MgO barrier has to be minimized. The lateral distortion due to the barrier could lead to band structure effects that lower the spin polarization or change the unoccupied states in the minority spin channel. A simple attempt towards this venture is the deposition of a ferromagnetic layer like Co or Fe.[95] However, the spin polarization of Co and Fe is reasonably lower compared to Mn-Ga. Tedrow et al.[96] reported a spin polarization of 34 % for Co and 44 % for Fe. The respective spin polarization was determined by spin dependent tunneling of electrons from the ferromagnetic layer into a superconducting Al layer. Despite the spin polarization the magnetic orientation is not of minor importance. In general, the interface between ferromagnetic materials, e.g., Co and Fe, and heavy nonmagnetic transition metals, e.g., Pt, Pd, and Au have been used to obtain PMA.[97] Furthermore, Yang et al.[98] reported a first-principle investigation of PMA in-

[93] B. Balke et al. In: *Applied Physics Letters* 90.15 (2007)

[94] T. Kubota et al. In: *Journal of Applied Physics* 110.1 (2011)

[95] Q. L. Ma et al. In: *Journal of Applied Physics* 114.16 (2013)

[96] P. M. Tedrow and R. Meservey. In: *Physical Review B* 7.1 (1973)

[97] S. Monso et al. In: *Applied Physics Letters* 80.22 (2002); B. Rodmacq et al. In: *Journal of Applied Physics* 93.10 (2003)

[98] H. X. Yang et al. In: *Physical Review B* 84.5 (2011)

duced by the interface between a ferromagnet (Co and Fe) and an MgO barrier. However, in all cases the ferromagnet has to reveal a thickness below 1 nm. This behavior is perfect for the approach using a ferromagnetic layer. In fact, when depositing a ferromagnet on a ferrimagnet like $L1_0$-ordered Mn-Ga, the magnetic moments of the ferromagnet align parallel to the magnetic moments of the ferrimagnet.[99] Ma et al.[100] reported an upcoming in-plane magnetization direction for 2 nm thick Co interlayers. The highest reported TMR effect was 40 % at 300 K for a Co interlayer thickness of 1.5 nm.[101] The stack consists of MgO/Cr (40 nm)/$Mn_{1.6}Ga$ (30 nm)/Mg (0.4 nm)/MgO (1.8 nm)/Co-Fe-B (1.2 nm). The obtained TMR effect is not sufficient for application in MRAM devices, thus a new interlayer material has to be investigated.

A reasonable choice is Co-Fe-B, due to the encouraging publications about the PMA for thin films around 1 nm, the TMR effect (124 % at 300 K) and the low current densities for STT switching ($3.4 \times 10^{-6}$ A cm$^{-2}$ for $AR = 16\,\Omega\,\mu$m).[102] We prepared samples with a 23 nm thick $Mn_{1.6}Ga$ film on $SrTiO_3$ substrates at a deposition temperature of 520 °C. On top of the Mn-Ga a $Co_{40}Fe_{40}B_{20}$ thin film with a thickness between 0.4 nm and 2 nm was sputter deposited at room temperature. All samples were capped by 2.3 nm MgO. Here the deposition method for the MgO was magnetron sputtering or e-beam evaporation. XRR measurements were carried out to determine the film thickness, roughness and density.

## *X-ray reflectivity measurements*

In Figure 36 an exemplary XRR scan of a sample with an 0.8 nm thick Co-Fe-B layer is shown.[103] The appearance of the distinct oscillations is a qualitative sign of a smooth surface. By fitting the XRR scan via Parratt algorithm the film thickness, density and roughness were determined (cf. Table 8).[104] The bottom Mn-Ga layer shows a roughness of only 0.51(5) nm and a film thickness of around 22.98(5) nm. The Co-Fe-B layer is approximately 0.5 nm thicker, whereas the MgO layer is 0.5 nm thinner than the intended values. This could be evidence of an intermixing of both layers. For this reason, further investigations via transmission electron microscopy (TEM) or AES have to be carried out to prove the intermixing of the elements. The roughness value of the Co-Fe-B is 0.55(5) nm and that of the MgO is

[99] Q. L. Ma et al. In: *Applied Physics Letters* 101.3 (2012); Q. L. Ma et al. In: *Journal of Applied Physics* 114.16 (2013)

[100] Q. L. Ma et al. In: *Applied Physics Letters* 101.3 (2012)

[101] Q. L. Ma et al. In: *Applied Physics Letters* 101.3 (2012)

[102] S. Ikeda et al. In: *Nature Materials* 9.9 (2010); H. Meng et al. In: *Journal of Physics D: Applied Physics* 44.40 (2011)

[103] An exemplary XRR scan is shown because the thickness of the Co-Fe-B should not influence the thickness or roughness of the $Mn_{1.6}Ga$ thin film.

[104] L. Parratt. In: *Physical Review* 95.2 (1954)

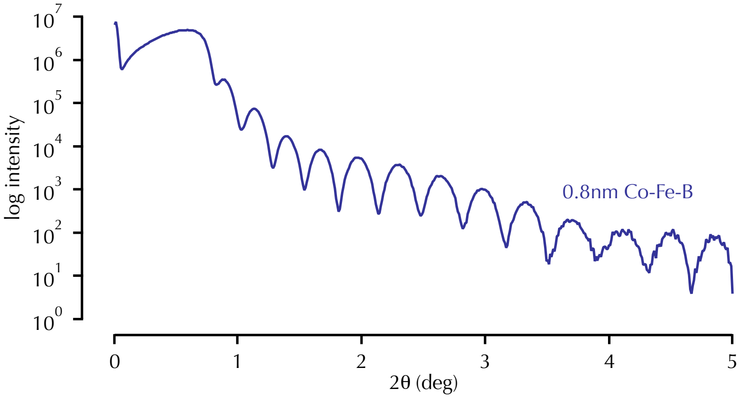

Figure 36: XRR scan of a $Mn_{1.6}Ga$ (23 nm)/Co-Fe-B (0.8 nm)/MgO (2.3 nm) stack on $SrTiO_3$ substrate. The deposition temperature was 520 °C.

| layer | $d$ (nm) | roughness (nm) | density ($g\,cm^{-3}$) |
|---|---|---|---|
| $Mn_{1.63(6)}Ga$ | 22.98(5) | 0.51(5) | 6.90(5) |
| Co-Fe-B | 1.32(5) | 0.55(5) | 4.64(5) |
| MgO | 1.76(5) | 0.78(5) | 4.08(5) |

Table 8: XRR data obtained by fitting the scan shown in Figure 36 via Parratt algorithm.

0.78(5) nm. Therefore, smooth surfaces were obtained, which is important for further integration into MTJ's.

### *Crystallographic properties*

XRD investigations were carried out to verify the crystallographic phase of the $Mn_{1.6}Ga$ thin films. Figure 37 illustrates the XRD data obtained from two exemplary samples, one without a Co-Fe-B interlayer and one with a 2 nm Co-Fe-B interlayer. The Mn-Ga peak positions (cf. Table 9) of the super lattice (001) and (003) reflex and the fundamental (002) peak are nearly at the same angles for all Co-Fe-B capping layer. The $c$ lattice constant was calculated by Braggs law (cf. Equation (10)).The average lattice constant is $c \approx 3.63$ Å (cf. Figure 38) and corresponds well with the value reported by Niida et al.[105] of 3.6249 Å for $Mn_{1.7}Ga$. The discrepancy is based on the different stoichiometry. Apart from the lattice constant we examined the full width at half maximum (FWHM) of the rocking curve ($\theta/2\theta$ scan with constant $\omega$ angle) carried out on the fundamental reflex. Figure 39 shows the FWHM depending on the Co-Fe-B interlayer thickness. An average value of 0.24 deg is found showing a narrow distribution of

| peak | angle |
|---|---|
| (001) | 24.58 deg |
| (002) | 50.33 deg |
| (003) | 79.23 deg |

Table 9: Theoretical $L1_0$-Mn-Ga peak positions for $\lambda = 1.5419$ nm.

[105] H. Niida et al. In: *Journal of Applied Physics* 79.8 (1996)

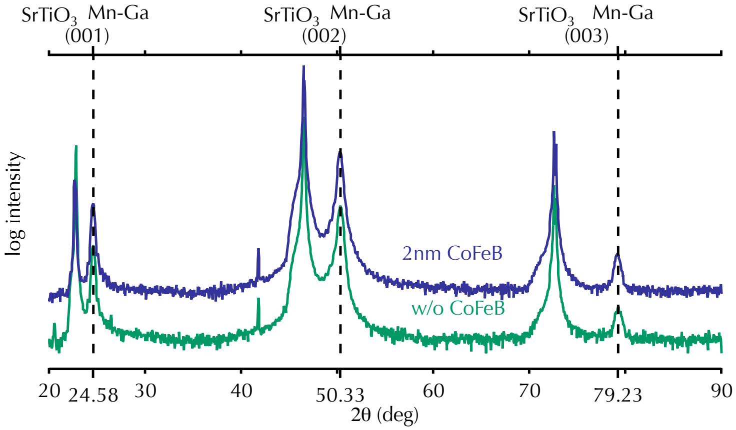

Figure 37: XRD scans of $Mn_{1.6}Ga$ thin films on $SrTiO_3$ without (green) and with a 2 nm (blue) Co-Fe-B interlayer.

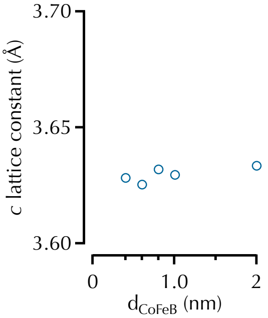

Figure 38: $Mn_{1.6}Ga$ $c$ lattice constant depending on the Co-Fe-B interlayer thickness.

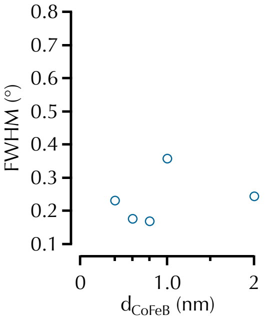

Figure 39: FWHM of the fundamental (002) $Mn_{1.6}Ga$ reflex depending on the Co-Fe-B interlayer thickness $d_{CoFeB}$.

the orientation of the grains.

By taking a closer at the (001) and (002) reflexes, we find that Laue oscillations are visible (cf. Figure 40). Laue oscillations are sensitive to the crystalline disorder of thin films and based on the interference of the diffracted x-ray from parallel crystal planes. The thickness of the crystalline-ordered film can be calculated by means of Equation (9). By comparing the obtained values with the data from the XRR measurement, one recognizes that both values are around 23 nm. The equal thickness suggests that the space between the two interfaces is thoroughly crystallized. Combined with the results of the textured order investigations, a perfectly crystalline thin film is found for values of around 830.

To prove the $L1_0$ phase, pole figure measurements were carried out to examine the appearance of the (011) reflex. In Figure 41 the pole figure scan of a $Mn_{1.6}Ga$ sample is depicted. The $2\theta$ angle was fixed at 33.65 deg. For each tilt angle $\Psi$ between 0 deg and 90 deg the sample was rotated by $\Phi$ from 0 deg to 360 deg. The scan showed no visible (011) reflex, only foothills of a substrate reflex. For this reason, the $L1_0$ crystal structure has been proven. Additionally, the Eulerian cradle can be used to investigate in-plane reflexes like the (202) peak. With the position of this reflex the in-plane lattice constant $a$ can be determined. Therefore, the sample with an 0.8 nm thick Co-Fe-B interlayer and a magnetron sputtered MgO layer and the sample with a 1 nm thick Co-Fe-B interlayer and an e-beam evaporated MgO layer were used. The (202) reflex of the sample with 0.8 nm Co-Fe-B was found at 70.74 deg. The corresponding $a$ parameter is 3.91 Å. The

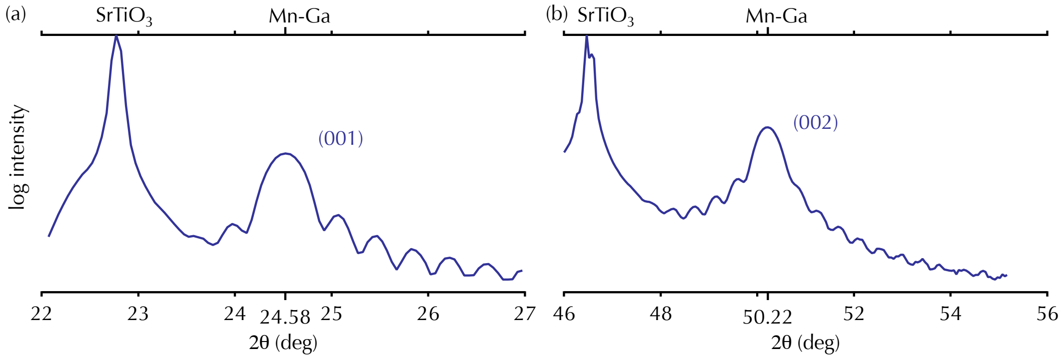

Figure 40: Visible Laue oscillations of the (a) (001) and (b) (002) reflexes for a $Mn_{1.6}Ga$ (23 nm)/Co-Fe-B (0.8 nm)/MgO (2.3 nm) stack on $SrTiO_3$. The deposition temperature was set to 520 °C.

sample with 1 nm Co-Fe-B revealed the (202) reflex at 70.74 deg. Therefore, the lattice constant $a$ is 3.91 nm. In addition, the (200) peak was also investigated. The position was determined to be 46.40 deg and the $a$ lattice constant to be 3.91 Å. Our obtained values fit well with the data reported by Niida et al.[106] The marginal difference of the results is most likely based on the mismatch between $SrTiO_3$ and Mn-Ga. The variation of the $a$ lattice constant with the composition is not as distinct as for the $c$ parameter.[107]

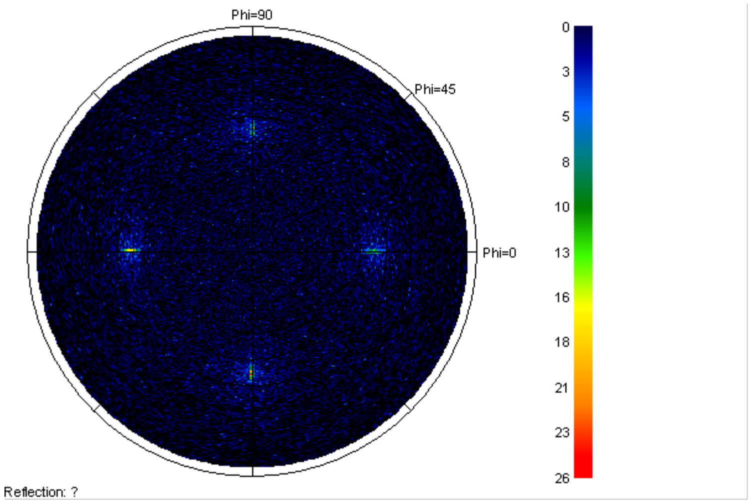

Figure 41: Pole figure scan of a $Mn_{1.6}Ga$ thin film on $SrTiO_3$ substrate. The film thickness was 23 nm and the sample was capped by 2.3 nm MgO. Between the Mn-Ga and the MgO, an 0.8 nm thick $Co_{40}Fe_{40}B_{20}$ layer was inserted. The deposition temperature was chosen to be 520 °C for the $Mn_{1.6}Ga$ layer, whereas the deposition of the two additional films took place at RT. The fixed angle is set to the (011) peak position at $2\theta = 33.65$ deg.

[106] H. Niida et al. In: *Journal of Applied Physics* 79.8 (1996)

[107] H. Niida et al. In: *Journal of Applied Physics* 79.8 (1996)

## Chemical and magnetic characteristics

After the crystallographic properties had been analyzed, we investigated the chemical and magnetic characteristics. X-ray absorption spectroscopy (XAS) is the simplest non-destructive way to obtain information about the chemical structure. Additionally, the obtained x-ray magnetic circular dichroism (XMCD) provides insight into the element-specific magnetic moment. Figure 42 illustrates the Mn-XA spectra of our samples with different interlayer thicknesses. In addition, the spectrum of an intentionally oxidized Mn thin film was added for comparison. On the $L_3$ as well as on the $L_2$ resonance a multiplet structure is visible, pointing to the formation of $Mn_1O_1$. Taking a closer look at the other Mn spectra, we find that a slight shoulder (indicated by a dashed line) at an energy above that of the $L_3$ resonance is present for samples with an Co-Fe-B interlayer thickness below 0.8 nm. The absorption spectra are not distinct enough to distinguish between MnO, $MnO_2$, and $Mn_2O_3$.[108] However, for Co-Fe-B thicknesses from 0.8 nm to 2 nm the Mn spectra fit in well with those of Mn in the metallic state. To investigate the influence of the deposition method of the MgO barrier on the formation of Mn–O, two samples with an e-beam evaporated MgO barrier were prepared. The deposition method of the Mn-Ga remained the same. One of the samples was prepared without a Co-Fe-B interlayer and the other one with 1 nm Co-Fe-B. On top a 2.3 nm thick MgO layer was e-beam evaporated to prevent the stack from

[108] S. Voss et al. In: *Physical Review B* 75.4 (2007)

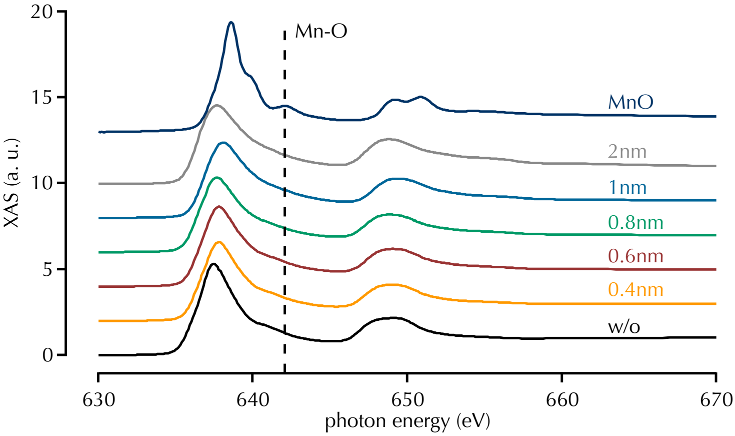

Figure 42: Normalized Mn-XAS (postedge jump height $\eta = 1$) of $Mn_{1.6}Ga$ thin films with a Co-Fe-B interlayer with various thicknesses on $SrTiO_3$ substrates. The MgO capping was sputter deposited at room temperature. The samples were measured at BL 6.3.1 at room temperature.

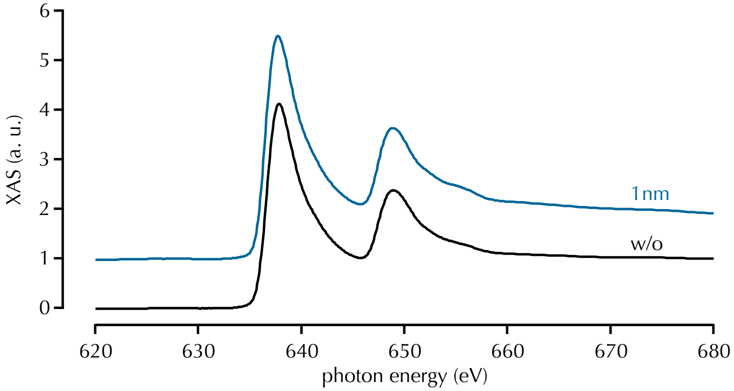

Figure 43: Normalized Mn-XAS (postedge jump height $\eta = 1$) of $Mn_{1.6}Ga$ thin films without and with a 1 nm Co-Fe-B interlayer on $SrTiO_3$ substrates. The MgO capping was prepared by e-beam deposition at room temperature. The samples were measured at BL 6.3.1 at room temperature.

oxidizing. The resulting Mn-XA spectra of both samples are illustrated in Figure 43. Closer inspection reveals the absence of any evidence for Mn–O. Therefore, the deposition method of the barrier is an essential factor for the formation of Mn–O. Sputter deposition is compared to the e-beam deposition, a highly energetic process that assists oxidation of Mn due to plasma damage. Besides the XA spectra, we carried out XMCD measurements. Figure 44 shows the XMCD signal normalized to the postedge jump height (i.e., $\eta = 1$), which increases with increasing Co-Fe-B thickness. The XMCD data accord with the XAS measurements and show that the interfacial magnetic Mn moment increases with increasing Co-Fe-B thickness. Another interesting outcome

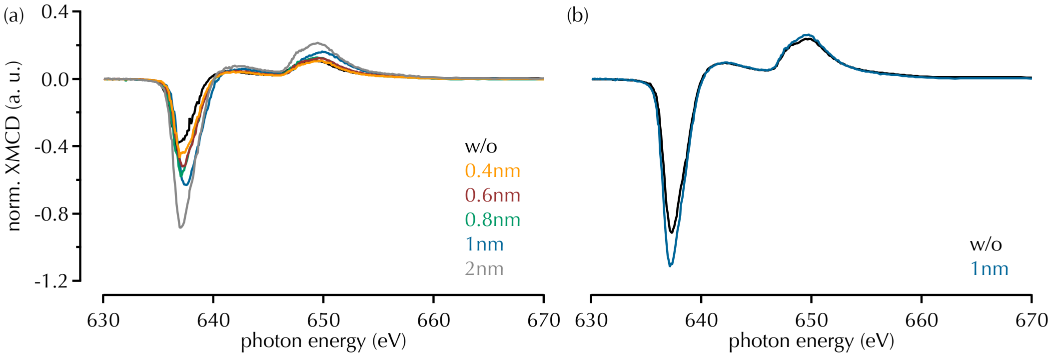

Figure 44: Normalized Mn-XMCD spectra ($\eta = 1$) for samples with (a) magnetron sputtered MgO capping and (b) e-beam evaporated MgO capping on $SrTiO_3$ substrates measured at BL 6.3.1.

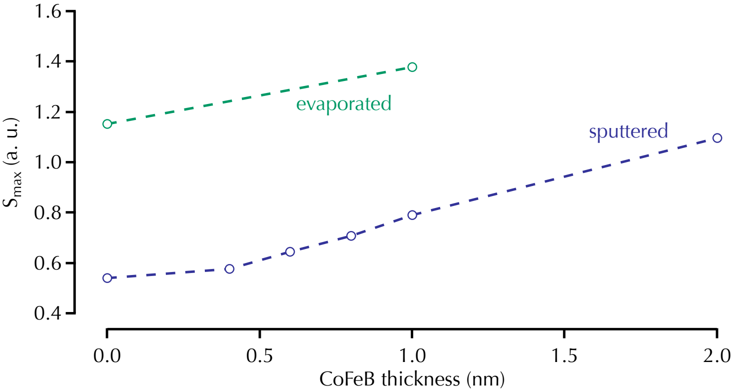

Figure 45: Maximum XMCD signal $S_{max}$ depending on the Co-Fe-B thickness for samples with e-beam evaporated (green) and magnetron sputtered (blue) MgO capping on $SrTiO_3$ substrates.

is proof that the Mn atoms on both sublattices react with the $O_2$, otherwise the magnetic moment would increase due to a lower compensation of both Mn magnetic moments. The XMCD amplitudes on the Mn-$L_{3,2}$-edges corresponds to the magnetic moment of Mn. The resulting total magnetic moment for Mn (sum of the orbital and spin magnetic moment) shows the same qualitative behavior as the maximum intensity $S_{max}$. The $m^{tot}$ from this evaluation results in $m^{tot}_{\mathrm{Mn}} = 1.83(3)\,\mu_{\mathrm{B}}$ for, e.g., $d_{\mathrm{CoFeB}} = 2\,\mathrm{nm}$. Thus, $m^{tot}_{\mathrm{Mn}}$ is obtainable from the maximum XMCD signal $S_{max}$ by $m^{tot}_{\mathrm{Mn}} = S_{max} \cdot (1.60(3)\,\mu_{\mathrm{B}})$. Figure 45 illustrates $S_{max}$ depending on the Co-Fe-B thickness. The signal for samples with e-beam evaporated MgO is higher for both Co-Fe-B thicknesses compared to samples with magnetron sputtered MgO. Thus, even if the XA spectra show no visible evidence of Mn–O there is still a difference in the XMCD signals. Another characteristic can be determined via XMCD, the alignment of the respective magnetic moments of Co, Fe, and Mn. The XMCD signal is the difference between excited spin-up and spin-down electrons. By comparing the sign of the $L_3$ signal for Co, Fe, and Mn the alignment could be obtained. We determined a parallel alignment of the Co-Fe-B and $Mn_{1.6}Ga$ magnetic moments (not shown).

Element-specific hysteresis loops were carried out to investigate the magnetic properties of the $Mn_{1.6}Ga$ and Co-Fe-B layer. Therefore, the beamline energy was set on the $L_3$-edge of the respective element. The orientation of the sample in relation to the magnetic field was 30 deg and 90 deg to obtain an in-plane and out-of-plane configuration. Figure 46 (a) compares the Mn

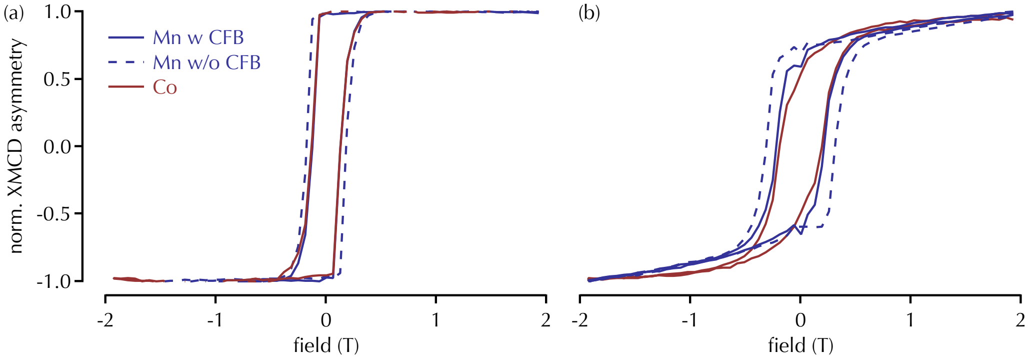

Figure 46: Element-specific full hysteresis loops of Mn (blue) for a sample with (bold) and without (dashed) 1 nm Co-Fe-B interlayer for an a) out-of-plane configuration and b) in-plane configuration (30 deg grazing incidence). Additionally, a Co (red) hysteresis for both field configurations is added to determine the magnetization direction of the Co-Fe-B layer.

hysteresis loop of a sample with a 1 nm and without a Co-Fe-B interlayer on the one hand and the Co hysteresis for out-of-plane configuration on the other hand. The sample without a Co-Fe-B layer reveals a higher coercive field than the sample with Co-Fe-B. This behavior was already reported by Kubota et al.[109] They suggest that the soft-magnetic character of the Co-Fe-B lowers the coercivity of the Mn-Ga layer. The interesting result is that the Mn-Ga and the Co-Fe-B layers reveal the same coercive field. The matching coercivity points to a magnetic pinning of the Co-Fe-B layer on the Mn-Ga layer. To investigate this property more clearly, hysteresis loops were carried out for a 30 deg grazing incidence configuration. Figure 46 (b) illustrates the corresponding hysteresis loops. The coercive field of the Co and Mn still show the same value, suggesting a pinning even for grazing incidence. It is noteworthy that a 1 nm $Co_{40}Fe_{40}B_{20}$ thin film usually requires a post-annealing process to obtain a PMA. Thus, the deposition of Co-Fe-B on a hard-magnetic ferrimagnetic layer increases the coercivity and makes a post-annealing process unnecessary. In addition, Tsai et al.[110] reported a superparamagnetic state for 1 nm thick Co-Fe-B thin films at RT. By the pinning effect the superparamagnetic state at RT could be avoided. The other samples with different Co-Fe-B thicknesses show the same correlation of the Co and Mn coercive fields. In Figure 47 the out-of-plane coercive fields of the Co-Fe-B and $Mn_{1.6}Ga$ layer are shown depending on the Co-Fe-B thickness. The Co hysteresis loop of a sample with a 0.4 nm Co-Fe-B thin film was not detectable due to the small amount of Co-Fe-B in these samples. For an interlayer

[109] T. Kubota et al. In: *Applied Physics Express* 5.4 (2012)

[110] C. C. Tsai et al. In: *IEEE Transactions on Magnetics* 50.1 (2014)

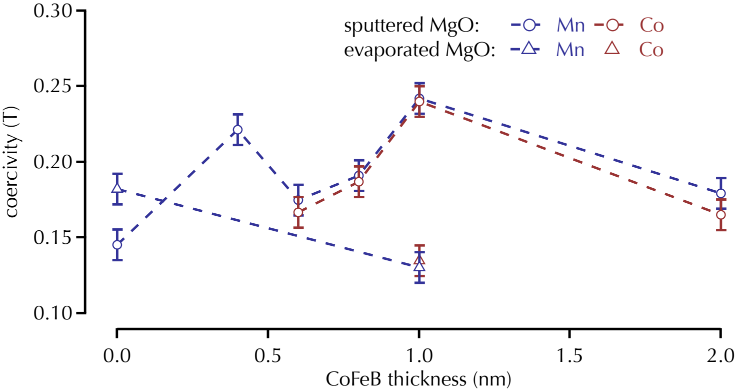

Figure 47: Relation between the Mn (blue) and Co (red) coercive fields for different Co-Fe-B interlayer thicknesses in a $Mn_{1.6}Ga$/ Co-Fe-B/ MgO stack on $SrTiO_3$. The orientation of the magnetic field was perpendicular to the film plane.

thickness from 0.6 nm to 2 nm a Co hysteresis was obtained, but the coercivity differs slightly, within the errors, from that shown by the Mn hysteresis. However, samples with 0.8 nm and 1.0 nm Co-Fe-B interlayer thickness show the same coercivity for Mn and Co. Therefore, up to a Co-Fe-B thickness of 2 nm the magnetic moments of the interlayer are parallel-aligned to the Mn-Ga bottom layer. The perpendicular alignment of the Co-Fe-B interlayer originates from three effects: the stray field of the Mn-Ga film, the exchange coupling at the interface, and the perpendicular magnetic anisotropy of the Co-Fe-B thin film. The influence of exchange coupling and the PMA decrease with increasing Co-Fe-B thickness, whereas the stray field is proportional to the film thickness. In a nutshell, the suppressed oxidation of the Mn-Ga layer and the pinning effect of the Co-Fe-B layer are promising properties for further integration into MTJ's.

### *Transport properties*

As already mentioned in the introduction, the TMR effect was discovered in 1975 by Jullière[111] in Fe/Ge/Co tunnel junctions, where the barrier is semiconducting Ge. By applying a voltage to an MTJ, the electrons tunnel through the barrier from one electrode into the other. The resistance of the stack depends on the alignment of the electrode, for a parallel orientation a low resistance is found and for an antiparallel orientation there is high resistance. The commonly known relation for the effect

[111] M. Jullière. In: *Physics Letters A* 54.3 (1975)

amplitude is

$$\mathrm{TMR} = \frac{\Delta R}{R_{\uparrow\uparrow}} = \frac{R_{\uparrow\downarrow} - R_{\uparrow\uparrow}}{R_{\uparrow\uparrow}}. \tag{39}$$

The ferromagnetic electrodes (Fe and Co) that Jullière used reveal a difference in the number of majority (spin-up) and minority (spin-down) electrons at the Fermi energy.[112] Therefore, these materials and also Ni are spin-polarized (cf. Table 10). The difference in the DOS in both spin channels is based on exchange interaction. For parallel alignment of the electrodes, more majority electrons tunnel from one electrode into the free states of the counter electrode. The contribution of the minority electrons is lower. In the antiparallel alignment, the amount of free states in the counter electrode is lower, thus the current of the majority and minority electrons is lower than in the parallel state. The TMR effect depends on the spin polarization that is given by

$$p = \frac{D_{\uparrow}(E_F) - D_{\downarrow}(E_F)}{D_{\uparrow}(E_F) + D_{\downarrow}(E_F)} \tag{40}$$

with $D_{\uparrow/\downarrow}(E_F)$ the majority/minority DOS at the Fermi energy. The tunnel current is proportional to the product of $D^1(E_F)$ and $D^2(E_F)$, the DOS of electrodes 1 and 2. The current for the parallel and antiparallel states are given by

$$I_{\uparrow\uparrow} = D^1_{\uparrow}(E_F)D^2_{\uparrow}(E_F) + D^1_{\downarrow}(E_F)D^2_{\downarrow}(E_F), \text{ and} \tag{41}$$

$$I_{\uparrow\downarrow} = D^1_{\uparrow}(E_F)D^2_{\downarrow}(E_F) + D^1_{\downarrow}(E_F)D^2_{\uparrow}(E_F). \tag{42}$$

With Equation (39) we found the relation between the TMR effect and the spin polarization

$$\mathrm{TMR} = \frac{R_{\uparrow\downarrow} - R_{\uparrow\uparrow}}{R_{\uparrow\uparrow}} = \frac{I_{\uparrow\downarrow} - I_{\uparrow\uparrow}}{I_{\uparrow\uparrow}} = \frac{2p_1p_2}{1 - p_1p_2}. \tag{43}$$

Since the first observation it took 20 years Moodera et al.[114] was able to reproduce the results in CoFe/$Al_2O_3$/Co tunnel junctions. In 2004, Parkin et al.[115] reported a giant TMR effect for samples with MgO barriers. The reason for the higher TMR effect in MgO based MTJ's is the *coherent* tunneling process (cf. Figures 48 and 49). Let us first consider an amorphous barrier like $Al_2O_3$, here every electronic state (Bloch state) shows equal tunnel probability (cf. Figure 48). This case is called *incoherent* tunneling process and was assumed by Slonczewski[117]. For a crystalline barrier, e.g. (001) MgO, the tunneling process behaves differently. The crystalline *bcc* order of the MgO is achieved when it is deposited

[112] The majority electron is defined as the electron with spin direction parallel-aligned to the external magnetic field, which is large enough to fully saturate the sample.

| material | polarization |
|---|---|
| Co | 34 % |
| Fe | 44 % |
| Ni | 11 % |
| $Mn_{3\text{-}x}Ga$ | 88 % |

Table 10: Experimentally obtained pin polarization of the transition metals in comparison to the theoretically predicted spin polarization of the $Mn_{3\text{-}x}Ga$ compound.[113]

[113] P. M. Tedrow and R. Meservey. In: *Physical Review B* 7.1 (1973); B. Balke et al. In: *Applied Physics Letters* 90.15 (2007)

[114] J. S. Moodera et al. In: *Physical Review Letters* 74.16 (1995)

[115] S. S. P. Parkin et al. In: *Nature Materials* 3.12 (2004)

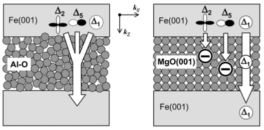

Figure 48: Sketch of the tunneling effect in amorphous (left) and crystalline (right) barriers.[116]

[116] S. Yuasa and D. D. Djayaprawira. In: *Journal of Physics D: Applied Physics* 40.21 (2007)

[117] J. C. Slonczewski. In: *Physical Review B* 39.10 (1989)

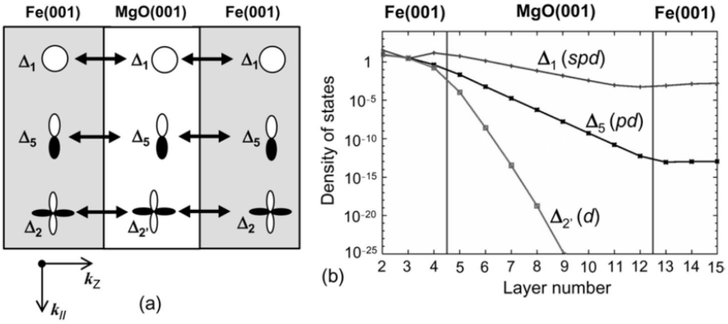

Figure 49: (a) Coupling of wave functions between the Bloch states in Fe and the evanescent states in MgO for the $k_{\parallel} = 0$ direction. (b) Tunneling DOS of majority-spin states for $k_{\parallel} = 0$ in Fe (001)/ MgO (001) (8 ML)/ Fe (001) with parallel magnetic state.[118]

on Fe or other ferromagnetic materials with low lattice mismatch. It has to be noted that the lattice mismatch between MgO and Mn-based Heusler compounds is around is above 7 %. For a crystalline barrier there are three kinds of evanescent states in the band gap, $\Delta_1$, $\Delta_5$, and $\Delta_2$.[119] If the symmetry of the wave functions is conserved during tunneling, the $\Delta_1$ Bloch states of the Fe couple with the evanescent $\Delta_1$ states of the MgO. The longest decay length in the parallel state of the electrodes reveals the $\Delta_1$ evanescent state and it is the dominant spin channel. Due to the higher spin polarization of the $\Delta_1$ electrons a higher TMR effect can be assumed. It should be noted that this is also valid for *bcc* ferromagnets, *bcc* Fe-Co, *bcc* Co-Fe-B and some of the Heusler compounds. However, a finite tunneling current is also present in the antiparallel state of the electrodes, but the conductance is much lower compared to the parallel state. This tunneling process is called *coherent* (cf. Figure 48). The coherent tunneling process is very sensitive to the structure at the barrier interface. Even a monolayer (ML) of oxidized electrode material leads to ineffectively coupling of the $\Delta_1$ states and thus reduces the TMR effect drastically.

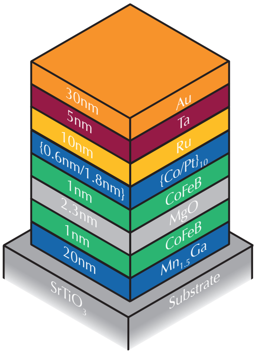

Figure 50: TMR stack with $Mn_{1.5}Ga$ bottom electrode and Co/Pt multilayer counter electrode.

To investigate the transport properties of the $Mn_{3-x}Ga$ Heusler compound, we prepared $Mn_{1.5}Ga$ (20 nm)/ $Co_{40}Fe_{40}B_{20}$ (1 nm)/ MgO (2.3 nm)/$Co_{40}Fe_{40}B_{20}$ (1 nm)/ $\{Co/Pt\}_{10}$ (24 nm)/ conduction layer (45 nm) MTJ's on $SrTiO_3$ (cf. Figure 50). The deposition temperature of the $Mn_{1.5}Ga$ was 550 °C, whereas the other layers were fabricated at RT. The tunnel junctions were prepared by UV-lithography and $Ar^+$ beam etching. The element sizes were

[118] S. Yuasa and D. D. Djayaprawira. In: *Journal of Physics D: Applied Physics* 40.21 (2007)

[119] S. Yuasa and D. D. Djayaprawira. In: *Journal of Physics D: Applied Physics* 40.21 (2007)

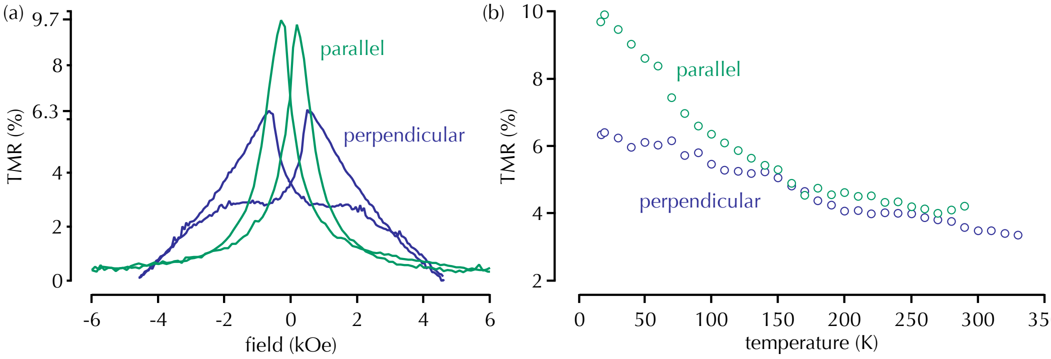

Figure 51: (a) TMR effect at 15 K of a $Mn_{1.5}Ga$/Co-Fe-B/MgO/Co-Fe-B/$\{Co/Pt\}_{10}$ tunnel junction on $SrTiO_3$ for in-plane (green) and out-of-plane (blue) configuration. (b) TMR over temperature for in-plane (green) and out-of-plane (blue) configuration.

100 µm², 225 µm² and 625 µm². These structures were capped by Ta (5 nm)/Au (30 nm) contact pads to enable contacting via Au bond wires. All measurements were carried out using a conventional two probe technique in a closed-cycle helium cryostat (Oxford Cryodrive 1.5) with a temperature range from 15 K to 330 K.

The simple growth conditions for Co/Pt multilayers are the reason why it was chosen as counter electrode. Kugler et al.[120] reported a perpendicularly magnetized Co/Pt multilayers on a Ta seed layer on $SiO_2$ substrates. In addition, they reported the successful synthesis of a Co/Pt multilayer counter electrode in direct contact with the MgO barrier.

Transport measurements only exhibited a TMR effect for MTJ's with an area of 100 µm² on $SrTiO_3$ substrate. Figure 51 (a) illustrates the in-plane and out-of-plane TMR effect at 15 K and Figure 51 (b) the temperature dependence of the TMR effect. The in-plane TMR effect at 15 K is about 9.7 % and higher than the out-of-plane effect with 6.3 %. A closer look at the out-of-plane measurements suggests that the hard electrode has an in-plane component. This suggestion is based on the linear decrease with increasing external magnetic field. Comparing the hysteresis of a plain $Mn_{1.5}Ga$ thin film (cf. Figure 27 on page 41) and the results of Kugler et al.[121] for Co/Pt multilayers, the bottom electrode is the hard electrode and the top electrode the soft electrode. That way the $Mn_{1.5}Ga$ layer would exhibit an in-plane component. However, previous measurements showed no evidence for an in-plane component. For this reason, we again prepared a plain thin film of $Mn_{1.5}Ga$ on an MgO and a $SrTiO_3$ substrate. The corre-

[120] Z. Kugler et al. In: *Journal of Applied Physics* 111.7 (2012)

[121] Z. Kugler et al. In: *Journal of Applied Physics* 111.7 (2012)

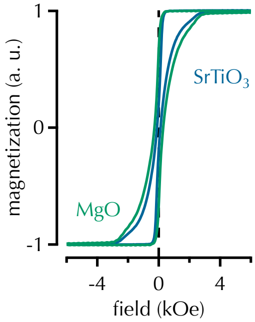

Figure 52: Out-of-plane hysteresis loops of a $Mn_{1.5}Ga$ thin film on MgO (green) and $SrTiO_3$ (blue) substrate.

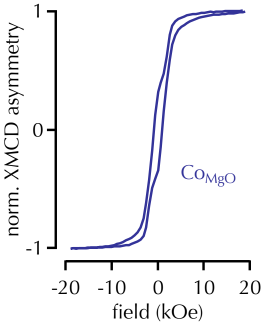

Figure 53: Element-specific Co hysteresis loop of a magnetic tunnel junction with Co/Pt counter electrode on MgO.

sponding hysteresis loops are depicted in Figure 52. The external magnetic field was applied perpendicular to the sample surface. Samples prepared on MgO and $SrTiO_3$ revealed a small coercivity of 303.3 Oe and 153.7 Oe, respectively. To determine the coercive field of the Co/Pt multilayers, we carried out element-specific hysteresis loops on MTJ's containing of $Mn_{2.5}Ga$/ $Co_{40}Fe_{40}B_{20}$/ MgO/ $Co_{40}Fe_{40}B_{20}$/ $\{Co/Pt\}_{10}$ on MgO. The obtained coercive field is 950 Oe (cf. Figure 53).[122] Therefore, the $L1_0$-Mn-Ga is the soft electrode and the Co/Pt multilayers the hard electrode. Due to this non-emerging antiparallel state of the electrodes a low TMR effect is achieved. In addition, due to the weak PMA of the electrodes, the in-plane TMR effect exhibits higher values than the out-of-plane TMR effect (cf. Figure 51 (b)).

The PMA of Co/Pt multilayer structures are sensitive to the respective thickness of the Co and Pt and also to the repetitions. However, for a first attempt the Co/Pt multilayer structure is a suitable option, due to the good growth conditions on top of the MgO barrier. Nonetheless, the difficult preparation of the multilayers and the required strict adherence to layer thickness requirements reduces its applicability.

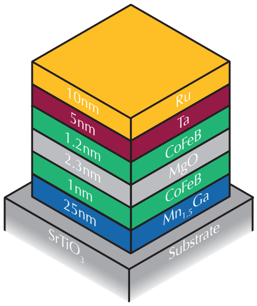

Figure 54: TMR stack with $Mn_{1.5}Ga$ bottom electrode and 1.2 nm Co-Fe-B counter electrode.

To increase applicability and simplify the preparation process, we exchanged the Co/Pt multilayers by a 1.2 nm thick $Co_{40}Fe_{40}B_{20}$ thin film (cf. Figure 54). Thus the MTJ's on MgO and $SrTiO_3$ consist of $Mn_{1.5}Ga$ (25 nm)/ $Co_{40}Fe_{40}B_{20}$ (1 nm)/ MgO (2.3 nm)/ $Co_{40}Fe_{40}B_{20}$ (1.2 nm)/ conduction layer (15 nm). Thin Co-Fe-B layers in contact with an MgO barrier exhibit a magnetization direction perpendicular to the film plane. The interface anisotropy is based on the hybridization of the MgO 2*p* orbitals with the 3*d* orbitals of the Co and Fe.[123] The hard-magnetic $Mn_{1.5}Ga$ layer was deposited at 550 °C to obtain a PMA. The other layers were prepared at RT. After the synthesis of the MTJ stack, an additional ex-situ post-annealing process was carried out at 360 °C for 1 h. During the heating and cooling procedure an external magnetic field of 6500 Oe was applied perpendicular to the sample surface. Because of the post-annealing, the PMA of the soft-magnetic Co-Fe-B layer was obtained and a higher crystallization of the MgO barrier was achieved.[124]

The first transport measurements revealed a TMR effect for samples on $SrTiO_3$ and MgO, for tunnel junctions from 100 $\mu m^2$ to 625 $\mu m^2$. Figure 55 presents the TMR effect at 300 K for a 100 $\mu m^2$ MTJ on MgO and $SrTiO_3$ substrates. The TMR effect is twice as high as for samples with a Co/Pt multilayer counter

[122] It has to be noted that the stack structure was quite different with regard to the bottom electrode. However, the bottom electrode should not affect the top electrode.

[123] S. Ikeda et al. In: *Nature Materials* 9.9 (2010)

[124] Due to the further annealing process, the preparation process was not really simplified. But the positive aspects overcome the negative aspects.

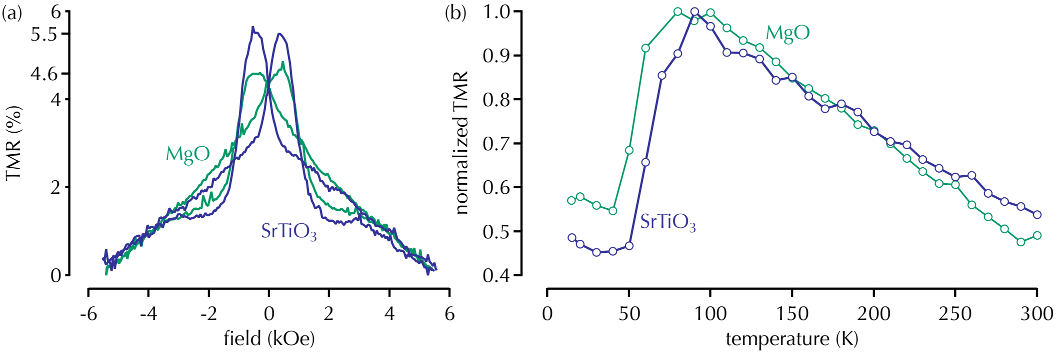

Figure 55: (a) TMR effect at 300 K of $Mn_{1.5}Ga$/Co-Fe-B/MgO/Co-Fe-B tunnel junctions on MgO (green) and $SrTiO_3$ (blue) substrates. (b) TMR over temperature for samples on MgO (green) and $SrTiO_3$ (blue) substrates.

electrode - although the shape of the TMR curve differs, indicating to an almost antiparallel state of the electrodes. Figure 56 shows the hysteresis loop of the MTJ on MgO substrate. The signal of the counter electrode is not visible in the hysteresis loop. Consequently, the increasing slope with decreasing field in the TMR loop and the non-visibility of the soft electrode in the hysteresis loop suggest a paramagnetic behavior of the Co-Fe-B thin film. Recently, Tsai et al.[125] reported a superparamagnetic state in thin Co-Fe-B layers, where the blocking temperature $T_B$ depends on the Co-Fe-B thickness. They reported a superparamagnetic state for a 1 nm thick Co-Fe-B layer at RT, whereas a 1.2 nm thick layer remains ferromagnetic up to 320 K. In our case, the 1.2 nm thick counter electrode is superparamagnetic at 300 K for samples on MgO. This suggests a discrepancy of 1 Å to 2 Å between the nominal and real film thickness. However, by cooling down the sample below 300 K the superparamagnetic effect vanishes. In Figure 55 (b) the TMR effect over temperature is shown. The TMR effect increases with decreasing temperature and achieves a maximum value around 100 K. Further cooling led to a minimal TMR effect at 30 K (40 K) for samples on $SrTiO_3$ (MgO).

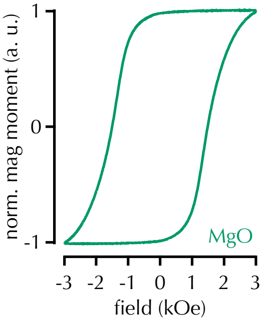

Figure 56: Hysteresis loop of a $Mn_{1.5}Ga$ based tunnel junction with Co-Fe-B counter electrode on MgO (green).

The variation of the major loops at different temperatures provides insight into the present effect. Figure 57 illustrates the major loops at three temperatures. We will only consider the sample on $SrTiO_3$ substrate for interpretation.[126] Starting at 300 K with a decreasing external magnetic field from positive to negative values, the major loop shows a linear increase of the TMR effect with decreasing external field and around zero field an abrupt switching of the soft electrode. At 90 K the TMR effect increased to the maximum value and the abrupt switching at low fields is

[125] C. C. Tsai et al. In: *IEEE Transactions on Magnetics* 50.1 (2014)

[126] The behavior of samples on MgO is analogous but with a small difference in the TMR ratio.

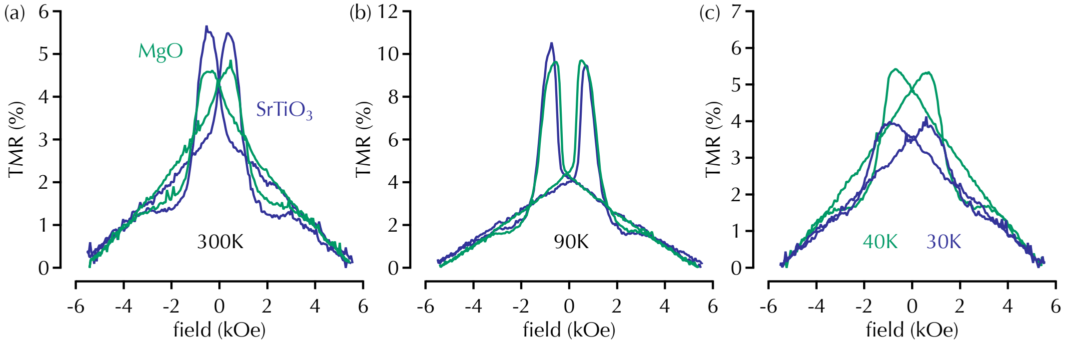

Figure 57: TMR effect of $Mn_{1.5}Ga$ (25 nm)/Co-Fe-B (1 nm)/MgO (2.3 nm)/Co-Fe-B (1.2 nm) tunnel junctions on MgO (green) and $SrTiO_3$ (blue) substrates at (a) 300 K (b) 90 K and (c) 40 K and 30 K.

more distinct (cf. Figure 57 (b)). However, at 30 K the TMR effect reaches almost the same value as at 300 K (cf. Figure 57 (c)). Here again, a linear increase of the TMR effect with decreasing external magnetic field is found. This time the superparamagnetic state can be excluded. Tsai et al.[127] reported a coercivity crossover of Co-Fe-B thin films with different layer thicknesses when cooled

[127] M. C. Tsai et al. In: *Journal of Applied Physics* 113.17 (2013)

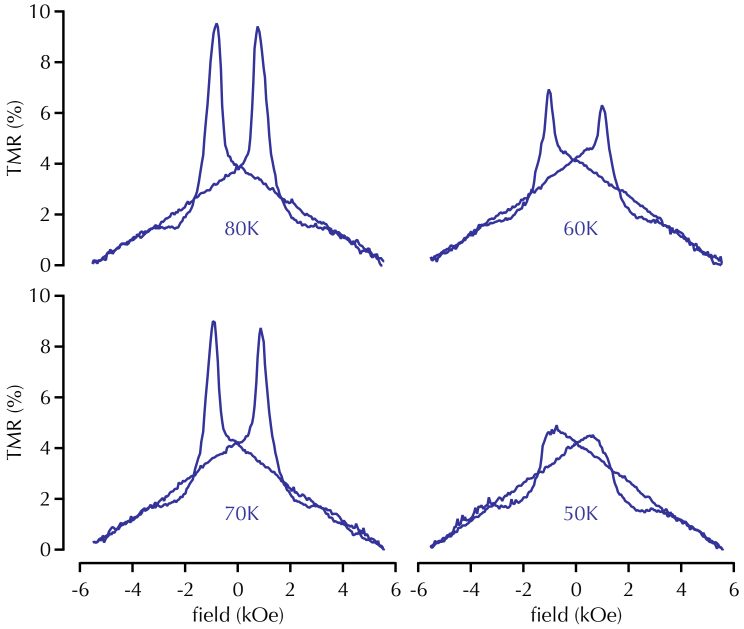

Figure 58: TMR curves during the coercive field crossover of a $Mn_{1.5}Ga$ (25 nm)/Co-Fe-B (1 nm)/MgO (2.3 nm)/Co-Fe-B (1.2 nm) MTJ on $SrTiO_3$ (blue) substrate.

down to low temperatures (LT's). For example, a Co-Fe-B thin film with a nominal thickness of 1.2 nm reveals a higher coercive field at RT than a 1 nm thin film. By cooling down, the coercivity changes differently for the two layers and the 1 nm thin film becomes the hard electrode. Compared to the coercive field of the Mn-Ga layer, the Co-Fe-B electrodes show a stronger temperature dependence. For that reason the 1.2 nm thick Co-Fe-B layer becomes the hard electrode at 50 K. In Figure 58, the corresponding major loops at different temperatures are shown. At 80 K a clear distinction between hard and soft electrode can be made. By decreasing the temperature, the coercivity of the soft layer increases faster than the coercive field of the hard layer, resulting in a crossover around 50 K.

However, we only obtained a TMR effect for samples with a Co-Fe-B interlayer, but the TMR ratio was lower than the theoretical expectations. Therefore, a reason for the low TMR effects needs to be found. Mn–O or the lattice mismatch between Mn-Ga can be neglected due to the Co-Fe-B interlayer. One last possible cause is the diffusion of Boron. Kurt et al.[128] investigated the B diffusion in Ta/CoFeB/MgO/CoFeB/Ta tunnel junctions, with thick Co-Fe-B layers (20 nm and 60 nm) and high annealing temperatures up to 400 °C. They reported a diffusion of B away from the MgO barrier into the 10 nm thick Ta layer. Thus, the Ta film acts as a B absorber. Especially, when the ionic radius of one material is much smaller than the radii of other materials, a diffusion takes place.[129] This raises questions about the B diffusion in our tunnel junctions. On top of the Co-Fe-B counter electrode a 5 nm thick Ta layer is deposited but the bottom Co-Fe-B layer is in contact with the Mn$_{1.5}$Ga layer. Thus for the bottom Co-Fe-B layer the B absorber is missing. As a consequence, the B probably diffuses to the MgO interface.

## Auger electron spectrocopy

The interdiffusion of the B was investigated by means of Auger electron spectroscopy (AES) depth profiles. Because of the penetration depth of only 1 nm to 2 nm the AES reveals a higher surface sensitivity compared to XRF and provides insight into the local element distribution. To investigate a multilayer stack a AES depth profile needs to be carried out. Therefore, Ar ions are used to etch atomic layer by atomic layer. The kinetic energy $E_{kin}$ of the AE is well-defined and directly related to the difference in core-level energies. For an exemplary $KL_1L_2$ transition, the

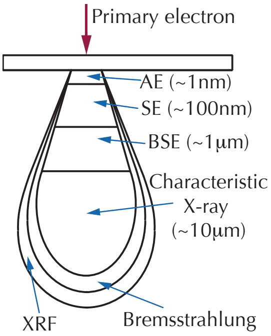

Figure 59: Interaction volume.

[128] H. Kurt et al. In: *Applied Physics Letters* 96.26 (2010)

[129] H. Kurt et al. In: *Applied Physics Letters* 96.26 (2010)

kinetic energy is given by

$$E_{kin} = E_K - E_{L_1} - E_{L_2} \tag{44}$$

The main difference between the Auger process and the photoemission is the formation of an additional core hole. For this reason, an additional term $\Delta E$ has to be added to describe the many-electron effects,

$$E^Z_{KL_1L_2} = E^Z_K - E^Z_{L_1} - E^Z_{L_2} - \Delta E(L_1L_2) \tag{45}$$

with $Z$ the atomic number. The correction term $\Delta E(L_1L_2)$ is small.

In order to determine the interdiffusion in our MTJ's, we carried out an AES depth profile on a $Mn_{1.5}Ga$ (25 nm)/Co-Fe-B (1 nm)/MgO (2.3 nm)/Co-Fe-B (1.2 nm)/Ta (5 nm)/Ru (10 nm) MTJ on an MgO substrate. Figure 60 illustrates the corresponding scan. The important element is B, which is marked red. Starting from the top we found a Ru and Ta signal together with $O_2$, suggesting an interdiffusion of both layers. Additionally, the $O_2$ signal is evidence of the formation of Ta–O.[130] The B signal starts together with the Ta signal. This is no evidence of diffusion, but induced by the overlap of the $E^{\mathrm{Ta}}_{NNN}$ and $E^{\mathrm{B}}_{KLL}$ energies at around 180 eV. For this reason, the B diffusion in the top part of the MTJ could not be examined. However, in the bottom part, i.e., below the barrier, no disturbing Ta signal is present. The Mg and $O_2$ signals increase slowly and show an abrupt decrease. This is a characteristic behavior and corresponds to a good crystalline barrier. Next to the barrier the highest B signal is observed. Therefore, a B migration away from the MgO barrier did not occur, but

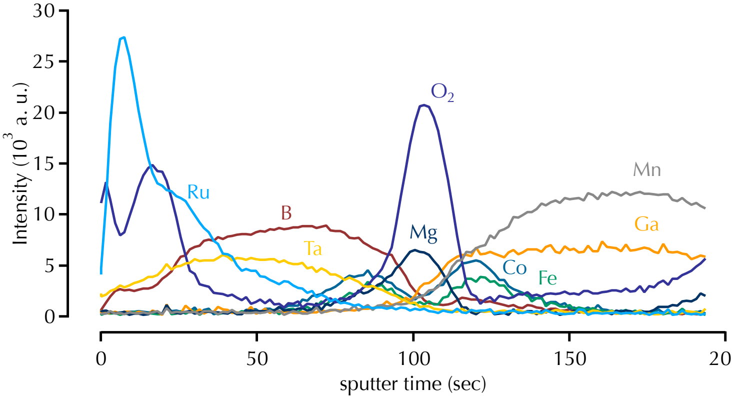

Figure 60: AES depth profile of a $Mn_{1.5}Ga$ (25 nm)/Co-Fe-B (1 nm)/MgO (2.3 nm)/Co-Fe-B (1.2 nm) tunnel junction on an MgO substrate. The post-annealing temperature was set to 360 °C.

[130] Ru reveals a lower oxygen affinity.

at least there is no B signal inside the barrier. The B reduces the spin polarization at the MgO/Co-Fe-B interface. Another feature seen in the AES depth profile is the occurrence of Mn and Ga at the barrier interface. In fact the Ga signal rises before the signal of the Mn and Co-Fe-B starts. Therefore, the Ga, but also the Mn, diffuse through the Co-Fe-B layer. ViolBarbosa et al.[131] reported the occurrence of Ga–O in $Mn_{1.64}Ga$/MgO stacks. The diffusion of Ga and the probable formation of Ga–O lower the spin polarization at the barrier interface drastically. For this reason, the achieved TMR ratios were rather low. Additionally, the diffusion changes the composition of the electrode and the interface termination (MnMn/MgO or MnGa/MgO).[132]

## The $Co_2FeAl$ interlayer

In the previous section the insertion of a thin Co-Fe-B interlayer between the $Mn_{3\text{-}x}Ga$ electrode and the MgO barrier was discussed.[133] A major disadvantage of Co-Fe-B is the diffusion of B during the post-annealing process. An alternative material with out-of-plane magnetization and high spin polarization is $Co_2FeAl$. To achieve a PMA the film thickness has to be decreased below 1 nm.[134] A reasonably high TMR effect of 91 % was reported for $Co_2FeAl/MgO/Co_{20}Fe_{60}B_{20}$ tunnel junctions. Additionally, a low damping parameter of $\alpha = 0.004$ and a high anisotropy energy of $K = 3 \times 10^5\,\mathrm{J\,cm^{-3}}$ were reported.[135] Therefore, $Co_2FeAl$ is a promising candidate to serve as an interlayer as well as counter electrode in $Mn_{3\text{-}x}Ga$ based MTJ's.

To INVESTIGATE THE PROPERTIES of a $Co_2FeAl$ interlayer, we deposited a 25 nm thick $Mn_{1.5}Ga$ thin film on $SrTiO_3$ and MgO substrates at 550 °C. This composition exhibits the advantages of low surface roughness and a low amount of Mn–O at the barrier interface due to deposition from a composite target. Afterwards a 1 nm thick $Co_2FeAl$ thin film was added, here the deposition temperature was around RT to achieve a comparable process to that of the Co-Fe-B interlayer. Additionally, the deposition of thin films below 1 nm on heated substrate is difficult due to the vaporization of the material. To investigate the influence of the barrier on the $Co_2FeAl$ and vice versa a 2.3 nm MgO layer was deposited on top of the stack, also at RT.

[131] C. E. ViolBarbosa et al. In: *Journal of Applied Physics* 116.3 (2014)

[132] Y. Miura and M. Shirai. In: *IEEE Transactions on Magnetics* 50.1 (2014)

[133] M. Glas et al. In: *Journal of Applied Physics* 114.18 (2013)

[134] K.-S. Chae et al. In: *Applied Physics Letters* 103.16 (2013)

[135] Z. Wen et al. In: *Applied Physics Letters* 98.24 (2011); Z. Wen et al. In: *Applied Physics Express* 5.6 (2012)

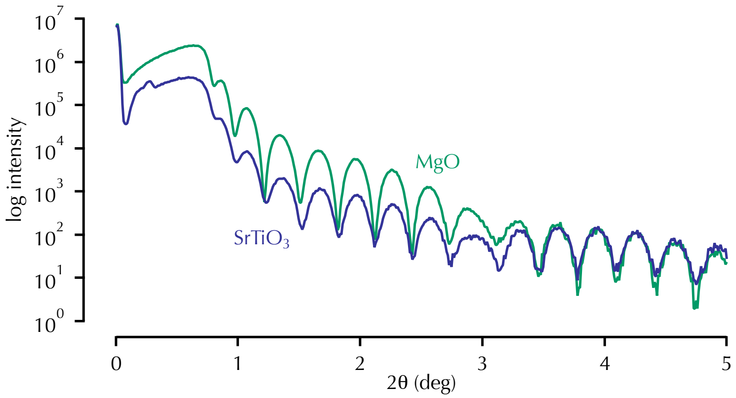

Figure 61: XRR scans of a $Mn_{1.5}Ga$ (25 nm)/$Co_2FeAl$ (1 nm)/MgO (2.3 nm) stack on MgO (green) and $SrTiO_3$ (blue). The deposition temperature of the $Mn_{1.5}Ga$ was 550 °C.

## Surface properties

The surface properties with regard to film roughness were investigated by XRR measurements. Additionally, the film thickness and density were examined. Figure 61 illustrates the obtained XRR scans of a $Mn_{1.5}Ga$ (25 nm)/$Co_2FeAl$ (1 nm)/MgO (2.3 nm) stacks on MgO and $SrTiO_3$.[136] The determined values from the XRR scan are shown in Table 11. The film roughness of the Mn-Ga was lower on MgO substrates. Most likely, the used $SrTiO_3$ substrate revealed a lower crystalline quality. For this reason, the deposited thin films differ in their properties from those on MgO substrate. However, initial investigations showed a low surface roughness of Mn-Ga without ferromagnetic interlayer and with Co-Fe-B interlayer. For this reason, we decided to integrate these stacks into MTJ's.

[136] Nominal film thickness in parentheses.

| layer | MgO | $SrTiO_3$ | MgO | $SrTiO_3$ | MgO | $SrTiO_3$ |
|---|---|---|---|---|---|---|
| | $d$ (nm) | | roughness (nm) | | $\rho$ (g cm$^{-3}$) | |
| $Mn_{1.5}Ga$ | 25.20(5) | 23.42(5) | 0.43(5) | 1.23(5) | 7.24(5) | 7.20(5) |
| $Co_2FeAl$ | 0.99(5) | 0.94(5) | 0.42(5) | 1.22(5) | 6.96(5) | 7.00(5) |
| MgO | 1.60(5) | 1.99(5) | 1.55(5) | 3.07(5) | 3.60(5) | 3.00(5) |

Table 11: Fit parameter obtained from the XRR scan in Figure 61.

## Crystallographic properties

The XRD scans revealed the typical reflexes of the $L1_0$ crystal phase (cf. Figure 62). The Mn-Ga layer shows the fundamental

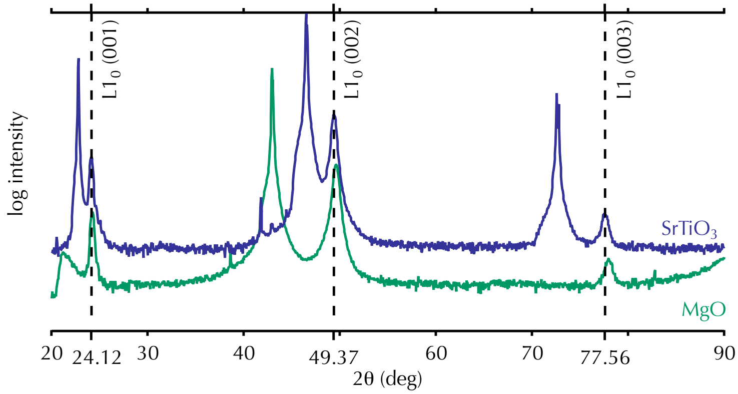

Figure 62: XRD scans of $Mn_{1.5}Ga$ thin films with a 1 nm $Co_2FeAl$ interlayer and a 2.3 nm MgO capping layer on MgO (green) and $SrTiO_3$ (blue).

(002) and super lattice (001) and (003) reflexes, independently of the substrate. The peak positions for the sample on $SrTiO_3$ are 24.12 deg for the (001) and 77.56 deg for the (003) super lattice reflexes. The fundamental reflex can be found at 49.37 deg. These positions correspond to a *c* parameter of 3.69 Å. However, the peak positions for samples on MgO are at higher angles, due to the lateral expansion induced by the substrate. The two super lattice reflexes are visible at 24.23 deg and 77.94 deg and the fundamental peak occurs at 49.59 deg. Therefore, a *c* lattice constant of 3.68 Å is determined. The $Co_2FeAl$ layer shows no influence on the crystal structure of the Mn-Ga. That was expected, due to the results obtained for a Co-Fe-B interlayer. The $Co_2FeAl$ layer induces no reflexes in the XRD scan because of the low thickness. In that way, the real crystal phase of the $Co_2FeAl$ film remains unknown.

## *Chemical and magnetic properties*

The XA and XMCD spectra obtained for $Mn_{1.5}Ga$ samples with a $Co_2FeAl$ interlayer on MgO and $SrTiO_3$ substrates are depicted in Figure 63. From the XA spectra no difference regarding the formation of Mn–O between the two samples is observed. However, the XMCD spectra are more sensitive to the formation of Mn–O. The sample on MgO exhibits a lower $S_{max}$ value compared to the sample on the $SrTiO_3$ substrate.[137] The corresponding magnetic moment per Mn atom is 1.69(3) $\mu_B$ on MgO and 1.84(3) $\mu_B$ on $SrTiO_3$. For this reason, we can conclude that the amount of Mn–O is higher for thin films on MgO. Another explanation

[137] $S_{max}$ is defined as the XMCD signal height.

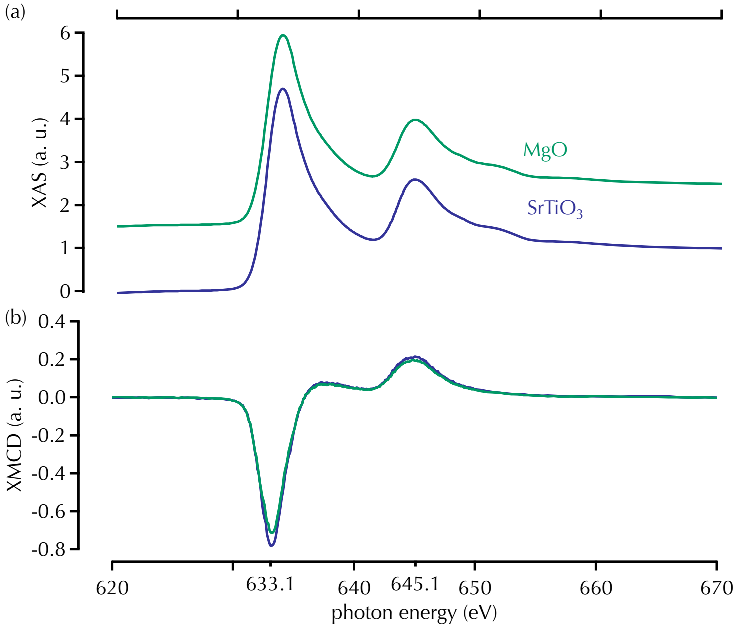

Figure 63: Mn-XA and XMCD spectra of $Mn_{1.5}Ga/Co_2FeAl/MgO$ stacks on MgO (green) and $SrTiO_3$ (blue) measured at BL 6.3.1.

could be higher compensation for samples on MgO. However, the degree of magnetic compensation depends strongly on the crystalline order. Because of the higher crystallinity for thin films on $SrTiO_3$, a higher compensation of the magnetic moment for thin films on MgO is probably not the reason. Comparing the

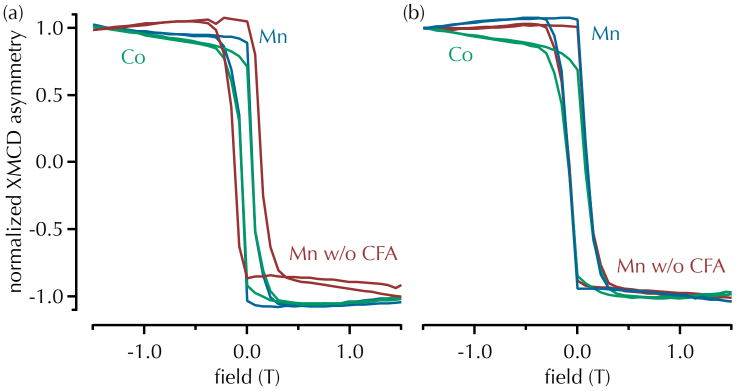

Figure 64: Mn-hystereses (blue) of $Mn_{1.5}Ga$ /$Co_2FeAl$ /MgO stacks on (a) $SrTiO_3$ and (b) MgO. Additionally, Co-hystereses (green) of both samples were added. For comparison a Mn major loop (red) for samples without an interlayer was added.

results with the magnetic moment obtained for samples without a $Co_2FeAl$ interlayer (cf. Figure 35), the determined values for samples with $Co_2FeAl$ are smaller. This would suggest a higher amount of Mn–O or a higher compensation of magnetic moments for samples with a $Co_2FeAl$ interlayer.

The element-specific hysteresis loops for samples on MgO and $SrTiO_3$ are illustrated in Figure 64. For both samples a Mn- and a Co-hysteresis were carried out to determine the magnetization direction of the interlayers. As seen before for the Co-Fe-B interlayer, the Co magnetic moments of the $Co_2FeAl$ aligns parallel to the Mn magnetic moments of the Mn-Ga. Therefore, the 1 nm thick $Co_2FeAl$ thin film reveals, an out-of-plane magnetization direction when deposited on a $Mn_{1.5}Ga$ thin film. Additionally, a Mn-hysteresis of a sample without interlayer was added (red curve, Figure 64) to investigate the effect of an interlayer on the magnetic properties of the $Mn_{1.5}Ga$ layer. $SrTiO_3$ based samples with an interlayer showed a lower coercive field, whereas for thin films on MgO, no difference is visible.

## *Transport measurements*

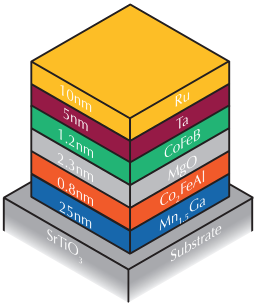

Figure 65: TMR stack with a $Mn_{1.5}Ga$ bottom electrode, a $Co_2FeAl$ interlayer and a Co-Fe-B counter electrode.

We prepared $Mn_{1.5}Ga$ (25 nm)/$Co_2FeAl$ (0.8 nm) /MgO (2.3 nm)/ CoFeB (1.2 nm) MTJ's on MgO and $SrTiO_3$ substrates (cf. Figure 65). The $Mn_{1.5}Ga$ bottom electrode was deposited at 550 °C the further layers were prepared at RT. The hole stack was ex-situ post-annealed at 360 °C to achieve a perpendicularly magnetized Co-Fe-B counter electrode. Figure 66 illustrates the major loops obtained at RT and 10 K. The TMR effects are not much higher

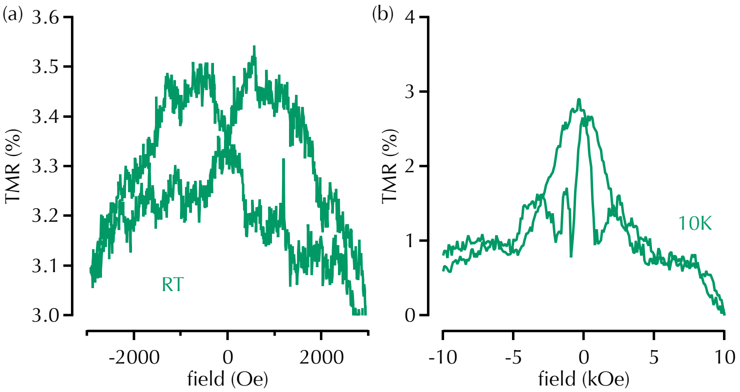

Figure 66: TMR effect of a $Mn_{1.5}Ga/Co_2FeAl/MgO$/Co-Fe-B tunnel junction on MgO at (a) RT and (b) 10 K.

compared to the ones obtained with a Co-Fe-B interlayer. At RT the soft electrode reveals an in-plane component, most likely induced by the superparamagnetic state of the Co-Fe-B. For LT a decrease of the coercive field of the soft electrode is observed. This behavior is different from that of the samples with Co-Fe-B interlayers and until now a reasonable explanation has not been found. The low nominal $Co_2FeAl$ thickness could also be an explanation for the the low TMR effect.

### *Auger electron spectroscopy*

AES measurements were carried out to examine the diffusion at the barrier interface. In Figure 67 the depth profile of the MTJ stack from Figure 65 is illustrated. Here, the signals from the Ru and Ta are clearly distinct and show no evidence of Ta–O. The signal from the other elements is rather low. The B diffusion in the top layer could not be detected, due to the overlapping Ta signal. To provide better insight into the distribution of the elements around the barrier interface, Figure 68 depicts a zoomed-in AES depth profile. Because of the high noise the Ru and Ta signal were canceled out to get a better view of the important materials next to the barrier. The Mg and $O_2$ peaks are broadened and differ from the sample in Figure 60. Evidence for the diffusion of Mn and Ga can be found in the fact that both signals start sooner than the Co and Fe signals. The Al signal was not detectable, due to the low thin film thickness and the depth resolution of the AE microscope.

Nonetheless, the diffusion of the Mn and Ga into the barrier

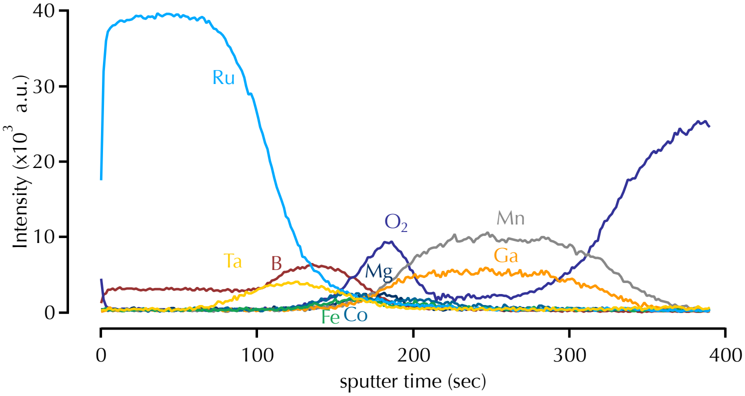

Figure 67: AES depth profile of a $Mn_{1.5}Ga$ (25 nm)/$Co_2FeAl$ (0.8 nm)/MgO (2.3 nm)/CoFeB (1.2 nm) tunnel junction on a $SrTiO_3$ substrate.

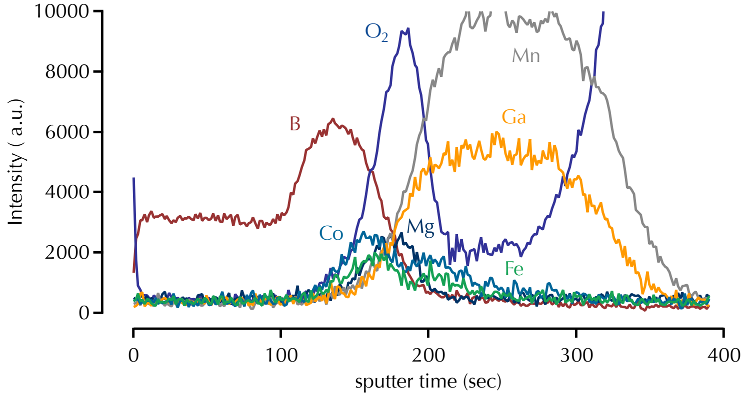

Figure 68: AES depth profile of a $Mn_{1.5}Ga$ (25 nm)/$Co_2FeAl$ (0.8 nm)/MgO (2.3 nm)/CoFeB (1.2 nm) tunnel junction on a $SrTiO_3$ substrate.

is again the main reason for the low TMR ratio. Therefore, the previously mentioned B diffusion of the bottom Co-Fe-B layer into the barrier is not the primary challenge. To overcome the second post-annealing process a new counter electrode has to be found. For example, $Co_{20}Fe_{60}B_{20}$ shows an out-of-plane magnetization direction without further post-annealing. Additionally, further investigations of the Mn and Ga diffusion have to be carried out, such as the dependence of the diffusion on the post-annealing temperature.

## *TiN seed layer*

The tetragonal distortion of the $Mn_{3\text{-}x}Ga$ thin films is based on the crystal growth, thus a substrate with a matching lattice constant and deposition on a heated substrate are required. We were able to show that substrates like MgO and $SrTiO_3$ exhibit a suitable lattice constant to achieve a $D0_{22}$- or $L1_0$-ordered $Mn_{3\text{-}x}Ga$ crystal phase. However, during the fabrication of MTJ's an ion etching process is required to prepare elements of several 100 $\mu m^2$. Unfortunately, the etching has to stop after the barrier, i.e., in the bottom electrode, otherwise the contact between electrode and power supply is not established. As a result a stray field from the large magnetic bottom layer could induce dipolar magnetostatic coupling with the top electrode. To overcome this obstacle a conducting seed layer with a suitable lattice constant is necessary. That way, the etching could proceed through the bottom electrode into the seed layer. Two commonly used seed layers are Pt and Cr, with an in-plane lattice constant of $a_{Pt} = 3.92$ Å and

$a_{Cr}$ = 2.88 Å. For a Cr buffer layer a growth rotated by 45 deg is needed to achieve a low lattice mismatch. A Pt buffer exhibits the lowest lattice mismatch (cf. Table 12) and reveals high thermal stability, whereas Pd and Cr diffuse at temperatures above 300 °C and 450 °C, respectively.[138] Diffusion of the seed layer into the electrode lowers the spin polarization at the barrier interface. However, on MgO and $SrTiO_3$ substrates the favored growth direction of Pt is the (111) direction. Only under circumstantial growth processes, like deposition under $O_2$ atmosphere or deposition on Cr, is the (001) direction obtained (not shown). TiN is a new material with high thermal stability, moderate lattice mismatch and low resistivity. The cubic NaCl structure exhibits a lattice constant of 4.24 Å. The lattice mismatch to the $Mn_{3-x}Ga$ compound is 7.78 % and thus quite high. However, a low resistivity of 10 µΩ cm to 15 µΩ cm (cf. Table 13) and a surface roughness of 0.8 nm were reported.[139] Even though the lattice mismatch is high the combination of high thermal stability, low resistivity and low surface roughness made TiN an excellent choice for application as a seed layer.

| buffer | mismatch |
|---|---|
| $SrTiO_3$ | 0.12 % |
| MgO | 7.13 % |
| Pt | 0.26 % |
| Pd | 0.51 % |
| $Cr^*$ | 3.93 % |
| TiN | 7.78 % |

Table 12: Mismatch between $Mn_{3-x}Ga$ and various substrates/buffer layer. * for a 45 deg rotated film growth.

| buffer | $\varrho$ (µΩ cm) |
|---|---|
| Pt | 10.6 |
| Pd | 10.7 |
| Cr | 12.7 |
| TiN | 10 to 15 |

Table 13: Resistivity $\varrho$ of various buffer layers.

## Crystallographic properties

In a first attempt, we deposited 40 nm thick TiN thin films on MgO due to the low lattice mismatches of 0.7 %. Additionally, TiN layers were prepared on $SrTiO_3$ because of the good growth conditions for $Mn_{3-x}Ga$ on $SrTiO_3$. The deposition temperature was varied from 210 °C to 830 °C. Figure 69 depicts the obtained XRD spectra of TiN on MgO and $SrTiO_3$ substrates. Because of the low lattice mismatch between MgO and TiN, the characteristic peaks of the TiN are only visible as shoulders close to the

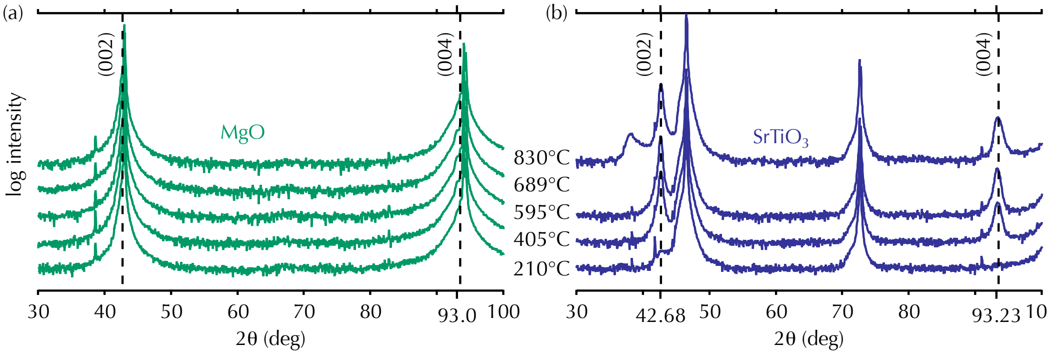

Figure 69: XRD scans of TiN thin films deposited at different temperatures on (a) MgO (green) and (b) $SrTiO_3$ (blue).

---

[138] Z. Kugler et al. In: *Journal of Magnetism and Magnetic Materials* 323.2 (2011); C. Sterwerf et al. In: *IEEE Transactions on Magnetics* 49.7 (2013)

[139] Y. Krockenberger et al. In: *Journal of Applied Physics* 112.8 (2012)

substrate reflexes. The TiN (004) reflex is found at 93 deg, thus the corresponding $c$-lattice constant is 4.26 Å and matches the literature values. Because of the higher lattice mismatch with $SrTiO_3$ the TiN reflexes are clearly visible in the XRD scans for all deposition temperatures, except 210 °C. The (002) reflex is visible at 42.68 deg and the (004) reflex at 93.23 deg. Thus the average out-of-plane lattice constant is determined to be 4.24 Å. Despite the higher lattice mismatch, the $c$ parameter corresponds well to the reported data.

## *Transport measurements*

The determination of the crystallographic properties of TiN thin films on MgO turned out to be difficult due to the low lattice mismatch. Another characteristic that provide insight into the crystalline quality is the resistivity of the films. A crystalline structure reveals a lower resistivity than an amorphous structure. Additionally, the formation of Ti–O also increase electrical resistance. Consequently, the obtained resistivity provides information about the crystalline structure and the formation of Ti–O.

Conventional four probe measurements were carried out on plain TiN thin films at 300 K. Four tips were placed on the thin film at the same distance. Then a current $I$ was driven through the outer tips and a voltage $U$ was measured at the inner contacts. The further determination was done by the van-der-Pauw[140] method. The resistivity of the thin film is defined as

$$\varrho = \frac{U}{I} \frac{\pi d}{\ln 2} \tag{46}$$

with $d$ being the film thickness. Figure 70 shows the obtained $\varrho$ of our TiN thin films depending on the deposition temperature. The lowest values are found for a deposition temperature of 595 °C. On MgO ($SrTiO_3$) substrate the TiN film reveals a resistivity of 39.91 μΩ cm (47.40 μΩ cm). These values are higher compared to the results from Krockenberger et al.[141] At 210 °C the high resistivity is due to the amorphous structure on $SrTiO_3$. The increasing resistivity with increasing deposition temperature, above 595 °C, is probably induced by the formation of Ti–O. It is possible that the O from the substrate diffuses into the TiN film and reacts with the Ti. For a closer look at this effect, AES depth profiles have to be carried out.

Additionally, the examination of the transition temperature $T_c$ into the superconducting regime provides information about

[140] L. J. van der Pauw. In: *Philips Research Reports* 13.1 (1958)

[141] Y. Krockenberger et al. In: *Journal of Applied Physics* 112.8 (2012)

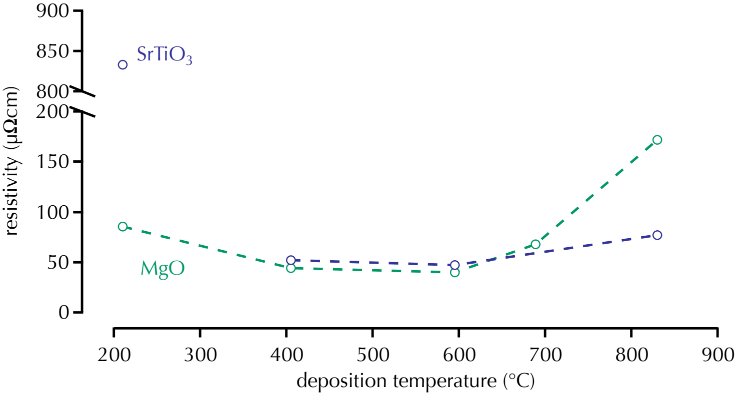

Figure 70: Resistivity of the TiN thin films depending on the deposition temperature. The samples were prepared on MgO (green) and SrTiO$_3$ (blue).

the crystalline order and formation of Ti–O. The phenomenon called superconductivity was discovered in 1911 by Kamerling Onnes[142] and describes the abrupt decay of the electric resistivity at low temperatures.[143] This effect can be explained by means of the BCS theory, named after the inventors Bardeen, Cooper and Schrieffer.[144] The underlying effect is the interaction of electrons with phonons and thus the condensation of what is called Cooper pairs. These Cooper pairs consist of two electrons with opposite impulse and spin. They do not underlie the Fermi-Dirac statistic but the Bose-Einstein statistic. Cooper pairs are bosons and are not subject to the Pauli exclusion principle. Additionally, they reveal no interaction with the atomic lattice. The BCS theory gives the following relation for the transition temperature:

$$T_c = 1.13 \frac{\hbar\omega_D}{k_B} \exp\left(-\frac{1}{D(E_F)V^*}\right) \tag{47}$$

with $\omega_D$ being the Debye frequency, $V^* = const.$ the electron phonon interaction and $D(E_F)$ the DOS at $E_F$. The Debye frequency is proportional to the atomic mass, $\omega_D \propto A^{-0.5}$. Due to the condensation of two electrons to one Cooper pair, a gap $\Delta$ occurs in the DOS of the superconductor. The BCS theory gives a relation between the gap $\Delta_0$ at 0 K and the transition temperature $T_c$

$$2\Delta_0(T = 0) = 3.5 k_B T_c \tag{48}$$

with $k_B$ being the Boltzmann constant. The coherence length is defined as the length scale where the condensation of a Cooper pair could take place. It strongly depends on the mean free path of the electrons. Defects in the lattice structure or impurities

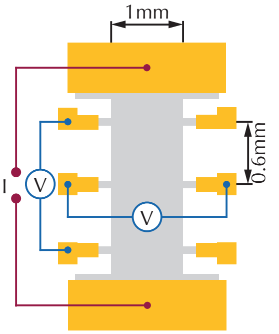

Figure 71: Schematic sketch of a Hall bar structure with Au contact pads and the measurement geometry.

[142] H. Kamerlingh Onnes. In: *Commun. Phys. Lab. Univ. Leiden* 12.120 (1911)

[143] However, it should be mentioned that the characteristic effect in superconductivity is the Meißner-Ochsenfeld effect.

[144] J. Bardeen et al. In: *Physical Review* 108.5 (1957)

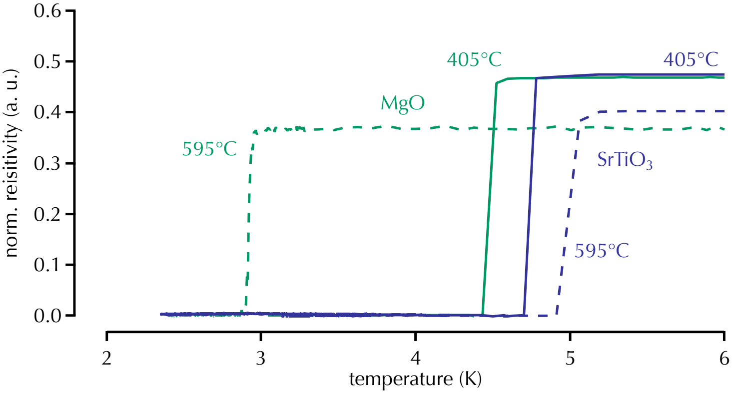

Figure 72: Transition into the superconducting state for TiN thin films deposited at 405 °C (bold line) and 595 °C (dashed line) on MgO (green) and SrTiO$_3$ (blue) substrates.

lower the mean free path. For that reason, a homogenous superconductor without impurities reveals a small $\Delta T_c$. In other words, the transition temperature shows a strong relation to the crystalline properties.

To determine the superconducting properties, we carried out transport measurements within a temperature range from 300 K to 2 K. Therefore, a closed-cycle helium cryostat was used and the TiN thin films were lithographed into a Hall bar structure (cf. Figure 71). The obtained resistivities, normalized to $\varrho$(300 K), as a function on the temperature are depicted in Figure 72. Samples on MgO exhibit a lower transition temperature $T_c$ compared to thin films on SrTiO$_3$. The samples deposited at 405 °C show a transition into the superconducting state at 4.52 K (MgO) and 4.78 K (SrTiO$_3$). For a deposition temperature of 595 °C a $T_c$ of 2.95 K (MgO) and 5.06 K (SrTiO$_3$) was determined. Only the samples prepared at 830 °C showed no superconducting state, even at 300 mK. This is more evidence of O diffusion from the substrate into the TiN layer. We conclude that the crystallographic properties with regard to the lattice constant and the superconducting properties are better for TiN on SrTiO$_3$.

## *Chemical properties*

The chemical properties of the TiN thin films were investigated by XAS in order to exclude the formation of Ti–O. Therefore, the TiN sample deposited at 405 °C on MgO was analyzed. The N-$K$-edge and the Ti-$L_{3,2}$-edges are illustrated in Figure 73. The top part of Figure 73 corresponds to the bulk-sensitive LM mode

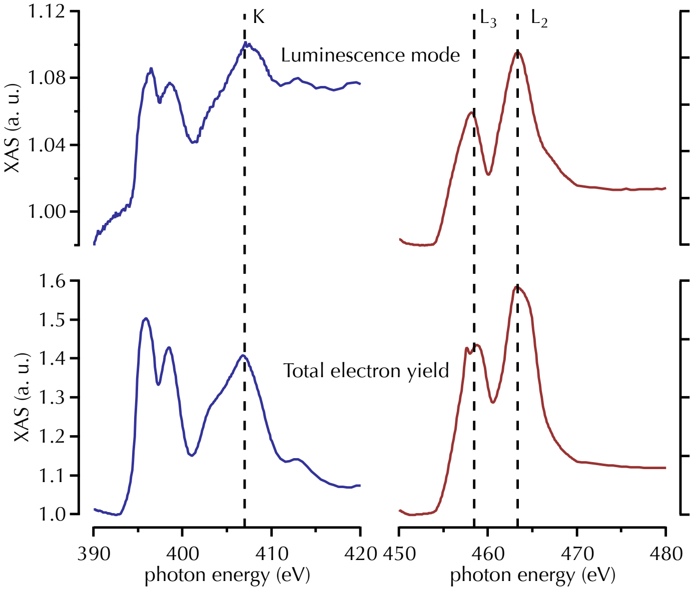

Figure 73: XA spectra of N-$K$-edge (blue) and Ti-$L_{3,2}$-edges (red) of a TiN thin film on MgO in LM (top) and TEY (bottom) mode. The TiN film was 40 nm thick and deposited at 405 °C. The sample was measured at BL 6.3.1.

and the bottom part to the surface-sensitive TEY mode. The N-spectra match the literature data well. If $O_2$ had replaced the N atoms at their positions in the crystal lattice, a spike in the XAS would have been observed, due to the free N atoms in the lattice.[145] The bulk-sensitive Ti-spectrum shows a metallic-like behavior, whereas the TEY signal shows a multiplet structure on the $L_3$-edge indicating a small amount of Ti–O. However, due to the fact that the TiN film was not covered by a capping layer, this small amount of Ti–O is acceptable and most likely induced by oxidation under atmosphere.

## *Seed layer for Mn-Ga*

In a next attempt, we sputtered 30 nm thick $Mn_{2.5}Ga$ thin films on a TiN buffer layer on MgO and $SrTiO_3$ substrates. The deposition temperature of the Mn-Ga was set to 550 °C. The TiN buffer layer was deposited at 405 °C and 830 °C. Each sample was capped by a 2.3 nm thick MgO layer to prevent the stack from oxidizing. Figure 74 presents the respective XRD scans. First we will take a closer look at samples with a TiN deposition temperature of 405 °C. The reflex intensity of the $Mn_{2.5}Ga$ layers on MgO is low, only the fundamental $D0_{22}$ peak at 51.08 deg is visible.

[145] L. Soriano et al. In: *Journal of electron spectroscopy and related phenomena* 62.1 (1993)

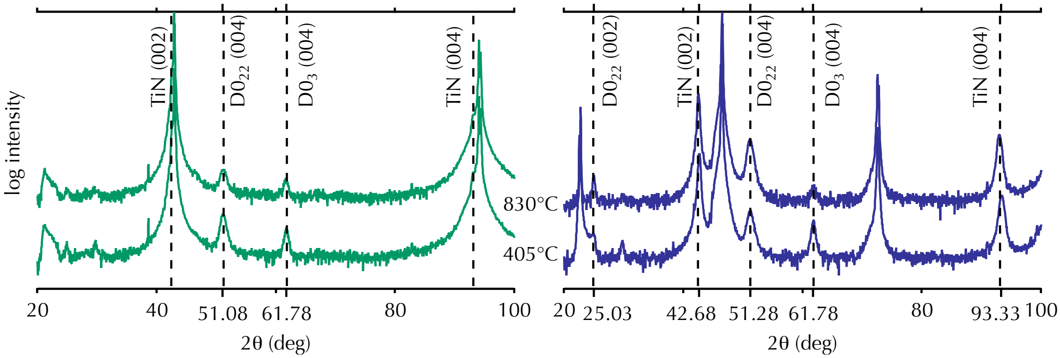

Figure 74: XRD scans of $Mn_{2.5}Ga$ thin films deposited on MgO (green) and $SrTiO_3$ (blue) substrates with TiN buffer layers. The TiN deposition temperature was set to 405 °C and 830 °C. The $Mn_{2.5}Ga$ was deposited at 550 °C.

Therefore, the $c$ lattice constant is determined to be 7.15 Å. In addition, the fundamental $D0_3$ reflex is present at 61.78 deg. The corresponding $c$ parameter is 6.01 Å. Thus, two different phases were obtained. However, the analogous sample on $SrTiO_3$ shows a higher peak intensity. The super lattice (002) and fundamental (004) reflex of the $D0_{22}$ phase are present at 25.03 deg and 51.28 deg. Thus, the $c$ lattice constant is 7.12 Å. In addition, the fundamental $D0_3$ reflex is found at 61.78 deg. The associated $c$ parameter is 6.01 Å. Samples where the TiN was deposited at 830 °C exhibit quite a different behavior. The TiN buffered $Mn_{2.5}Ga$ thin film on MgO shows a lower reflex intensity compared to the sample with a TiN deposition temperature of 405 °C, the $Mn_{2.5}Ga$ thickness being the same. The determined out-of-plane lattice parameters are $c_{D0_{22}} = 7.15$ Å and $c_{D0_3} = 6.01$ Å. The similar sample on $SrTiO_3$ reveals the $D0_{22}$ super lattice and fundamental reflexes and the $D0_3$ fundamental peak. The corresponding out-of-plane lattice parameters are $c_{D0_{22}} = 7.12$ Å and $c_{D0_3} = 6.01$ Å. The intensity of the $D0_3$ reflex is essentially lower compared to the former sample on $SrTiO_3$. The peak positions are at the same angles as for the sample with a TiN deposition temperature of 405 °C on $SrTiO_3$. To sum up, we achieved a tetragonal distortion of the $Mn_{2.5}Ga$ crystal when deposited on a TiN seed layer. However, due to the large lattice mismatch between the $Mn_{3\text{-}x}Ga$ crystal and the TiN buffer we only obtained a multiphase structure, a combination of the $D0_{22}$ and $D0_3$ phases. For thin films on $SrTiO_3$ substrates the $D0_3$-ordered phase could be decreased by increasing the deposition temperature.

THE MAGNETIC PROPERTIES of the $Mn_{2.5}Ga$ thin films with TiN buffer

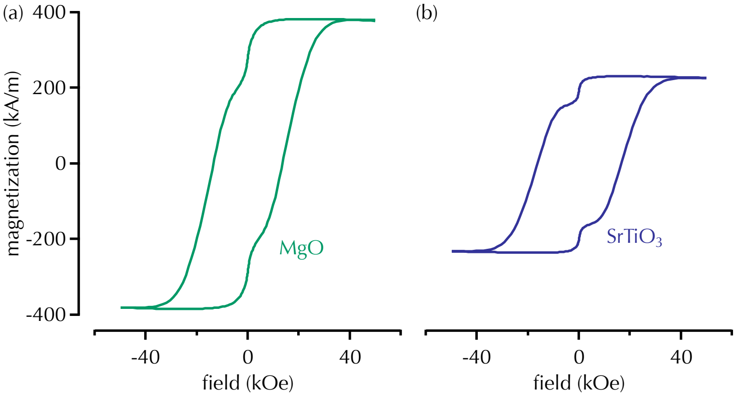

Figure 75: Hysteresis loops for TiN buffered $Mn_{2.5}Ga$ thin films on MgO (green) and $SrTiO_3$ (blue) substrates.

were investigated by means of SQUID measurements.[146] Only the samples with a TiN deposition temperature of 830 °C were investigated due to the higher crystalline order. In Figure 75 the hysteresis loops for an out-of-plane configuration are shown. Both hysteresis loops show the previously mentioned step in the major loop (cf. Figure 27). A relation between the step height and the amount of the $D0_3$ phase could not be determined. The coercivity of TiN buffered Mn-Ga films on MgO ($SrTiO_3$) is 1.30(5) T (1.60(5) T) and the squareness ratio is 0.75(5) (0.86(5)). In addition, the magnetization values differ for samples on MgO and $SrTiO_3$ substrate. We determined a value of $M_S = 232\,\mathrm{kA\,m^{-1}}$ on $SrTiO_3$ and a value of $M_S = 383\,\mathrm{kA\,m^{-1}}$ on MgO substrate. The magnetization for samples on MgO is 1.65 times higher than on $SrTiO_3$ substrates. This discrepancy is based on the two crystal phases. The sample on $SrTiO_3$ showed a more distinct $D0_{22}$ phase and therefore a higher compensation of the magnetic moments, i.e., lower net magnetization. A question that remains open is how the sum of the magnetization of the $D0_{22}$ phase and the $D0_3$ phase is assembled.

## *Conclusion*

We successfully prepared out-of-plane magnetized $Mn_{3\text{-}x}Ga$ ($1.5 \leq x \leq 0.1$) thin films with $L1_0$ or $D0_{22}$ crystal structure. The thin films were magnetron sputtered on MgO and $SrTiO_3$ substrates at deposition temperatures between 520 °C and 595 °C. The surface roughness was analyzed by XRR. Thin films on MgO and $SrTiO_3$ showed the lowest roughness (below 1 nm) when prepared by

[146] Measured at the Max-Planck-Institute for Chemical Physics of Solids in Dresden

deposition from a $Mn_{45}Ga_{55}$, a $Mn_{50}Ga_{50}$ or a $Mn_{60}Ga_{40}$ composite target. To determine the crystal phase we carried out XRD measurements. A decreasing out-of-pane lattice constant with decreasing Mn content was found for both crystal phases. The highest crystalline order was found for samples deposited from a Mn-Ga composite target. Thin films deposited on $SrTiO_3$ substrates revealed higher crystallinity, i.e., lower FWHM and higher textured order, compared to samples on MgO. This behavior is based on the lower lattice mismatch between $SrTiO_3$ and $Mn_{3\text{-}x}Ga$. The magnetic properties were investigated by means of SQUID measurements. $Mn_{3\text{-}x}Ga$ thin films with an $L1_0$ crystal phase showed a considerably higher magnetization than $D0_{22}$-ordered thin films. The lower magnetization derives from higher degree of compensation of the magnetic moments in the $D0_{22}$ phase. In addition, the coercive field was lower for $L1_0$-$Mn_{3\text{-}x}Ga$ thin films. These samples could be saturated in an in-plane configuration with a field of around 4 T. By applying the Stoner-Wohlfarth model an anisotropy energy $K$ of $0.97(2) \times 10^6\,\mathrm{J\,m^{-3}}$ was determined. The formation of Mn–O at the $Mn_{3\text{-}x}Ga$/MgO interface is a crucial point in the preparation of MTJ's. For this reason, we investigated the chemical and magnetic properties at the barrier interface by XAS and XMCD. Different $L1_0$- and $D0_{22}$-ordered $Mn_{3\text{-}x}Ga$ thin films on $SrTiO_3$ substrates were examined by surface-sensitive total electron yield. The XAS showed the formation of Mn–O at the barrier interface for each sample. However, samples prepared by co-deposition from a Mn-Ga composite target and an additional Mn target revealed the highest amount of Mn–O. The XMCD signal is more sensitive to the formation of Mn–O. It showed the highest XMCD signal, i.e., the lowest amount of Mn–O for samples deposited from a $Mn_{50}Ga_{50}$ target. By applying the sum rules on the obtained XA and XMCD spectra the magnetic moment could be determined. We found the expected decrease of the magnetic moment with increasing Mn content.

In addition, we examined the consequences of the insertion of a ferromagnetic layer, Co-Fe-B and $Co_2FeAl$, between the $L1_0$-ordered $Mn_{3\text{-}x}Ga$ layer and the MgO barrier.[147] Whereas the surface roughness and crystalline order stayed unaffected the formation of Mn–O could be further suppressed. Additionally, by changing the deposition method of the MgO barrier from magnetron sputtering to e-beam evaporation the amount of Mn–O was further decreased. The magnetic orientation of the ferromagnetic insertion layer is of particular interest. By carrying

[147] M. Glas et al. In: *Journal of Applied Physics* 114.18 (2013)

out element-specific hysteresis loops, we were able to determine a parallel alignment to the $Mn_{3\text{-}x}Ga$ magnetic moments, even for a Co-Fe-B thickness of 2 nm. Thus the $Mn_{3\text{-}x}Ga$ layer acts as a pinning layer on the soft-magnetic insertion layer. After the characterization of the $Mn_{3\text{-}x}Ga$ layer had been completed, we prepared MTJ's with an $L1_0$-ordered bottom electrode, 1 nm Co-Fe-B insertion layers, and a $\{Co/Pt\}_{10}$ counter electrode. The obtained transport measurements pointed out an in-plane component of the hard electrode, i.e., the $\{Co/Pt\}_{10}$ multilayers. To overcome this obstacle we replaced the multilayer electrode by a 1.2 nm thick Co-Fe-B film. That way, further post-annealing was required to obtain a perpendicularly magnetized Co-Fe-B thin film, but post-annealing also increases the crystallinity of the MgO barrier. The achieved TMR effect of this stack structure was marginally higher compared to the previous system. The reasons for the low TMR effect are the following: At RT the top Co-Fe-B electrode shows a superparamagnetic state, by cooling down the sample below the blocking temperature a ferromagnetic state was achieved. Another obstacle was the temperature dependence of the coercive fields. Due to a crossover of the coercive fields during cooling, the hard electrode becomes the soft electrode and vice versa. In the crossover regime the TMR effect almost disappears. However, even at a temperature above the coercive field crossover and below the superparamagnetic state the TMR effect showed a maximum value of only 10 %. The cause of this low TMR effect was detected by AES. The B of the bottom Co-Fe-B layer and the Mn and Ga of the $Mn_{3\text{-}x}Ga$ electrode diffuse to the barrier interface. For this reason, a material combination with low spin polarization is next to the barrier and reduces the TMR effect. Hence, we changed the ferromagnetic insertion layer. An 0.8 nm thick $Co_2FeAl$ layer overcomes the obstacle of B diffusion. But again the obtained TMR ratio was only 3 % at 10 K. Here again, a diffusion of the Mn and Ga was observed via AES.

Another issue that should be mentioned is the stray field of the Mn-Ga electrode. Kanai et al.[148] reported that the stray field from a 1 nm Co-Fe-B electrode affects the 1.2 nm thick Co-Fe-B counter electrode that is separated by a 1 nm thick MgO layer. Therefore, it is plausible that a 25 nm thick hard-magnetic $Mn_{3\text{-}x}Ga$ bottom electrode also induces a stray field that affects the soft-magnetic counter electrode. The bottom electrode serves as a supply line for the applied voltage. For this reason, the etching process during the preparation of the MTJ's stops after the MgO barrier. That way, the area of the bottom electrode is much larger compared

[148] S. Kanai et al. In: *Applied Physics Letters* 104.21 (2014)

to that of the counter electrode. To make etching through the bottom electrode possible, a conducting seed layer is required. Typical buffer layers are Cr and Pt due to the matching in-plane lattice constant. Nonetheless, the diffusion temperature of the Cr is too low, and to achieve a (001) oriented Pt layer circumstantial growth conditions are necessary. Therefore, we investigated TiN.[149] Even though the lattice mismatch is around 7.78 % the high thermal stability, low resistivity, and low surface roughness make TiN a promising candidate to serve as a seed layer in MTJ's. However, first the structural and electrical properties as well as the surface roughness had to be determined. For this reason, we prepared TiN thin films on MgO and $SrTiO_3$ substrates at various deposition temperatures. Afterwards, the surface roughness was determined via XRR. The obtained roughness values were below 1 nm. XRD measurements were performed to determine the crystalline properties. Transport measurements showed a superconducting state below 5 K depending on the deposition temperature and type of substrate. A room temperature resistivity of 39.91 $\mu\Omega$ cm on MgO was verified via four-point terminal transport measurements. The formation of Ti–O could be excluded for a deposition temperature of 405 °C by XAS. Afterwards, we prepared TiN buffered $Mn_{2.5}Ga$ thin films on MgO and $SrTiO_3$. XRD measurements revealed a multiphase, a combination of the $D0_{22}$ and the $D0_3$ crystal structures. For this reason, samples on MgO showed higher magnetization compared to samples on $SrTiO_3$ due to the two crystal structures.

---

[149] A. Niesen et al. In: *arXiv.org* (2015). eprint: `1510.06256v2`

# *The ternary Mn-Co-Ga compound*

*In this chapter we attend to the preparation of* $Mn_{3\text{-}x}Co_xGa$ *(*$0.7 \leq x \leq 0.3$*) thin films. We investigated the crystallographic structure and magnetic properties of thin films with a cubic and a tetragonally distorted crystal phase. The barrier interface was analyzed with regard to film roughness and the formation of Mn–O in view of the intended integration into MTJ's.*

## *Stoichiometry dependence*

In the previous chapter the tetragonally distorted $L1_0$ and $D0_{22}$ phases of the $Mn_{3\text{-}x}Ga$ compound were investigated. Unfortunately, the fully compensated, half-metallic properties of the $D0_3$-$Mn_3Ga$ phase diminish during tetragonal distortion into the $D0_{22}$-phase. Thus a theoretically predicted spin polarization of 88 % and a magnetic moment of $1\,\mu_B$ was reported.[150] Substitution of Mn atoms by Co will decrease the magnetic moment due to a higher compensation. Alijani et al.[151] reported a lower magnetic moment for $Mn_{2.7}Co_{0.3}Ga$ than for $Mn_3Ga$. Additionally, they determined a Curie temperature between 730 °C and 790 °C, depending on the Co content. The magnetization direction is changed from in-plane to out-of-plane by increasing the Mn content and decreasing the Co content.[152] The soft-magnetic $Mn_{3\text{-}x}Co_xGa$ layer with an in-plane magnetization direction occurs for $x > 0.5$ (cubic structure). For $0.5 < x \leq 1$ the hard-magnetic $D0_{22}$ structure with a magnetization direction perpendicular to the film plane is obtained. For this reason, the crystal properties depend on the Mn to Co concentration. The cell volume of the cubic phase decreases with increasing Co content due to the lower atomic radius compared to Mn. The tetragonal phase reveals an almost constant cell volume because with decreasing Co content the $c$ lattice constant increases and the $a$ lattice constant decreases. The in-plane lattice constant ranges from 5.869 Å

[150] B. Balke et al. In: *Applied Physics Letters* 90.15 (2007); J. Winterlik et al. In: *Physical Review B* 77.5 (2008)

[151] V. Alijani et al. In: *Applied Physics Letters* 99.22 (2011)

[152] V. Alijani et al. In: *Applied Physics Letters* 99.22 (2011)

for cubic crystals to 3.871 Å for tetragonal structures. The out-of-plane lattice constant of the tetragonal phase is around 7.04 Å. Like the crystal structure the magnetic properties depend on the stoichiometry. Starting with a total magnetic moment of 2 $\mu_B$ for $Mn_2CoGa$ the moment decreases to 0.49 $\mu_B$ for $Mn_{2.6}Co_{0.4}Ga$.[153] Hence, a higher compensation of the magnetic moments is found for Mn rich structures. TMR effects of 5 % were first reported by Kubota et al.[154] for Mn-Co-Ga based MTJ's. The reported stack structure was MgO/ Cr (40 nm)/ $Mn_{2.3}Co_{0.4}Ga_{1.3}$ (30 nm)/ Mg (0.4 nm)/ MgO (2.2 nm)/ $Co_{20}Fe_{60}B_{20}$ (1.3 nm)/ Ta (5 nm)/ Ru (7 nm).

$Mn_{3\text{-}x}Co_xGa$ reveals properties similar to $Mn_{3\text{-}x}Ga$, whereas the Curie temperature is higher and the magnetic moment is lower. Therefore, the tetragonally distorted $D0_{22}$ phase is an auspicious candidate for serving as an electrode in MTJ's.

In a first attempt we prepared $Mn_{3\text{-}x}Co_xGa$ thin films with two different compositions. For this purpose we co-sputtered our thin films from a $Mn_{45}Ga_{55}$ or a $Mn_{60}Ga_{40}$ composite target together with a Mn and a Co target.[155] By changing the power applied to each target the stoichiometry was varied. Since the in-plane lattice constant is similar to $Mn_{3\text{-}x}Ga$, we used MgO (001) and $SrTiO_3$ (001) substrates. The deposition temperature was between 500 °C and 550 °C. Afterwards the samples were cooled down to room temperature and capped by a 2.3 nm thick MgO layer. In that way, the stack was prevented from oxidizing and the influence of the barrier on the bottom electrode could be investigated. The stoichiometry of our thin films was determined via XRF measurements. XRR and XRD investigations were performed to analyze the surface roughness and crystallographic phase. The magnetic properties were examined by means of VSM, element-specific hysteresis loops obtained at BL 6.3.1, and SQUID measurements. Finally, the Mn-Co-Ga/MgO interface was investigated by XAS and XMCD.

## *X-ray fluorescence measurements*

Different compositions were obtained by adjusting the applied power at the respective targets. XRF measurements in a He atmosphere were carried out to determine the stoichiometry. In Table 14 the investigated thin films are listed. By using the $Mn_{60}Ga_{40}$ target it was possible to lower the power applied to the Mn and Co target by a factor of two.

---

[153] Magnetic moment at 5 K

[154] T. Kubota et al. In: *Journal of Applied Physics* 115.17 (2014)

[155] In what follows, we will only refer to the Mn-Ga target used.

| Mn-Ga | Mn | Co | composition | substrate |
|---|---|---|---|---|
| 100 W | 20 W | 10 W | $Mn_{2.3}Co_{0.7}Ga$ | $SrTiO_3$ |
| 100 W | 45 W | 20 W | $Mn_{2.7}Co_{0.3}Ga$ | $SrTiO_3$ |
| 100 W | 20 W | 10 W | $Mn_{2.6}Co_{0.3}Ga$ | $SrTiO_3$ |

Table 14: Overview of the prepared samples and their stoichiometry. The top four samples were sputtered from a $Mn_{45}Ga_{55}$ target and an additional Mn and Co target. The bottom sample was prepared from a $Mn_{60}Ga_{40}$ target and an additional Mn and Co target. The stoichiometry was determined by XRF measurements.

## *X-ray reflectivity investigations*

In Figure 76 the XRR scans of $Mn_{2.3}Co_{0.7}Ga$ on MgO and $SrTiO_3$ as well as $Mn_{2.7}Co_{0.3}Ga$ on MgO and $SrTiO_3$ are illustrated. The absence of Kiessing fringes in the XRR scan of the $Mn_{2.3}Co_{0.7}Ga$ samples reveal a high surface roughness. It is not possible to fit the obtained scans and determine the film thickness, surface roughness and density. The $Mn_{2.7}Co_{0.3}Ga$ thin films on MgO and $SrTiO_3$ show two to three distinct oscillations. By fitting the scans via Parratt algorithm we obtained a film thickness of around 16(1) nm on $SrTiO_3$ and 20(1) nm on MgO. In addition, a film roughness of 1.4(5) nm on $SrTiO_3$ and 5.7(5) nm on MgO was determined.[156] The high surface roughness corresponds well to the results obtained for co-deposited $Mn_{3-x}Ga$. Therefore, additional evidence was found for a co-deposition induced surface roughness. Consequently, the integration of these thin films into MTJ's is difficult. The high roughness of the bottom electrode results in metallic pinholes through the barrier and thus a tunnel effect is not possible. However, to lower the surface roughness we have to minimize the power of the Mn and Co target during the co-deposition process. For that reason, we used a $Mn_{60}Ga_{40}$ target to

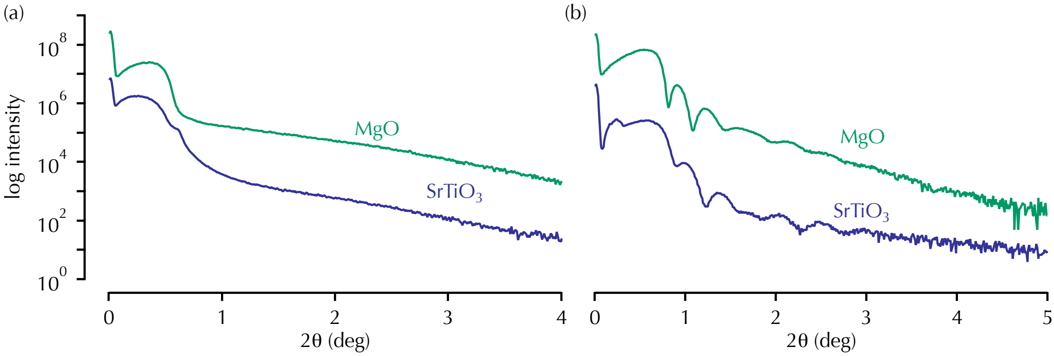

Figure 76: XRR scans of the (a) $Mn_{2.3}Co_{0.7}Ga$ and (b) $Mn_{2.7}Co_{0.3}Ga$ on MgO (green) and $SrTiO_3$ (blue) substrates.

[156] High errors due to the low number of oscillations.

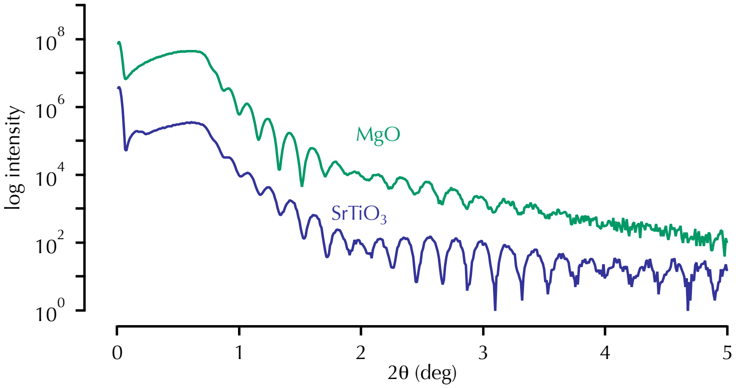

Figure 77: XRR scans of $Mn_{2.6}Co_{0.3}Ga$ thin films deposited at 500 ℃ on MgO (green) and $SrTiO_3$ (blue). Here a $Mn_{60}Ga_{40}$ target was used.

achieve a higher Mn concentration and therefore a lower power applied to the Mn target is required. Figure 77 illustrates the XRR scans of $Mn_{2.6}Co_{0.3}Ga$ thin films deposited on MgO and $SrTiO_3$ at 500 ℃. The obtained film thickness on $SrTiO_3$ was 38.50(5) nm and the roughness 0.6(1) nm. To gain insight into the effect of the deposition temperature on the film properties, we prepared $Mn_{2.6}Co_{0.3}Ga$ thin films at higher temperatures on $SrTiO_3$. The values obtained from the XRR fit are illustrated in Figure 78. The film thickness increases with increasing deposition temperature, whereas the density decreases. However, the roughness shows a minimum value at 500 ℃. Therefore, the $Mn_{2.6}Co_{0.3}Ga$ thin film deposited at 500 ℃ is a promising candidate for use as bottom electrode in MTJ's.

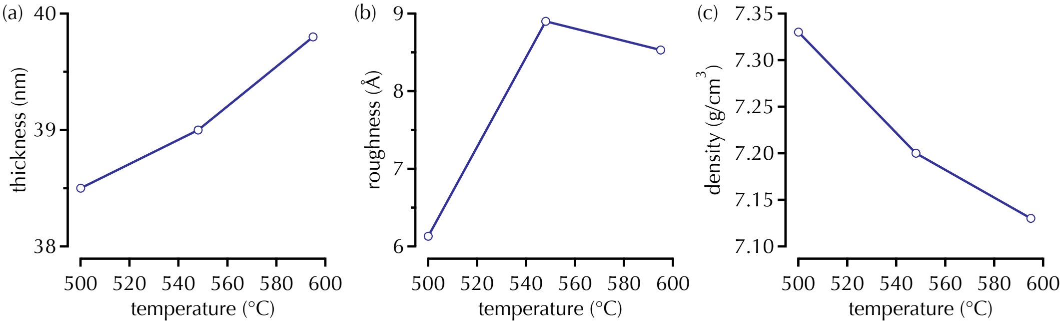

Figure 78: Temperature dependence of the (a) film thickness, (b) roughness and (c) the density of $Mn_{2.6}Co_{0.3}Ga$ thin films on $SrTiO_3$. The samples were prepared from a $Mn_{60}Ga_{40}$ target and additional Mn and Co targets.

## Crystallographic properties

Figure 79 illustrates the XRD scans of a $Mn_{2.3}Co_{0.7}Ga$ thin film deposited on MgO and $SrTiO_3$ substrates. The deposition temperature was chosen to be 500 °C. A cubic structure is obtained for both types of substrate. The super lattice and fundamental peaks of the cubic phase are visible at 30.33 deg and 63.18 deg independently of the substrate. The corresponding lattice constant was determined to $c = 5.88$ Å and matches well with the data reported by Alijani et al.[157] However, two further reflexes are found at 32.93 deg and 69.08 deg for thin films on MgO. Thin films deposited on $SrTiO_3$ exhibit only the reflex at 32.93 deg but with lower intensity. These reflexes are not assigned to the cubic or tetragonal phase.

Apart from the cubic phase we investigated the tetragonally distorted $D0_{22}$ phase. In Figure 80 the XRD scans of $Mn_{2.7}Co_{0.3}Ga$ thin films on MgO and $SrTiO_3$ are depicted. The deposition temperature was 550 °C. The thin film on MgO shows only reflexes of the $D0_{22}$ crystal structure. The fundamental reflex is found at 52.31 deg and at 25.61 deg the super lattice reflex appears. Therefore, the average $c$ parameter is 6.98 Å. For the sample on $SrTiO_3$, the (002) and (004) reflex can be found at 25.14 deg and 51.85 deg resulting in $c = 7.07$ Å. This value fits with the reported bulk data of Alijani et al.[158] The thin film on MgO reveals a lower $c$ lattice constant compared to layers on $SrTiO_3$ substrate. This behavior was expected due to the higher lattice mismatch between the substrate and the thin film.

Besides the discussed $Mn_{2.7}Co_{0.3}Ga$ sample sputtered from a

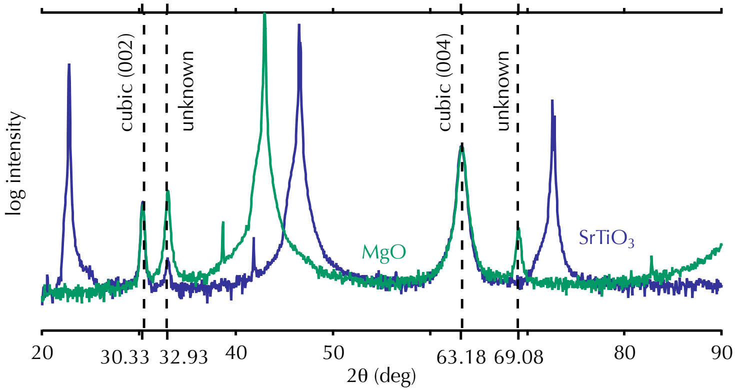

Figure 79: XRD scans of a $Mn_{2.3}Co_{0.7}Ga$ thin films deposited on MgO (green) and $SrTiO_3$ (blue).

[157] V. Alijani et al. In: *Applied Physics Letters* 99.22 (2011)

[158] V. Alijani et al. In: *Applied Physics Letters* 99.22 (2011)

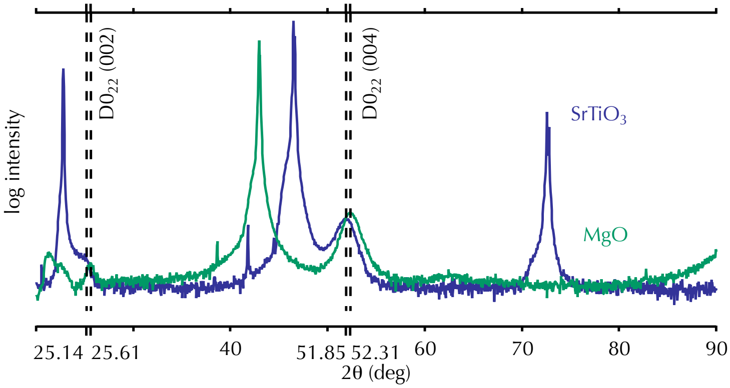

Figure 80: XRD scans of $Mn_{2.7}Co_{0.3}Ga$ thin films deposited on MgO (green) and $SrTiO_3$ (blue).

$Mn_{45}Ga_{55}$ target, we also prepared an almost analogous sample from a $Mn_{60}Ga_{40}$ target.[159] Thus the power applied to the Mn and Co target could be decreased and a lower surface roughness was obtained. The XRD scans of the respective samples reveal the influence of the different preparation conditions, i.e., lower power applied to the targets on the crystallographic structure (cf. Figure 81). The deposition temperature of the $Mn_{2.6}Co_{0.3}Ga$ thin film was chosen to be 500 °C in order to obtain a low surface roughness. Both samples show the (002) and (004) reflex of the *D*0$_{22}$ phase. The Mn-Co-Ga crystal on MgO substrate reveals a very small (004) reflex at 63.10 deg, probably induced by the cubic phase. The peak positions for samples on MgO are 26.18 deg and

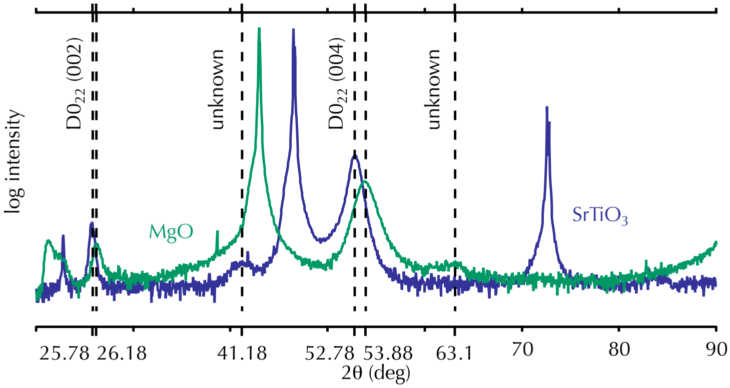

Figure 81: XRD scans of 38.50(5) nm thick $Mn_{2.6}Co_{0.3}Ga$ thin films on MgO (green) and $SrTiO_3$ (blue) substrates. The samples were prepared from a $Mn_{60}Ga_{40}$, a Mn, and a Co target.

[159] And additional Mn and Co targets.

53.88 deg and on $SrTiO_3$ 25.78 deg and 52.78 deg). The respective angles for samples on MgO are higher, which indicates a lower lattice constant. The corresponding out-of-plane lattice constants of the $Mn_{2.6}Co_{0.3}Ga$ thin films are 6.81 Å on MgO and 6.95 Å on $SrTiO_3$. These values match well with the data from Alijani et al.[160] and the $c$ value on MgO substrate is lower than the $c$ value on $SrTiO_3$ substrates.

As mentioned previously, the deposition temperature dependence of the $Mn_{2.6}Co_{0.3}Ga$ compound was also investigated. Therefore, three different deposition temperatures, 500 °C, 550 °C and 595 °C, were used. Figure 82 reveals the out-of-plane lattice constant $c$, the FWHM of the $D0_{22}$ (004) and (002) reflex and the textured order as a function of the deposition temperature. The reported bulk values of the $c$ constant from Alijani et al.[161] are not achieved, most likely due to the expansion in the $a$,$b$-plane induced by the $SrTiO_3$ and the MgO substrate. The lowest FWHM and highest textured order are present at a deposition temperature of 550 °C, for thin films on both substrates. However, compared to the textured order value of 830 for the $L1_0$-$Mn_{1.6}Ga$ thin film on $SrTiO_3$, the values of $Mn_{2.6}Co_{0.3}Ga$ are quite low. This is evidence of incompletely crystallized thin films. The $D0_{22}$-ordered $Mn_{3\text{-}x}Ga$ thin films reveal comparable textured order values. Thus, the crystal quality of $D0_{22}$-Mn-Co-Ga and $D0_{22}$-$Mn_{3\text{-}x}Ga$ thin films is similar.

Apart from the $D0_{22}$ structure thin films on MgO exhibit an additional cubic phase ($B2$, $L2_1$, or $Hg_2CuTi$ type).[162] The temperature dependence of the $c$ parameter, the FWHM of the (004) and the textured order are shown in Figure 83. The fundamental (002) reflex of the $D0_3$ phase is only visible for a deposition

[160] V. Alijani et al. In: *Applied Physics Letters* 99.22 (2011)

[161] V. Alijani et al. In: *Applied Physics Letters* 99.22 (2011)

[162] G. D. Liu et al. In: *Physical Review B* 77.1 (2008)

[163] V. Alijani et al. In: *Applied Physics Letters* 99.22 (2011)

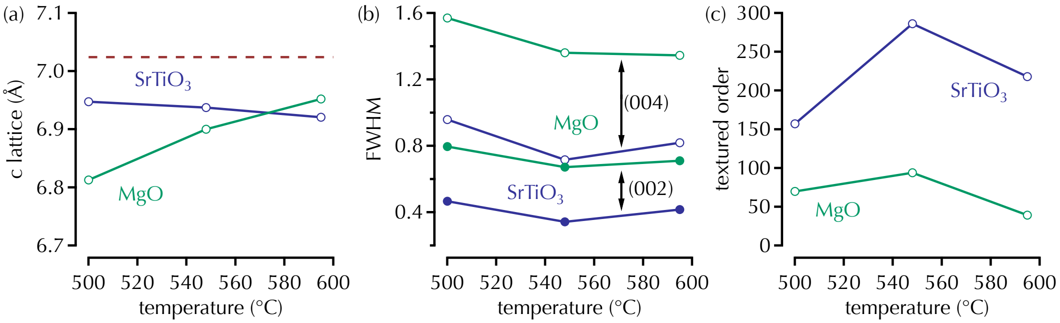

Figure 82: Temperature dependence of the (a) $c$ lattice constant, (b) FHWM of the (002) (bold) and (004) (circle) reflex and (c) the textured order of $Mn_{2.6}Co_{0.3}Ga$ thin films on MgO (green) and $SrTiO_3$ (blue). The red dashed line indicates the values reported by Alijani et al.[163]

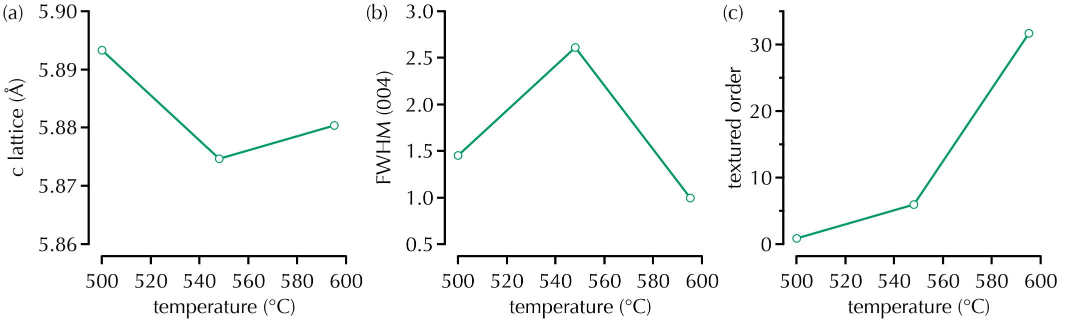

Figure 83: Temperature dependence of the cubic (a) $c$ lattice constant, (b) FHWM of the (004) reflex and (c) the textured order of $Mn_{2.6}Co_{0.3}Ga$ thin film on MgO.

temperature of 595 °C. The lattice constant $c$ shows a maximum at 500 °C, the data from Alijani et al.[164] are in the same range. The lowest FWHM and the highest textured order are found for a deposition temperature of 595 °C. Therefore a correlation between the deposition temperature and the cubic and tetragonal phases exists. If the deposition temperature is chosen too high, a multiphase is observed. This behavior is inconsistent with the results for $Mn_{3\text{-}x}Ga$, here the cubic phase is obtained if the deposition temperature is too low.[165] Compared to the $D0_{22}$-phase the textured order values are much lower (a tenth of the $D0_{22}$ values) and so is the crystalline quality.

To compare the crystallinity of the Mn-Co-Ga thin films with the $Mn_{3\text{-}x}Ga$ thin films, we will take a closer look on the FWHM of the present reflexes. Because of the higher crystallinity of thin film on $SrTiO_3$ we will neglect samples on MgO. The obtained data are present in Table 15. The cubic structure shows the lowest values for the Mn-Co-Ga samples and thus the largest grain size. The values of the $Mn_{2.7}Co_{0.3}Ga$ thin film deposited from the $Mn_{45}Ga_{55}$ target are twice as high for the (002) reflex and three times higher for the (004) reflex. The almost same sample

| sample | FWHM (002) | FWHM (004) | FWHM (006) |
|---|---|---|---|
| $Mn_{2.3}Co_{0.7}Ga$ | 0.282 | 0.558 | % |
| $Mn_{2.7}Co_{0.3}Ga$ | 0.565 | 1.614 | % |
| $Mn_{2.6}Co_{0.3}Ga^*$ | 0.466 | 0.958 | 0.270 |
| $Mn_{2.5}Ga$ | 0.307 | 0.509 | 0.611 |

Table 15: The obtained FWHM of the respective (002), (004) and (006) reflex for different $Mn_{3\text{-}x}Co_xGa$ thin films and a $Mn_{2.5}Ga$ thin film on $SrTiO_3$. The sample $Mn_{2.6}Co_{0.3}Ga^*$ was prepared from a $Mn_{60}Ga_{40}$ target and deposited at 500 °C.

[164] V. Alijani et al. In: *Applied Physics Letters* 99.22 (2011)

[165] M. Glas. Diploma thesis. Bielefeld University, Faculty of Physics, 2012

($Mn_{2.7}Co_{0.3}Ga$) prepared from a $Mn_{60}Ga_{40}$ target exhibits also higher values compared to those of the cubic phase. However, this sample was the only sample that reveals the (006) reflex. Nonetheless, the received data show a lower crystallinity of the tetragonal Mn-Co-Ga thin films compared to the $Mn_{2.5}Ga$ thin film on $SrTiO_3$. It has to be mentioned that this sample was also prepared from the $Mn_{60}Ga_{40}$ target. To summarize, co-deposition from different targets decrease the crystallinity of the thin film and increases its surface roughness.

## *Investigations of the magnetic properties*

The magnetic properties were investigated by means of a vibrating sample magnetometer (VSM)[166] (±2 T), element-specific hysteresis loops obtained at BL 6.3.1 (±2 T), and SQUID (±7 T) measurements, of which only the latter provides information about magnetization. The external magnetic field was applied perpendicular and parallel to the film plane, except for the element-specific hysteresis loops.

For the VSM measurement, the sample was placed in a homogeneous magnetic field. With the help of piezoelectric material, a sinusoidal vibration of the sample is caused. The periodic vibration of the sample results in variation of the magnetic flux (Faraday's law of induction). The change of the magnetic flux induces a voltage in what is called pickup coils[167]. The induced voltage is proportional to the magnetic moment and is independent of the static, external magnetic field.

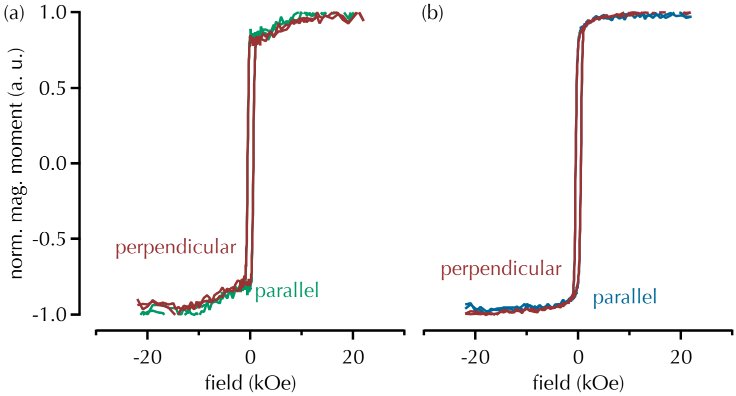

Figure 84: VSM hysteresis loops for $Mn_{2.3}Co_{0.7}Ga$ thin films on (a) MgO and (b) $SrTiO_3$. The external field was applied parallel and perpendicular to the sample surface.

[166] VSM measurements were carried out at Anadolu University, Faculty of Engineering, Department of Materials Sciences and Engineering.

[167] Additional coils inside the pole shoes of the external magnetic field.

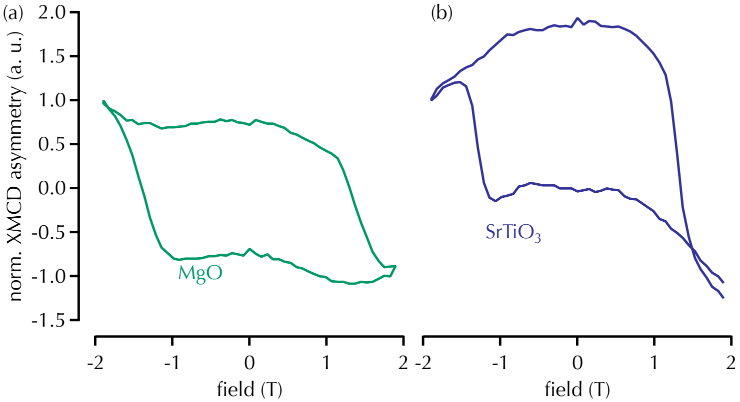

Figure 85: Normalized XMCD asymmetry of a $Mn_{2.7}Co_{0.3}Ga$ thin film on (a) MgO and (b) $SrTiO_3$. The external field was applied perpendicular to the sample surface.

First we investigated the cubic $Mn_{2.3}Co_{0.7}Ga$ compound on MgO and $SrTiO_3$ as follows. Figure 84 illustrates the respective in-plane and out-of-plane magnetization loops. The obtained hystereses show a soft-magnetic character. The out-of-plane and in-plane curves exhibit the same coercivity of 550(5) Oe for thin films on MgO and 500(5) Oe for thin films on $SrTiO_3$ substrates. This behavior underlines the soft-magnetic qualities of the Mn poor Mn-Co-Ga compound. Apart from the cubic structure, we investigated the tetragonally distorted phase. Figure 85 depicts the determined element-specific hysteresis loops of $Mn_{2.7}Co_{0.3}Ga$ thin films, prepared from the $Mn_{45}Ga_{55}$ target, on MgO and $SrTiO_3$. The hysteresis loops indicate a hard-magnetic behavior with an out-of-plane coercive field of 1.3(1) T for both samples.

The magnetization of an analogous sample on MgO, but deposited from a $Mn_{60}Ga_{40}$ target, i.e., a $Mn_{2.6}Co_{0.3}Ga$ layer was investigated by SQUID measurements. The dia-/paramagnetic background was subtracted by subtraction of a line. Figure 86 depicts the obtained magnetization loop. The shape of the major loop shows two unexpected features that are marked by red arrows. Comparing the shape of the loop with that of the major loops obtained for $D0_{22}$-$Mn_{3-x}Ga$ (cf. Figure 27 (b)) we see an inverted behavior. At zero field the magnetization of the Mn-Co-Ga sample increases, whereas the magnetization of the $Mn_{3-x}Ga$ sample decreases. The step in the hysteresis of the $Mn_{3-x}Ga$ was attributed to a second, soft-magnetic phase. A second phase that results in a higher magnetization at zero field, like seen in the major loop of the Mn-Co-Ga, is highly implausible. The only

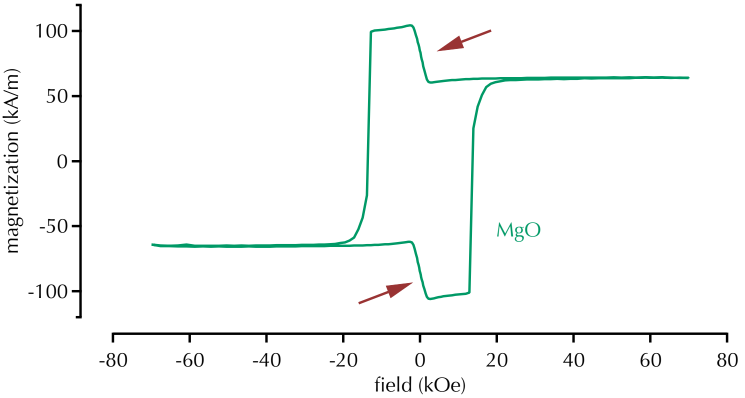

Figure 86: Hysteresis loop of a 38.50(5) nm thick $Mn_{2.6}Co_{0.3}Ga$ thin film on MgO deposited at 500 °C. Unexpected steps are present in the magnetization loop (indicated by red arrows).

reasonable explanation is an incorrect measurement.

The coercive field is estimated to 13.0(5) kOe and is equal to that of the $Mn_{2.7}Co_{0.3}Ga$ thin films. The magnetization is determined to 65(1) kA $m^{-1}$ at high field and 105(1) kA $m^{-1}$ at zero field. These values are low in comparison to the magnetization values of the $Mn_{3\text{-}x}Ga$ samples. Therefore the obtained results correspond to the reported data from Winterlik et al.[168] for $Mn_{3\text{-}x}Ga$ and Alijani et al.[169] for Mn-Co-Ga. Alijani et al.[170] reported a lower magnetic moment for Mn-Co-Ga bulk samples compared to $Mn_3Ga$. With increasing Co content the magnetic moment decreases, whereas the magnetic moment increases after transition into the cubic phase. Additionally, Ouardi et al. reported a low magnetic moment of 0.84 $\mu_B$ for a $Mn_{2.6}Co_{0.3}Ga_{1.1}$ thin film on MgO.[171] For the cubic phase a typical Slater-Pauling type behavior was reported and for the tetragonal phase a linear dependency according to $m_{tetra} = 1 - 1.34x$, with $x$ the Co concentration.

## *Soft x-ray absorption spectroscopy*

The chemical and magnetic properties were investigated by XAS and XMCD measurements at BL 4.0.2 and BL 6.3.1 at the ALS in Berkeley, California. Figure 87 illustrates the element specific XA and XMCD spectra of a $Mn_{2.3}Co_{0.7}Ga$ thin film on MgO. The Mn- and Co-spectra were obtained by bulk-sensitive LM mode at RT. A surface-sensitive TEY measurement could not be obtained due to the non-conducting thin film induced by the high surface roughness. Both spectra were normalized to the post-edge jump height. The Mn-spectrum shows two additional features (indi-

[168] J. Winterlik et al. In: *Physical Review B* 77.5 (2008)

[169] V. Alijani et al. In: *Applied Physics Letters* 99.22 (2011)

[170] V. Alijani et al. In: *Applied Physics Letters* 99.22 (2011)

[171] S. Ouardi et al. In: *Applied Physics Letters* 101.24 (2012)

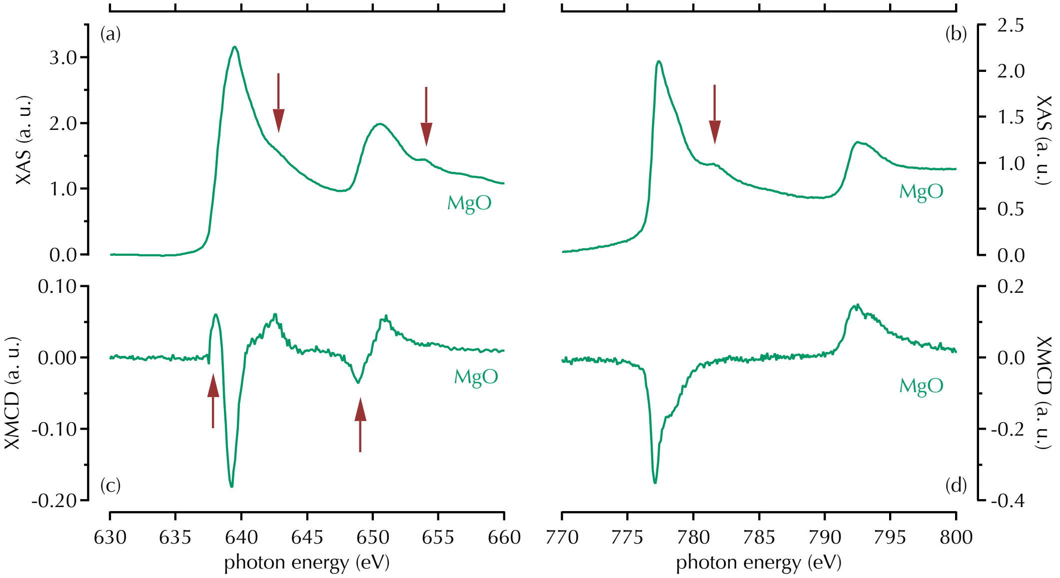

Figure 87: The bulk-sensitive (a) Mn- and (b) Co-XA spectra and the corresponding (c) Mn- (d) and Co-XMCD spectra of a $Mn_{2.3}Co_{0.7}Ga$ thin film on MgO. The absorption spectra are normalized to the post-edge jump height ($\eta = 1$). The red arrows indicate unexpected features. The sample was measured at BL 4.0.2.

cated by arrows). The feature at photon energies above the $L_3$ resonance could be an indicator of the formation of Mn–O, but this deduction is questionable. The second feature is induced by a second order Mg peak ($K_1 = 1303.0\,\mathrm{eV}$), caused by higher order contributions of the beamline and the MgO substrate. An additional feature is also found in the Co-spectrum at an energy above the $L_3$-edge (cf. Figure 87 (b)). However, the shape of the spectrum differs from that of pure Co but is also incompatible with the typical multiplet structure of Co–O. Schmalhorst et al.[172] reported a similar behavior in $Co_2MnSi$ and Ebke et al.[173] in $Co_2FeAl$ Heusler compounds. Both attributed the feature to ordered interfacial spins. Thus a certain atomic and magnetic order of the $Mn_{2.3}Co_{0.7}Ga$ is determined. Figure 87 (c) shows the Mn-XMCD spectrum, additional features were found as reported by Meinert et al.[174] for $Mn_2CoGa$ thin films and attributed to band structure effects. By comparing the Mn- and Co-XMCD spectra, we could draw conclusions about the relative orientation of the magnetic moments. Here, the (effective) Mn and Co magnetic moments are parallel-aligned (cf. Figure 87 (d)).

In addition, we have investigated $D0_{22}$-ordered $Mn_{2.7}Co_{0.3}Ga$ thin films on MgO and $SrTiO_3$ substrates.[175] This time the surface-sensitive TEY mode was used. In Figure 88 the obtained XA and

[172] J. Schmalhorst et al. In: *Physical Review B* 70.2 (2004)

[173] D. Ebke et al. In: *IEEE Transactions on Magnetics* 46.6 (2010)

[174] M. Meinert et al. In: *Physical Review B* 84.13 (2011)

[175] Prepared from the $Mn_{45}Ga_{55}$ target

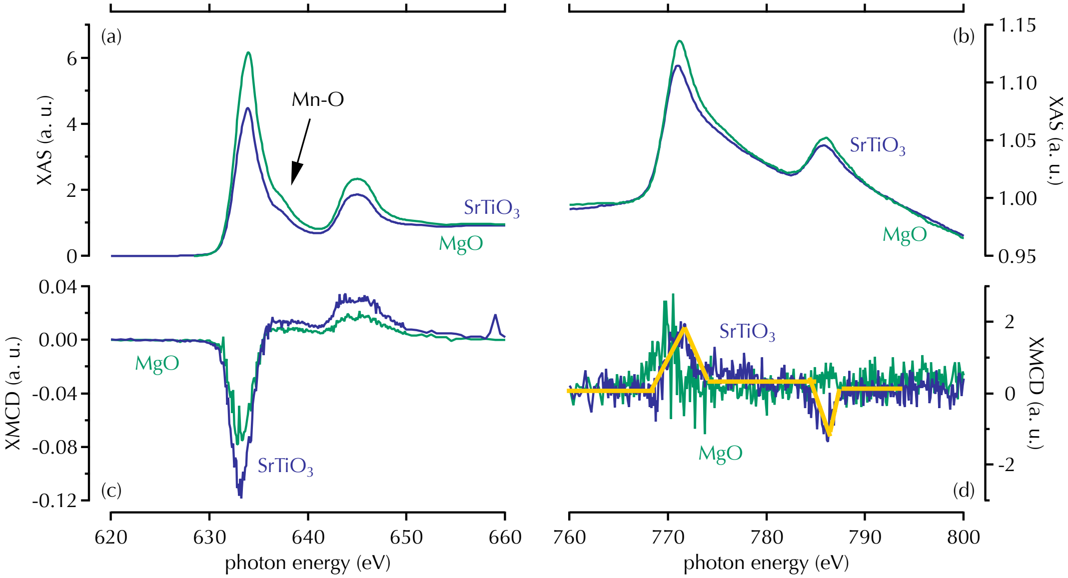

Figure 88: (a) Mn and (b) Co XA spectra and the corresponding (c) Mn (d) Co XMCD spectra of $Mn_{2.7}Co_{0.3}Ga$ thin films on MgO (green) and $SrTiO_3$ (blue). The yellow line in (d) has been inserted to guide the reader's eye. The samples were measured at BL 6.3.1.

XMCD spectra are depicted. The Mn-XAS was normalized to the post-edge jump height, i.e., $\eta = 1$ (cf. Figure 88 (a)). The feature at photon energies above the $L_3$-edge is clear evidence of the formation of Mn–O. Thin films on both substrates show this additional feature. The spectrum is not distinct enough to distinguish between MnO, $MnO_2$, and $Mn_2O_3$. The corresponding Mn-XMCD spectrum is noisy with additional spikes. However, a qualitative prediction about the magnetic moment could be made by comparing the amplitude of the XMCD signal normalized on the $L_3$-edge height.[176] The magnetic moment of the $Mn_{2.7}Co_{0.3}Ga$ thin film deposited on $SrTiO_3$ is higher compared to that of the film on MgO. Most likely, the lower magnetic moment is based on the higher amount of Mn–O for the sample on MgO. This correlation between the magnetic moment and the amount of Mn–O has been shown previously for $Mn_{3\text{-}x}Ga$ thin films. In Figure 88 (b) the Co absorption spectra are illustrated. The spectra were normalized to unity for energies lower than the $L_3$-edge. The signal strengths are lower compared to the Mn signals due to the small amount of Co in the samples. Hence, the corresponding XMCD signals are even noisier and a determination of the magnetic moment or an estimation, as done for Mn, is not possible. However, the shape of the XMCD signal (yellow line for clarifica-

[176] Because of the noisy XMCD signal, a calculation of the magnetic moment by the sum rules would involve a high error rate.

tion) reveals antiferromagnetic coupling between the Mn and Co magnetic moments for the thin film on $SrTiO_3$. The signal of the Mn-Co-Ga layer on MgO is too noisy to make an estimation of the alignment of the magnetic moments. The antiferromagnetic coupling is the reason for the lower magnetic moment in the $D0_{22}$ crystal structure. Therefore, the intended compensation of the magnetic moment has been achieved. This is a good example of the customizable properties of Heusler compounds and the reason for their high applicability.

## *Ferromagnetic interlayers*

Next, we will investigate the influence of a ferromagnetic layer between the $Mn_{2.7}Co_{0.3}Ga$ thin film and the MgO barrier on the formation of Mn–O. As seen before for the $Mn_{3\text{-}x}Ga$ compound two commonly known ferromagnetic layers were used, $Co_{40}Fe_{40}B_{20}$ and $Co_2FeAl$. The insertion layer was always deposited at RT. The respective thickness of the Co-Fe-B and $Co_2FeAl$ layers was 1 nm. Figure 89 illustrates the obtained Mn-XA and XMCD spectra for samples with a Co-Fe-B and a $Co_2FeAl$ interlayer on MgO and $SrTiO_3$ substrates, respectively. The XA and XMCD spectra were normalized to the post-edge jump height. The previously

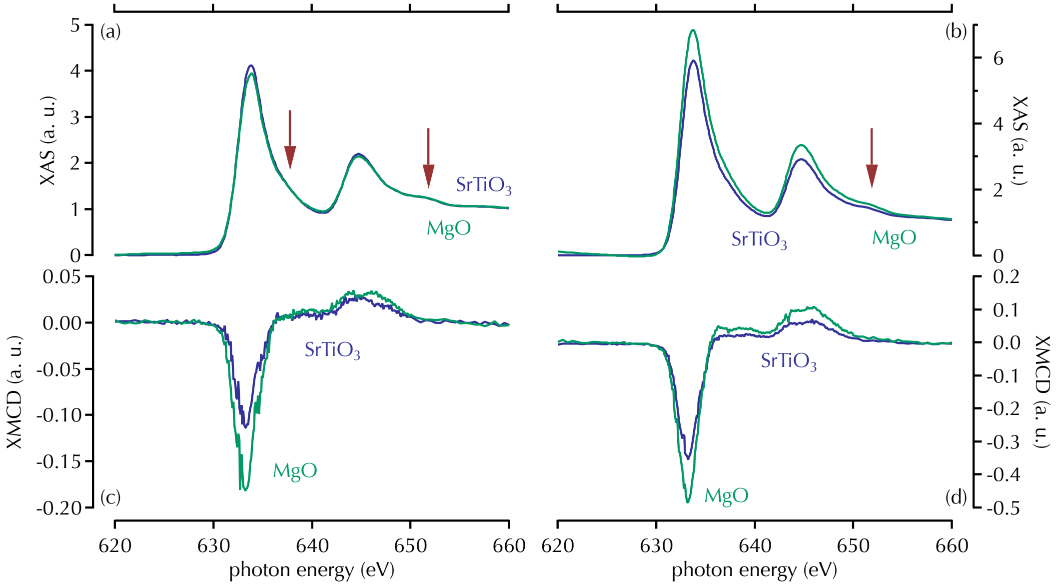

Figure 89: Mn-XA spectra of $Mn_{2.7}Co_{0.3}Ga$ on MgO (green) and $SrTiO_3$ (blue) with (a) Co-Fe-B and (b) $Co_2FeAl$ interlayer. (c) and (d) illustrates the corresponding XMCD spectra. The red arrows indicate unexpected features.

determined Mn–O at the interface for samples without interlayer is reduced by a Co-Fe-B layer (cf. Figure 89 (a) red arrow). Again a second order Mg peak is found, indicated by a red arrow, at 8 eV above the $L_2$-edge. The peak is induced by the MgO substrate and/or the MgO capping layer. Figure 89 (b) illustrates the Mn absorption spectra for samples with a $Co_2FeAl$ interlayer. Here, the formation of interfacial Mn–O is also reduced and the second order Mg peak is visible. The XMCD spectra for both types of samples are noisy and therefore the calculation of the magnetic moment via sum rules difficult.[177] However, by comparing the XMCD signal normalized to the $L_3$-edge height of the two samples, one can see the qualitative aspects of the magnetic moment.

Figure 90 depicts the XMCD signal normalized to the $L_3$-edge for $Mn_{2.7}Co_{0.3}Ga$ thin films on MgO and $SrTiO_3$ with a Co-Fe-B, a $Co_2FeAl$, and without an interlayer. Samples prepared on MgO exhibit the highest values if a ferromagnetic layer is inserted, whereas without an interlayer the normalized XMCD signal shows a minimum. For Mn-Co-Ga thin films on $SrTiO_3$ the Mn moment is equal for samples with a Co-Fe-B and without an interlayer. However, analogously to the samples on MgO the maximum XMCD signal was found for samples with a $Co_2FeAl$ interlayer. This behavior suggests the lowest amount of Mn–O for samples with a $Co_2FeAl$ interlayer and for samples on MgO substrates. This is plausible because the samples on MgO revealed a higher crystallinity and thus a higher compensation of the magnetic moments.[178]

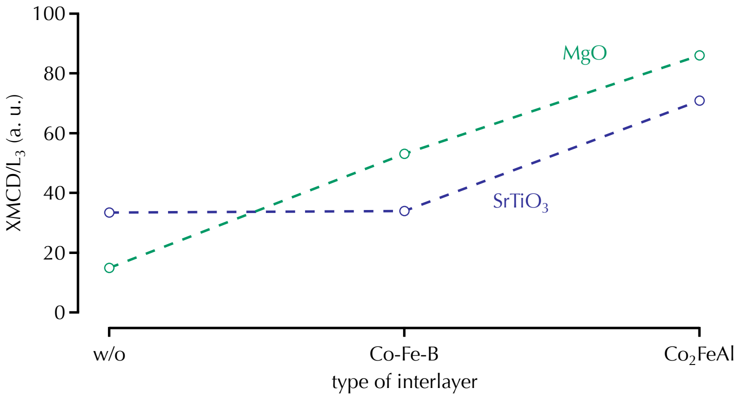

Figure 90: Normalized Mn-XMCD signal for $Mn_{2.7}Co_{0.3}Ga$ on MgO (green) and $SrTiO_3$ (blue) with a Co-Fe-B, a $Co_2FeAl$ and without an interlayer.

[177] The errors would be too high.

[178] Only for samples prepared by the $Mn_{45}Ga_{55}$ target.

# *Conclusion*

In summary, we successfully prepared cubic $Mn_{2.3}Co_{0.7}Ga$ on MgO and $SrTiO_3$ and tetragonally distorted $Mn_{2.7}Co_{0.3}Ga$ thin films on MgO and $SrTiO_3$. The thin films were prepared using a $Mn_{45}Ga_{55}$ composite target and an additional Mn and Co target. To investigate the dependence of the deposition conditions on the film properties, the $Mn_{45}Ga_{55}$ target was exchanged for a $Mn_{60}Ga_{40}$ target. That way, the power applied to the additional Mn target could be lowered by a factor of two and we obtained $D0_{22}$-ordered $Mn_{2.6}Co_{0.3}Ga$ thin films on MgO and $SrTiO_3$ substrates. We observed a phase transition from the cubic structure for $x \geq 0.5$ into the tetragonally distorted structure for $x \leq 0.5$. The surface roughness was measured by means of XRR measurements and showed a strong dependence on the co-deposition process. Samples prepared from the $Mn_{45}Ga_{55}$ target revealed the highest surface roughness. By using the $Mn_{60}Ga_{40}$ target a surface roughness of around 0.6(1) nm was achieved on $SrTiO_3$ substrates. XRD measurements proved a cubic phase for Mn poor samples on MgO and $SrTiO_3$. The Mn rich samples prepared from the $Mn_{45}Ga_{55}$ target exhibit a $D0_{22}$ phase on MgO and $SrTiO_3$. By lowering the deposition temperature to 500 °C and using the $Mn_{60}Ga_{40}$ target, the $Mn_{2.6}Co_{0.3}Ga$ thin films on $SrTiO_3$ and MgO crystallized in the $D0_{22}$ structure with a negligible cubic phase. VSM measurements proved the reported soft-magnetic properties of the cubic phase. Element-specific hysteresis loops of the $Mn_{2.7}Co_{0.3}Ga$ thin films on MgO and $SrTiO_3$ verified the hard-magnetic properties ($\vec{H}_c = 1.3(1)\,\mathrm{T}$) of the the $D0_{22}$ phase. SQUID observations revealed a lower magnetic moment compared to $Mn_{3\text{-}x}Ga$ thin films. In addition, surface and bulk-sensitive XAS and XMCD measurements were carried out. The formation of interfacial Mn−O was observed, but by using a ferromagnetic interlayer the amount of Mn−O could be decreased. The lowest amount of Mn−O was found for samples with a 1 nm $Co_2FeAl$ interlayer. Due to the promising results with regard to the surface roughness and hard-magnetic properties the integration of Mn-Co-Ga thin films in MTJ's is being planned.

# *The binary Mn-Ge compound*

*In the previous chapters we investigated the perpendicularly magnetized* $Mn_{3\text{-}x}Ga$ *and* $Mn_{3\text{-}x}Co_xGa$ *compounds. Next, we will discuss the properties of the recently reported* $Mn_{3+x}Ge$ *compound. Therefore, we prepared thin films with different compositions (*$x = -0.3, 0.2, 0.6$*). We studied the surface roughness and the crystallographic properties via XRR and XRD measurements. The magnetic properties were examined by anomalous Hall effect measurements.*

## *Stoichiometry dependence*

Over the years there were a lot of publications about $Mn_{3\text{-x}}Ga$ and $Mn_{3\text{-x}}Co_xGa$ tunnel junctions. Theoretically predicted high TMR effects were reported. However, the effects obtained at RT fall short of expectations. The TMR effects achieved for $Mn_{3\text{-x}}Ga$ based MTJ's without a ferromagnetic interlayer never exceed 10 % at RT.[179] The highest reported TMR effect was 40 % at RT (80 % at 5 K) for a stack consisting of Cr (40 nm)/$Mn_{62}Ga_{38}$ (30 nm)/Co (1.8 nm)/Mg (0.4 nm)/MgO (1.8 nm)/CoFeB (1.2 nm) on an MgO substrate.[180] Therefore, the necessity of an interlayer to observe reasonable TMR ratios was shown. However, ferromagnetic interlayers bear the disadvantage of low spin polarization and a high magnetic moment. Furthermore, ferromagnetic materials, e.g. Co-Fe-B, without $Mn_{3\text{-x}}Ga$ buffer achieve considerably higher TMR effects.[181] In addition, the question why a pure $Mn_{3\text{-x}}Ga$ electrode in contact with an MgO barrier shows no decent TMR effect was recently answered by Miura et al.[182] They reported first-principle calculations on TMR effect of MTJ's with $D0_{22}$-$Mn_3Z$ (Z = Ga, Ge) electrodes. The obtainable TMR effect strongly depends on the interface termination, i.e., whether a MnMn or a MnGa configuration is next to the MgO barrier (cf. Figure 91). Considering the dependence of the in-plane wave vector $k_{\|} = (k_x, k_y)$ on the tunneling conductance, they observed a broad peak at

[179] Q. L. Ma et al. In: *Applied Physics Letters* 101.3 (2012)

[180] Q. L. Ma et al. In: *Applied Physics Letters* 101.3 (2012)

[181] S. Yuasa et al. In: *Applied Physics Letters* (2006)

[182] Y. Miura and M. Shirai. In: *IEEE Transactions on Magnetics* 50.1 (2014)

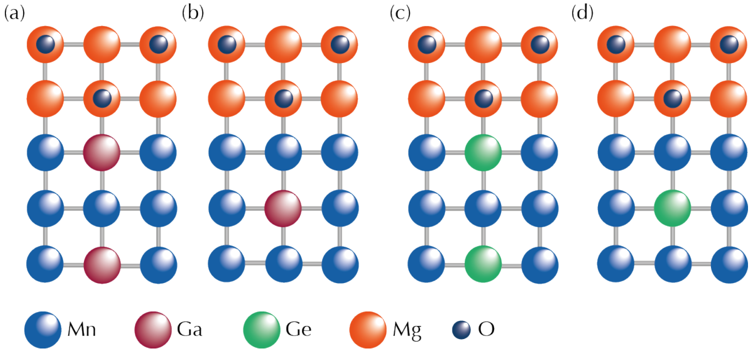

Figure 91: (a) MnGa and (b) MnMn-terminated $Mn_3Ga/MgO$ interface. (c) and (d) replacement of Ga by Ge.[183]

$k_{||} = (0, 0)$ for a MnGa termination. Thus the tunneling of the $\Delta_1$ electrons is dominant even in the anti-parallel state and a small TMR effect is observed. Replacing the Ga by Ge, the $k_{||}$ dependence shows spikes for both types of termination. That way, there is no contribution of the $\Delta_1$ electrons in the anti-parallel state. They also reported a half-metallic behavior of $Mn_3Ge$ on the $\Delta_1$ band around the Fermi level. However, by expanding the in-plane lattice by more than 4 % the half-metallic state of the $\Delta_1$ band vanishes. Therefore the use of an MgO barrier ($a^{MgO} = 4.21$ Å) is unsuitable due to the lattice mismatch of 11.2 % ($a^{MnGe}_{bulk} = 3.74$ Å). Other barrier materials like $CaF_2$ or $MgAl_2O_4$ are promising candidates. The theoretically predicted TMR values are illustrated in Table 16. Recently, Kurt et al.[185] reported the utilization of $D0_{22}$-ordered $Mn_3Ge$ thin films on $SrTiO_3$ substrates. The lattice constants were determined to be $a = 3.85(3)$ Å and $c = 7.185(7)$ Å. Additionally, a low magnetization of 73 kA m$^{-1}$ and an anisotropy constant of 0.91 MJ m$^{-3}$ were reported. The spin polarization was reported to be 46.0(2) % measured by point contact Andreev reflection. Furthermore, Sugihara et al.[186] reported the successful growth of $D0_{22}$-$Mn_{3\pm x}Ge$ on MgO substrates with a Cr buffer. The samples were post-annealed at different temperatures. Magnetic torque measurements[187] revealed an anisotropy constant of 1.15(3) MJ m$^{-3}$. A theoretically predicted low magnetic damping of $9 \times 10^{-4}$ was reported by Mizukami et al.[188] for $Mn_3Ge$. Kádár and Krén[189] reported a phase transition from the $D0_{22}$ structure into the $D_{19}$ phase at 850 K before reaching the Curie temperature. A Curie temperature of 920 K was estimated by extrapolation. Therefore the Curie temperature is 70 K higher compared to that of $Mn_{3\text{-}x}Ga$.[190]

| termination | TMR (%) |
|---|---|
| MnMn | $6.3 \times 10^2$ |
| MnGa | $4.0 \times 10^1$ |
| MnMn | $4.6 \times 10^3$ |
| MnGe | $1.4 \times 10^5$ |

Table 16: Estimated TMR effect for MnMn termination relative to MnGa or MnGe terminations of $Mn_3Ga/MgO$ or $Mn_3Ge/MgO$ interfaces.[184]

[183] Y. Miura and M. Shirai. In: *IEEE Transactions on Magnetics* 50.1 (2014)

[184] Y. Miura and M. Shirai. In: *IEEE Transactions on Magnetics* 50.1 (2014)

[185] H. Kurt et al. In: *Applied Physics Letters* 101.13 (2012)

[186] A. Sugihara et al. In: *Applied Physics Letters* 104.13 (2014)

[187] H. Miyajima. In: *Journal of Applied Physics* 47.10 (1976)

[188] S. Mizukami et al. In: *Applied Physics Express* 6.12 (2013)

[189] G. Kádár and E. Krén. In: *International Journal Magnetism* 143.1 (1971)

[190] J. Winterlik et al. In: *Physical Review B* 77.5 (2008)

At first glance, the reported properties are marginally better than for $Mn_{3\text{-}x}Ga$, but the first-principle calculations regarding the TMR effect are highly promising. However, one has to keep in mind that using an MgO barrier will lower the TMR effect, due to expansion in the *a*, *b*-plane and the resulting loss of half-metallic behavior.

We prepared different $Mn_{3+x}Ga$ ($x = -0.3$, 0.2 and 0.6) thin films on $SrTiO_3$ substrates, due to the low lattice mismatch (1.41 %) to the values reported by Kurt et al.[191]. Therefore, we ran a co-deposition process from a plain Mn and Ge sputtering target. The stoichiometry was changed by varying the power applied to the Mn target whereas the power applied to the Ge remain constant. The deposition temperature was 450 °C for the $Mn_{3.24(17)}Ge$ compound and 550 °C for the other two compositions. The respective stoichiometry was determined via XRF. To investigate the surface roughness and crystal structure, we carried out XRR and XRD analyses. The magnetic properties were measured via anomalous Hall effect (AHE) in a closed-cycle helium cryostat. The superconducting coils revealed a magnetic field up to ±4 T.

[191] H. Kurt et al. In: *Applied Physics Letters* 101.13 (2012)

## *X-ray fluorescence examinations*

The respective compositions were determined by means of XRF measurements in a He atmosphere. For this purpose three different $Mn_{3\pm x}Ge$ samples were prepared on $SrTiO_3$ substrates at two different temperatures (450 °C and 550 °C). By keeping the power applied to the Ge target fixed and adjusting the power on the Mn target, the composition was changed. In Table 17 the power, deposition temperature and obtained stoichiometry are listed. The effect of the deposition temperature seemed to be low in comparison to the power applied to the Mn target. Because of the low thin film thickness (around 30 nm), errors in the estimation of the stoichiometry might occur.

| Mn | Ge | temperature | composition |
|---|---|---|---|
| 90 W | 40 W | 550 °C | $Mn_{2.66(14)}Ge$ |
| 100 W | 40 W | 450 °C | $Mn_{3.24(17)}Ge$ |
| 110 W | 40 W | 550 °C | $Mn_{3.58(6)}Ge$ |

Table 17: Obtained XRF data for three different $Mn_{3\pm x}Ge$ samples on $SrTiO_3$.

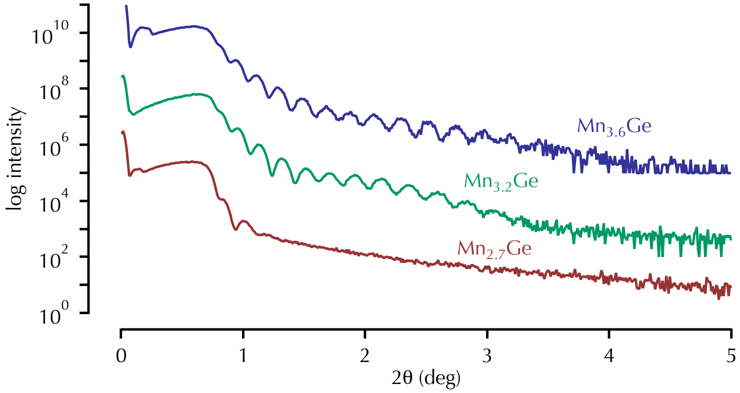

Figure 92: XRR scans of a $Mn_{2.7}Ge$ (red), a $Mn_{3.2}Ge$ (green), and a $Mn_{3.6}Ge$ (blue) thin films deposited on $SrTiO_3$ at different temperatures.

| composition | $d$ (nm) | roughness (nm) | $\rho$ (g cm$^{-2}$) |
|---|---|---|---|
| $Mn_{2.66(14)}Ge$ | % | % | % |
| $Mn_{3.24(17)}Ge$ | 33.0(5) | 1.3(1) | 7.50(5) |
| $Mn_{3.58(6)}Ge$ | 35.0(5) | 1.4(1) | 7.25(5) |

Table 18: Thin film thickness, surface roughness, and density for three different $Mn_{3\pm x}Ge$ compounds, determined from the XRR scans via Parratt algorithm. The XRR scan for the $Mn_{2.7}Ge$ cannot be fitted via Parratt algorithm.

## *X-ray reflectivity investigations*

The surface roughness, film thickness, and density of the $Mn_{3\pm x}Ge$ thin films were examined via XRR measurements. Figure 92 illustrates the corresponding XRR scans for all compositions. The values obtained by fitting via Parratt algorithm are displayed in Table 18. The scan of the $Mn_{2.7}Ge$ compound shows the absence of Kiessing fringes suggesting a high surface roughness. A fit via Parratt algorithm would have a low significance. However, the $Mn_{3.2}Ge$ and $Mn_{3.6}Ge$ thin films reveal nearly the same thickness. The obtained densities were in the same order as the densities of the $Mn_{3\text{-}x}Ga$ and $Mn_{3\text{-}x}Co_xGa$ thin films. The surface roughness for both compounds is above 1 nm and therefore in the same range as the barrier thickness in STT-MTJ's. For this reason, the surface roughness has to be decreased to increase the applicability of $Mn_{3\pm x}Ge$ based MTJ's.

## *Crystallographic structure*

Apart from the roughness, we analyzed the crystal structure by XRD measurements. In Figure 93 the obtained XRD scans are de-

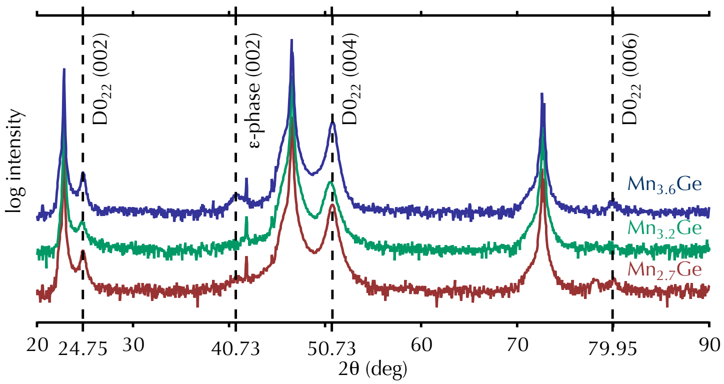

Figure 93: XRD scans of a $Mn_{2.7}Ge$ (red), a $Mn_{3.2}Ge$ (green), and a $Mn_{3.6}Ge$ (blue) thin films deposited on $SrTiO_3$.

picted. The $Mn_{2.7}Ge$ sample reveals the super lattice (002) reflex at 24.75 deg and the fundamental (004) reflex at 50.73 deg. An upcoming super lattice (006) reflex is present at 79.95 deg. Thus the out-of-plane lattice constant is determined to be 7.20 Å. The sample deposited at 450 °C with a $Mn_{3.2}Ge$ composition exhibits only the (002) reflex at 24.61 deg and the (004) peak at 50.51 deg. The corresponding $c$ lattice constant is 7.23 Å. The Mn rich sample shows the super lattice peaks (002) and (006) at 24.77 deg and 79.98 deg and the fundamental reflex at 50.75 deg. Therefore, the $c$ parameter is 7.19 Å (cf. Figure 94 (a)). Additionally, an upcoming reflex at 40.73 deg is visible, most likely evidence of the $\varepsilon$-Mn-Ge phase ($D0_{19}$).[192] This (002) peak corresponds to a lattice constant of 4.43 Å. The $\varepsilon$ phase will be found for a Ge content between 22 at % and 24 at % at high annealing tem-

[192] T. Ohoyama. In: *Journal of the Physical Society of Japan* 16.10 (2013)

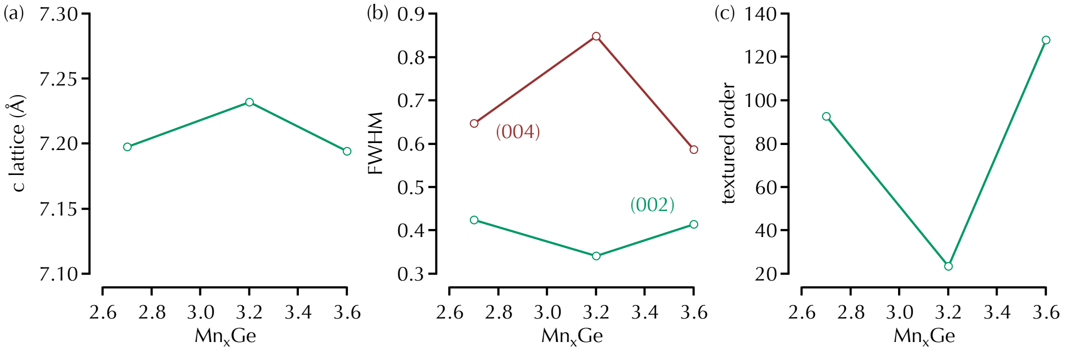

Figure 94: Parameter obtained from the XRD scans as a function of the stoichiometry. (a) $c$ lattice parameter, (b) FWHM of the (002) (green) and (004) (red) reflex, and (c) the textured order of the respective thin film.

peratures around 800 °C but also in a metastable phase around 515 °C.[193] The $Mn_{3.2}Ge$ thin film revealed the highest $c$ value, probably induced by the lower deposition temperature. Thus, the non-apparent (006) reflex could also be explained.

Additionally, we determined the dependence of the FWHM and textured order on the stoichiometry (cf. Figures 94 (b) and 94 (c)). The lowest FWHM of the (004) reflex is found for the Mn rich and poor thin films that were deposited at 550 °C. However, the lowest FWHM value of the (002) reflex is obtained for the $Mn_{3.2}Ge$ compound. The textured order reflects the results from the FWHM observation, the lowest value is found for the $Mn_{3.2}Ge$ compound. This suggests a low crystalline quality due to the low deposition temperature.

However, the textured order values are much lower than for the $L1_0$- and $D0_{22}$-ordered $Mn_{3-x}Ga$ and the $D0_{22}$-ordered Mn-Co-Ga thin films on $SrTiO_3$. Thus, only a small portion of the $Mn_{3\pm x}Ge$ thin film is crystallized. In this way, the $Mn_{3\pm x}Ge$ compound reveals the lowest crystalline quality of the three different compounds.

## *Magnetic properties*

The magnetic properties were analyzed by means of anomalous Hall effect (AHE) measurements. The ordinary Hall effect (OHE) occurs in non-magnetic metals; when a current is driven longitudinally to the sample and an external magnetic field is applied perpendicularly to the current a transversal voltage, Hall voltage, is detected. The force experienced by the charge carriers is the Lorentz force. The transversal resistivity increases linearly with the field applied,

$$\varrho_{xy} = R_H B_z \tag{49}$$

where $R_H = E_y/(j_x\vec{B})$ is the ordinary Hall coefficient. For magnetic materials the behavior is different, the AHE is often higher. The transverse resistivity is defined as

$$\varrho_{xy} = R_H B_z + R_S M_z \tag{50}$$

with $R_S$ the anomalous Hall coefficient. Instead of a linear decrease of $\varrho_{xy}$ with increasing $\vec{B}$, here a strong linear increase followed by a second increase with a lower gradient is found. Thus the underlying mechanism is not only the Lorentz force. The first theoretical attempt to describe the AHE was made by Karplus and Luttinger[194] in 1954. This *intrinsic* contribution relates to an

[193] T. Ohoyama. In: *Journal of the Physical Society of Japan* 16.10 (2013); E. Arras et al. In: *Physical Review B* 83.17 (2011); N. Yamada et al. In: *Physica B* 149.1-3 (1988)

[194] R. Karplus and J. Luttinger. In: *Physical Review* 95.5 (1954)

additional contribution to the group velocity of charge carriers induced by an external electric field. The intrinsic contribution depends only on the band structure. Since the discovery of the AHE in paramagnetic materials, the Berry phase theory of Bloch states entered the field of AHE.[195] The Berry phase theory shows similarities to the theory of Karplus and Luttinger. Besides the intrinsic contribution, two additional *extrinsic* contributions were reported by Smit[196] in 1955 and Berger[197] in 1970. What is called asymmetric skew scattering from impurities caused by the spin-orbit interaction was introduced by Smit. Another extrinsic effect is the side jump of quasiparticles upon scattering from spin-orbit coupled impurities, predicted by Berger.

With this measuring technique, the total magnetization value could not be obtained. However, the coercive field and squareness value were determined. The lowest coercive field is present for the $Mn_{2.7}Ge$ compound with 2.3(1) T. Still, the coercivity is higher than the highest value for the $Mn_{3\text{-}x}Ga$ and $Mn_{3\text{-}x}Co_xGa$ compounds. The $Mn_{3.2}Ge$ compound reveals a coercive field of 3.3(1) T. This is the highest coercive field achieved in this work. The $Mn_{3.6}Ge$ compound exhibits a lower value of 2.85(5) T. The squareness values decreased with increasing Mn content from 0.89 via 0.88 to 0.73. In addition, the obtained hysteresis loop of the $Mn_{3.6}Ge$ layer suggests an in-plane component. Sugihara et al.[198] reported the same behavior for a $Mn_{3.35}Ge$ compound. Therefore, a critical composition can be estimated, where the out-of-plane magnetization direction changes into the in-plane direction. For a precise determination, a composition dependent AHE investigation has to be carried out.

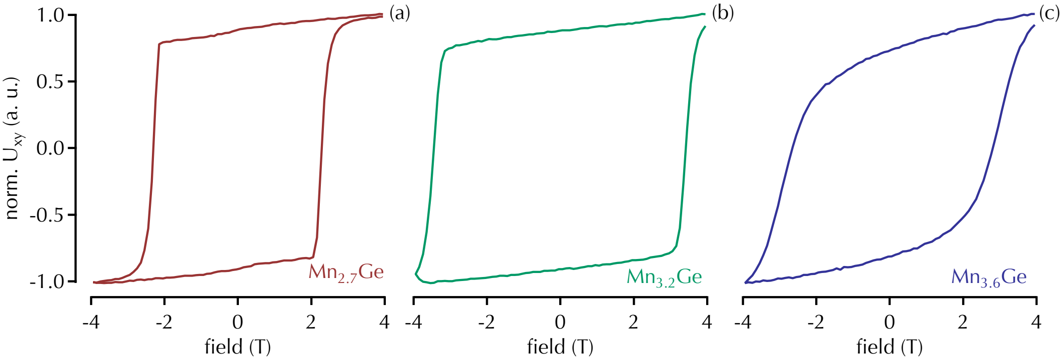

Figure 95: Comparison of hysteresis loops obtained from anomalous Hall effect measurements for (a) $Mn_{2.7}Ge$ (red), (b) $Mn_{3.2}Ge$ (green), and (c) $Mn_{3.6}Ge$ (blue) on $SrTiO_3$ substrates. The deposition temperature was 450 °C for the $Mn_{3.2}Ge$ sample and 550 °C for the two other compositions.

---

[195] J. Cumings et al. In: *Physical Review Letters* 96.19 (2006)

[196] J. Smit. In: *Physica* 21.6-10 (1955)

[197] L. Berger. In: *Physical Review B* 2.11 (1970)

[198] A. Sugihara et al. In: *Applied Physics Letters* 104.13 (2014)

# *Conclusion*

Summarizing this chapter, we successfully grew epitaxial $Mn_{3+x}Ga$ thin films with $x = -0.3, 0.2, 0.6$ on $SrTiO_3$ substrates. The deposition temperatures were 450 °C and 550 °C and chosen due to the results obtained for $Mn_{3-x}Ga$ and $Mn_{3-x}Co_xGa$. Nonetheless, the temperatures may not be ideal.

XRF measurements were carried out to determine the film stoichiometry. The film roughness was analyzed via XRR. The lowest surface roughness is 1.3(1) nm for the $Mn_{3.2}Ge$ thin film, whereas the highest value is found for the $Mn_{2.7}Ge$ sample. An optimization of the surface roughness is required for future integration into MTJ's. The crystal phases were determined via XRD. Each sample shows the fundamental (004) and super lattice (002) reflex. Apart from that the $Mn_{2.7}Ge$ and $Mn_{3.6}Ge$ thin films reveal the super lattice (006) peak. Most likely, the higher crystalline order was achieved due to the higher deposition temperature. The Mn-rich sample also exhibits the (002) reflex of an upcoming $\varepsilon$-Mn-Ge phase. Nonetheless, this sample shows the highest crystallinity with regard to the textured order and FWHM. However, compared to $Mn_{3-x}Ga$ and Mn-Co-Ga thin films on $SrTiO_3$ the obtained textured order values are much lower.

The magnetic properties were investigated by means of AHE measurements. A high coercive field of 3.3(1) T is present for the $Mn_{3.2}Ge$ sample and the lowest coercivity of 2.3(1) T for the $Mn_{2.7}Ge$ compound. Both samples revealed a squareness of around 0.9. The Mn-rich thin film shows an upcoming in-plane component that leads to the lowest squareness of 0.73. However, a high coercivity of 2.85(5) T is observed.

By comparing these results with the $Mn_{3-x}Ga$ and $Mn_{3-x}Co_xGa$ compounds on $SrTiO_3$ substrates, we see that the surface roughness is higher for the $Mn_{3\pm x}Ge$ thin films. In addition, the crystalline quality of the $Mn_{3-x}Ga$ and $Mn_{3-x}Co_xGa$ compounds, especially the $L1_0$-ordered $Mn_{3-x}Ga$ thin films, is better. The FWHM values are lower and the textured order is higher. $Mn_{2.7}Co_{0.3}Ga$ thin films on $SrTiO_3$ exhibit FWHM values comparable to those of the $Mn_{3\pm x}Ge$ thin films, whereas the textured order is higher. However, the magnetic properties in terms of coercivity and squareness are superior for the $Mn_{3\pm x}Ge$ compound. In a nutshell, by increasing the crystallinity and decreasing the surface roughness, the $Mn_{3\pm x}Ge$ compound will be a excellent replacement of the $Mn_{3-x}Ga$ and $Mn_{3-x}Co_xGa$ compounds.

Other properties that have to be investigated before integration into MTJ's are: the barrier interface, interdiffusion, and lateral expansion. The barrier interface concerning the formation of Mn–O or Ge–O has to be examined via XAS and XMCD measurements. As previously seen for the $Mn_{3\text{-}x}Ga$ compound, the interdiffusion of the elements was the reason for the low TMR effect. Hence, AES measurements are definitely required. After successful control of these factors, the remaining question will be the lateral expansion in case of an MgO barrier and the associated change in the band structure. The expansion could be reduced by a metallic interlayer. However, in that case the properties of the $Mn_{3\pm x}Ge$ layer, in terms of spin polarization, are insignificant. An advantage of the hard-magnetic seed layer is the induced pinning of the interlayer. That way, the absence of a perpendicular exchange bias could be overcome.

# *Co-Fe-B thin films*

*In this chapter $Co_{40}Fe_{40}B_{20}$ based MTJ's will be investigated. The Co-Fe-B compound is commonly known and already integrated into MRAM devices. We will investigate temperature dependent transport measurements and the electric field effect on the coercive field and TMR effect. The obtained TMR ratios are considerably higher compared to those of the previous compounds.*

In the previous chapters we investigated different Mn-based Heusler compounds. These compounds revealed certain characteristics which look promising for low critical current densities for STT switching. However, the obtained TMR effects never exceed 100 % at RT. For a commercial STT-MRAM an MTJ with a TMR effect of 200 % and an $AR$ of $10\,\Omega\,\mu m^2$ would be ideal. Therefore, the materials investigated in the previous chapters are no substitute for $Co_{40}Fe_{40}B_{20}$ at the moment. We will now take a closer look at Co-Fe-B based MTJ's and analyze the effect of an electric field on the critical current density. The electric field could lower the current density by a temporary decrease of the anisotropy energy.

Figure 96 illustrates different magnetization switching modes in MTJ's. $\vec{H}$-field-induced switching was applied in the previous chapters. This method is simple and still operates in first-generation spintronic devices and in conventional HDD's. However, the architecture of MRAM cells consisting of MTJ's, whose magnetization direction has to be changed via magnetic field, are complicated and small cells are almost impossible to manufacture. In the basic design, a read and write line, i.e., a conduction line is arranged next to the MTJ. Driving a current through the line induces a magnetic field that writes the information, i.e., changes the magnetization direction of the free layer.

By applying Newton's third law of motion *actio = reactio*, another switching mechanism comes into mind, called spin-transfer torque (STT) switching. A spin current carries angular momen-

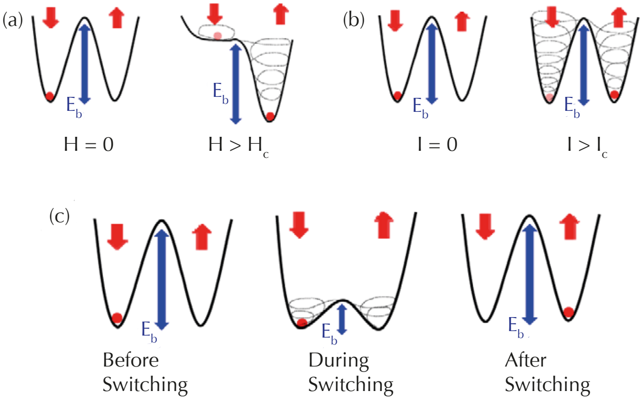

Figure 96: Schematic drawings of various switching modes: (a) $\vec{H}$-field-induced switching; (b) STT switching; (c) $\vec{E}$-field-induced switching with variable barrier height.[199]

tum, like an electric current is carried by moving charge. The angular momentum of the spin current can be transferred to the magnetization of a ferromagnetic electrode. The first theoretical approach was made by Slonczewski[200] and Berger[201]. The itinerant electrons in a ferromagnetic material are spin-polarized, thus a spin current is present. Interaction of the spin current with the magnetization result in a torque (cf. Figure 97).[202] The ferromagnetic magnetization dynamics are determined via the Landau-Lifshitz-Gilbert-Slonczewski Equation

$$\frac{\partial \vec{m}}{\partial t} = -\gamma \vec{m} \times \vec{H}_{\mathrm{eff}} + \alpha \vec{m} \times \frac{\partial \vec{m}}{\partial t} + \vec{\tau} \tag{51}$$

where $\vec{m}$ is the magnetization direction, $\gamma = g\mu_B\hbar^{-1}$ the gyromagnetic ratio, $\mu_B$ is the Bohr magneton and $g$ is the Lande g-factor,

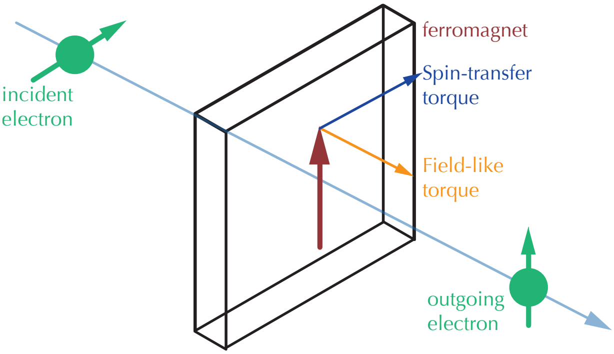

Figure 97: Schematic illustration of current-induced torques.[203]

[199] W. G. Wang and C. L. Chien. In: *Journal of Physics D: Applied Physics* 46.7 (2013)

[200] J. C. Slonczewski. In: *Journal of Magnetism and Magnetic Materials* 159 (1996)

[201] L. Berger. In: *Physical Review B* 54.13 (1996)

[202] A. Brataas et al. In: *Nature Materials* 11.5 (2012)

$\vec{H}_{\text{eff}}$ is an effective magnetic field, $\alpha$ is the Gilbert damping constant, and $\vec{\tau}$ denotes the current-induced torques (cf. Figure 98). The first term on the right side in Equation (51) describes the precession of the magnetization around an effective magnetic field $\vec{H}_{\text{eff}}$. The second term corresponds to the relaxation of the magnetization in the effective field direction. The last term $\vec{\tau}$ denotes the STT effect.

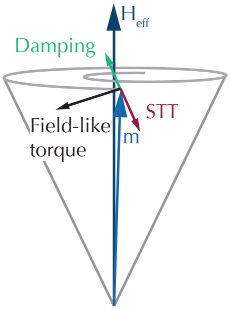

Figure 98: Illustration of the LLGS dynamics from Equation (51).

One important advantage of the STT effect over $\vec{H}$-field switching is the possibility of magnetization oscillation at gigahertz frequencies. For that reason, the read/write access is as fast as for DRAM structures.[204] The critical current densities for switching are defined as

$$\vec{j}_c^{\perp} = \frac{2\alpha e}{\hbar\zeta}\vec{M}_S d(\vec{H}_K^{\perp} \pm \vec{H}_{ext}), \tag{52}$$

$$\vec{j}_c^{\parallel} = \frac{2\alpha e}{\hbar\zeta}\vec{M}_S d(\vec{H}_K^{\parallel} \pm \vec{H}_{ext} + 2\pi\vec{M}_s). \tag{53}$$

In Equations (52) and (53), $e$ denotes the electron charge, $\alpha$ the damping constant, $\vec{M}_s$ the saturation magnetization, $d$ the thickness of the ferro(i)magnetic electrode, $\hbar$ the reduced Planck constant, $\vec{H}_{ext}$ is the external field, $\vec{H}_K$ is the effective anisotropy field including magnetocrystalline anisotropy and shape anisotropy, $\zeta$ is the spin-transfer efficiency.[205] Ikeda et al.[206] reported the following parameters for $Co_{20}Fe_{60}B_{20}$ thin films. The damping constant $\alpha$ depends on the film thickness and reveals values between 0.03 and 0.01 for thin films between 1 nm and 1.2 nm. $K \cdot d_{\text{CoFeB}}$ was reported to be $0.5\,\text{mJ}\,\text{m}^{-2}$, although this value also depends on the film thickness. The saturation magnetization was 1.58 T ($1257\,\text{kA}\,\text{m}^{-1}$). By applying Jullières model to the TMR effect a spin polarization of $p = 61\,\%$ was determined. These values are comparable to the ones obtained for $Mn_{3\text{-}x}Ga$, except for the lower spin polarization and higher magnetization. However, using the parameters of $Co_{20}Fe_{60}B_{20}$ a critical current density of approximately $7 \times 10^6\,\text{A}\,\text{cm}^{-2}$ was calculated. For example, Meng et al.[207] reported a critical current density of $2.1 \times 10^6\,\text{A}\,\text{cm}^{-2}$ for a stack consisting of Ta (5 nm)/CuN (50 nm)/Ta (3 nm)/CoFeB (1 nm)/MgO (1 nm)/CoFeB (1.16 nm)/Ta (10 nm)/CuN (10 nm)/Ru (7 nm). The low MgO thickness is necessary to enable STT switching, otherwise the applied voltage is too high. The achieved *AR* product was 16 Ω µm and the TMR effect 52 %. The low TMR ratio is based on the thin MgO barrier. Skowroński et al.[208] investigated the dependence of the TMR ratio on the *AR* product and attributed the lower effect to imperfections in the barrier. Thus

---

[203] A. Brataas et al. In: *Nature Materials* 11.5 (2012)

[204] W. J. Gallagher and S. S. P. Parkin. In: *IBM Journal of Research and Development* 50.1 (2006)

[205] $\zeta$ depends on the spin polarization $p$.

[206] S. Ikeda et al. In: *Nature Materials* 9.9 (2010)

[207] H. Meng et al. In: *Journal of Physics D: Applied Physics* 44.40 (2011)

[208] W. Skowroński et al. In: *Journal of Applied Physics* 107.9 (2010)

we are facing a predicament, the MgO barrier thickness has to be decreased to enable the STT process, but this means that the TMR effect decreases too.[209]

A promising attempt to overcome the obstacles of a low barrier thickness that also lowers the critical current density is an $\vec{E}$-field-induced switching process. Due to the low thin film thickness in Co-Fe-B based pMTJ's, usually below 2 nm, the electric field over the barrier induced by the applied bias voltage $U_b$ affects the charge carrier density at the MgO interface (cf. Figure 99). Over the years several groups reported $\vec{E}$-field effects in magnetic thin films.[210] The first investigations were made in 2000 by Ohno et al.[211] in magnetic semiconductors. The hole-induced ferromagnetism was modified via an electrical field. For a high negative (positive) $\vec{E}$-field, the concentration of holes was increased (decreased) and so was the Curie temperature. Endo et al.[212] investigated the dependence of magnetic anisotropy on electric field effects in Co-Fe-B thin films. They carried out AHE measurements with an additional $\vec{E}$-field parallel to the $\vec{H}$-field. The higher (lower) perpendicular anisotropy energy was attributed to a depletion (accumulation) of charge carriers at the interface. However, to the best of our knowledge a clear dependence between electron density $n$ and the PMA was not reported yet.[213] Only Maruyama et al.[214] showed a quantitative value for the relation of electron density and PMA in Fe thin films. By applying a bias voltage of 200 V an electron filling of $2 \times 10^{-3}$ electrons per Fe atom was determined. This corresponds to a change of the chemical potential by 2 meV. The reported $\vec{E}$-field dependence was used by Wang et al.[215] to obtain electric-field-assisted switching in MTJ's. By applying a bias magnetic and electric field ($\vec{H}_b$ and $\vec{E}_b$), an STT like switching of the electrodes was realized. This STT like switching effect is illustrated in Figure 101. Starting in a parallel state of the electrodes an external magnetic field is applied close to the switching of the soft electrode. Now an electric field is applied to reduce the coercive field of the soft electrode, thus the magnetization direction changes into the antiparallel state. The antiparallel state is stable even when the electric field is removed. To switch the hard electrode, i.e., achieve the parallel state again, an electric field of opposite polarity to the initial electric field is applied. Now the hard electrode shows a lower coercivity and the external magnetic field switches the electrode. Afterwards the electric and magnetic fields are removed and a stable parallel state is obtained. However, unlike the STT process this electric field induced switching

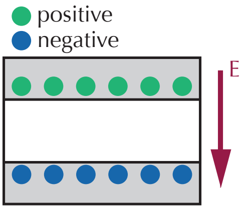

Figure 99: Charge carrier accumulation/depletion at the barrier interface induced by an electric field in pMTJ's.

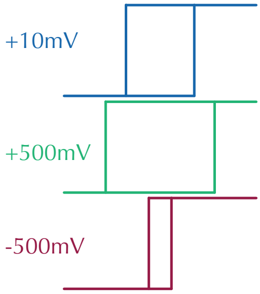

Figure 100: Minor loops for different bias voltages.

---

[209] Except for a perfectly crystalline MgO barrier.

[210] Y. Shiota et al. In: *Applied Physics Express* 2.6 (2009); T. Nozaki et al. In: *Applied Physics Letters* 96.2 (2010); T. Maruyama et al. In: *Nature* 4.3 (2009); M. Weisheit et al. In: *Science* 315.5810 (2007)

[211] H. Ohno et al. In: *Nature* 408.6815 (2000)

[212] M. Endo et al. In: *Applied Physics Letters* 96.21 (2010)

[213] $n$ can be calculated from the Hall constant.

[214] T. Maruyama et al. In: *Nature* 4.3 (2009)

[215] W. G. Wang et al. In: *Nature Materials* 11.1 (2011)

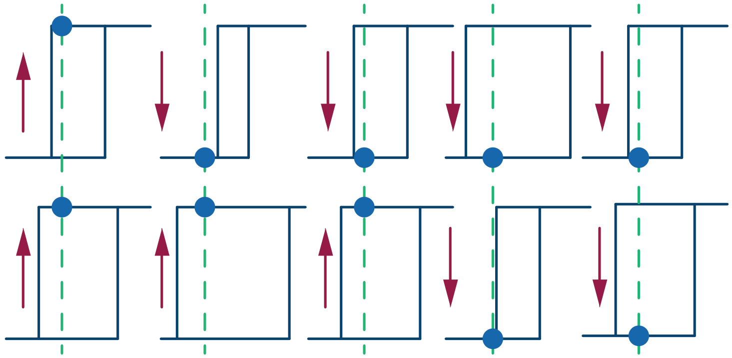

Figure 101: Schematic sketch of electric-field-assisted switching of MTJ's. The top row corresponds to the soft electrode and the bottom row to the hard electrode. The blue dots indicate the present state. The green dashed line corresponds to the external magnetic field, the red arrow specifies the magnetization direction of the respective electrode.[216]

requires an external magnetic field and the final parallel state differs from the initial parallel state. For that reason, to obtain a reproducible writing process the polarity of the $\vec{H}_b$ has to be changed. To overcome this obstacle Wang et al.[217] showed an electric-field-induced unipolar switching, a combination of STT and $\vec{E}$-field effect with an applied $\vec{H}$-field. The functionality of this switching process is as follows: an external bias magnetic field is applied during the whole process, then 200 ms pulses of a high negative voltage (−0.9 V) are applied and the magnetization direction of the soft electrode switches due to the STT effect. Afterwards an even higher negative bias pulse (−1.5 V) is applied for 200 ms. Now the induced $\vec{E}$-field reduces the coercive field and the applied $\vec{H}_b$ switches the soft electrode into the parallel state. The resulting current densities for this process were reported to be $-1.2 \times 10^4\,\mathrm{A\,cm^{-2}}$. Wang et al.[218] attributed the lower current density to the reduction of the energy barrier by $\vec{H}_b$. Nonetheless, one has to keep in mind that the applied $\vec{H}_b$ also decreases $\vec{j}_c$ (cf. Equation (52)). In addition, a 200 ms pulse is too slow for the implementation in MRAM devices because the transistor works in the GHz region. Recently, Kanai et al.[219] published a paper on magnetization switching in the nanosecond regime for Co-Fe-B based MTJ's by a combination of STT and $\vec{E}$-field effects. Therefore, they applied an external magnetic field to compensate the stray field $\vec{H}_s$ from the reference layer.[220] Then an initial pulse of 0.7 V was applied to switch into the antiparallel state. The magnetization of the soft layer precessed around the external magnetic field. The duration of the pulse was below 1.7 ns to

[216] W. G. Wang et al. In: *Nature Materials* 11.1 (2011)

[217] W. G. Wang et al. In: *Nature Materials* 11.1 (2011)

[218] W. G. Wang et al. In: *Nature Materials* 11.1 (2011)

[219] S. Kanai et al. In: *Applied Physics Letters* 104.21 (2014)

[220] The compensation field is probably always required for switching.

prohibit an oscillatory dependence of the switching probability. Afterwards, a lower voltage with same polarity (0.5 V) was applied to induce an STT effect. Due to the misalignment of the soft electrode magnetization direction, induced by the interplay of the magnetic and electric field, a high torque was applied to the Co-Fe-B layer. For that reason, the achieved current densities were as low as $3.5 \times 10^5\,\mathrm{A\,cm^{-2}}$. By combination of STT, $\vec{E}$-field and $\vec{H}$-field effects Kanai et al.[221] were able to lower the switching time. However, the necessity of an additional line for the magnetic field reduces the applicability of the Co-Fe-B based MTJ's. To overcome the required external magnetic field Alzate et al.[222] proposed using a non-zero leakage current acting as a field-like STT.

Another interesting phenomenon that occurs in thin, single-domain ferro(i)magnetic layers is superparamagnetism. Néel pointed out that thermal fluctuations in a single-domain particle could cause a Brownian-like magnetization rotation. The time between two flips of the magnetization direction is called Néel relaxation time

$$\tau_N = \tau_0 \exp\left(\frac{KV}{k_B T}\right) \tag{54}$$

with $K$ the anisotropy energy, $V$ the volume of the particle, $k_B$ the Boltzmann constant, $\tau_0$ the characteristic length of time of the order of $10^{-9}$ s, and $T$ the temperature. Without an external field, when the measuring time $\tau_M$ is larger then $\tau_N$ the magnetization of the sample seems to be zero. This state is called *superparamagnetic*. Therefore, the state of the particle depends on the measuring time. A transition between the superparamagnetic and the ferromagnetic state occurs when $\tau_M = \tau_N$. The temperature of the transition is called blocking temperature $T_B$,

$$T_B = \frac{KV}{k_B \ln\left(\frac{\tau_M}{\tau_0}\right)}. \tag{55}$$

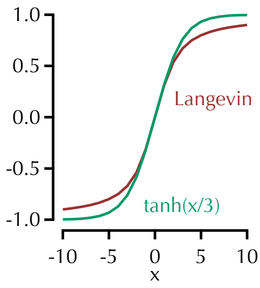

Figure 102: Comparison between the Langevin function (red) and the tanh($x/3$) function (green).

By applying an external magnetic field, the sample can be magnetized like a paramagnet but the magnetic moment is higher. For identical particles the magnetization depends on the external magnetic field like a Langevin function (cf. Figure 102):

$$\vec{M}(\vec{H}) = N\vec{m}\left(\coth\left(\frac{\vec{m}\vec{H}_{ext}}{k_B T}\right) - \frac{k_B T}{\vec{m}\vec{H}_{ext}}\right) = N\vec{m}L\left(\frac{\vec{m}\vec{H}_{ext}}{k_B T}\right) \tag{56}$$

$\vec{m}$ denotes the magnetic moment, $\vec{H}_{ext}$ the external magnetic field, $N$ the number of particles and $L$ the Langevin function.[223] If

[221] S. Kanai et al. In: *Applied Physics Letters* 104.21 (2014)

[222] J. G. Alzate et al. In: *IEEE International Electron Devices Meeting* (2012)

the temperature is high enough ($T \geq KV/k_B$) the magnetization shows a $\tanh(x)$ dependence.

Let us take an accumulation of non-interacting single-domain particles of same size with uniaxial anisotropy. In this case, the temperature dependence of the coercive field is given by the Stoner-Wohlfarth theory with thermal fluctuations:

$$\vec{H}_c(T) = \sigma \frac{2K}{\vec{M}_s} \left( 1 - \left( \frac{T}{T_B} \right)^{\frac{1}{2}} \right) \tag{57}$$

$\sigma$ is one if the particle easy axes are aligned or 0.48 if the particles are randomly oriented. $\sigma 2K/\vec{M}_s = \vec{H}_{c0}$ is the coercivity at 0 K.[224] However, for a system with different particle sizes the calculation of $\vec{H}_c$ faces some obstacles. For example the blocking temperature depends on the particle size (cf. Equation (55)). In addition, the average coercive field is smaller for superparamagnetic particles, whose relative fraction increases with increasing temperature, than for particles that remain blocked.[225]

Summarizing, the above-mentioned $\vec{E}$-field effects are interesting for usage in Co-Fe-B based MTJ's and MRAM devices. However, it is commonly known that the temperature in personal computers is above 300 K. Therefore, a superparamagnetic Co-Fe-B layer in an MRAM device would lead to data leakage.

In what follows, we will describe our transport measurements on Co-Fe-B based MTJ's with different barrier thicknesses. The transport properties will be analyzed regarding the temperature and bias voltage dependence.

We prepared typical Co-Fe-B based MTJ's (cf. Figure 103) with a bottom conduction layer consisting of Ta (5 nm)/Ru (30 nm)/Ta (5 nm). On top a 1 nm thick $Co_{40}Fe_{40}B_{20}$ layer was deposited forming the bottom electrode. The thickness of the following MgO barrier was varied from 1.5 nm to 2.6 nm. The top electrode consists of a 1.2 nm thick $Co_{40}Fe_{40}B_{20}$ layer. To prevent the stack from oxidizing a 5 nm thick Ta and 10 nm thick Ru layer were sputtered. The whole stack was prepared at RT and went through an additional ex-situ post-annealing process. The duration time was 60 min and the temperature 360 °C.[226] Thus the PMA of the Co-Fe-B electrodes and the crystallization of the MgO barrier in (001) direction were achieved. To support the formation of the PMA an external magnetic field of 6500 Oe was applied during the entire process. After the post-annealing process, we prepared tunnel junctions with sizes of 100 μm², 225 μm²

[224] C. P. Bean and J. D. Livingston. In: *Journal of Applied Physics* 30.4 (1959); E. C. Stoner and E. P. Wohlfarth. In: *Philosophical Transactions of the Royal Society of London. Series A. Mathematical and Physical Sciences* (1948)

[225] W. C. Nunes et al. In: *Physical Review B* 70.1 (2004)

[226] V. Drewello et al. In: *Physical Review B* 77.1 (2008); W. Skowroński et al. In: *Journal of Applied Physics* 107.9 (2010)

and 625 µm$^2$ by UV lithography and Ar$^+$ beam etching. Contact pads were formed by a 5 nm thick Ta and a 30 nm thick Au layer. More information about the stack preparation can be found elsewhere.[227]

Although You et al.[228] reported a polycrystalline orientation of MgO grown on amorphous Co-Fe-B, the post-annealing process reveals further advantages. During annealing a migration of B atoms occurs. In order to avoid the B diffusion into the MgO barrier, due to the high oxygen affinity of B, an amorphous material like Ta is deposited next to the Co-Fe-B electrodes. Therefore, the B is absorbed by the Ta layer and at the barrier interface a clean and highly crystallized Co-Fe layer is created.[229] It is worth noting that, the Ta diffuses into the Co-Fe-B layer and causes a magnetic dead layer (MDL) with a thickness of several Å. The thinner the magnetic dead layer, the better the stack quality. The MDL depends on the Ta thickness but could also be reduced by replacing Ta with Nb, Mo or FeZr.[230] Lee et al.[231] reported an estimated MDL of only 0.05 nm for the Nb buffer layer and 0.1 nm for the Ta layer. This could be an explanation for the lower coercive field of the Co-Fe-B with Nb seed layer. The interface anisotropy $K_i$ is in the range of 2 mJ m$^{-2}$ and 2.2 mJ m$^{-2}$ for a Nb and Ta layer. Mo increases the thermal stability of the MTJ and enables higher annealing temperatures up to 425 °C. Liu et al.[232] reported an interface anisotropy of 1.9 mJ m$^{-2}$ and a MDL of 0.25 nm. Amorphous FeZr is a good B absorber, because FeZrB is more stable than FeZr. To achieve a crystalline FeZr layer and thus reduce B absorption a temperature of 700 K has to be reached. The estimated MDL was reported to be 0.62 nm and the interface anisotropy to be 0.56 mJ m$^{-2}$. Because of the low MDL and the marginal differences between Nb and Ta we used a Ta buffer layer.

The transport measurements were carried out by conventional two probe technique in a closed-cycle helium cryostat (Oxford Cryodrive 1.5) within a temperature range between 15 K and 330 K.

## Temperature dependent transport measurements

The dependence of the TMR effect on the temperature for an MTJ stack with a 1.5 nm thick MgO barrier is depicted in Figure 104. Apart from the temperature dependence, the TMR effect shows dependence on element size (100 µm$^2$, 225 µm$^2$ and 625 µm$^2$).

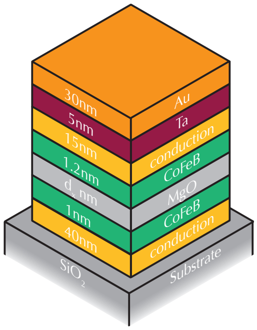

Figure 103: Typical Co-Fe-B based MTJ with 1 nm bottom and 1.2 nm top electrode. The thickness of the MgO barrier was varied between $d_x$ = 1.5 nm to 2.6 nm.

[227] A. Gebauer. Bachelor thesis. Bielefeld University, Faculty of Physics, 2014

[228] C. Y. You et al. In: *Journal of Applied Physics* 104.3 (2008)

[229] H. Kurt et al. In: *Applied Physics Letters* 96.26 (2010)

[230] D.-S. Lee et al. In: *IEEE Transactions on Magnetics* 50.7 (2014); T. Liu et al. In: *Scientific reports* 4 (2014); D. Kim et al. In: *Journal of Magnetism and Magnetic Materials* 375 (2015)

[231] D.-S. Lee et al. In: *IEEE Transactions on Magnetics* 50.7 (2014)

[232] T. Liu et al. In: *Scientific reports* 4 (2014)

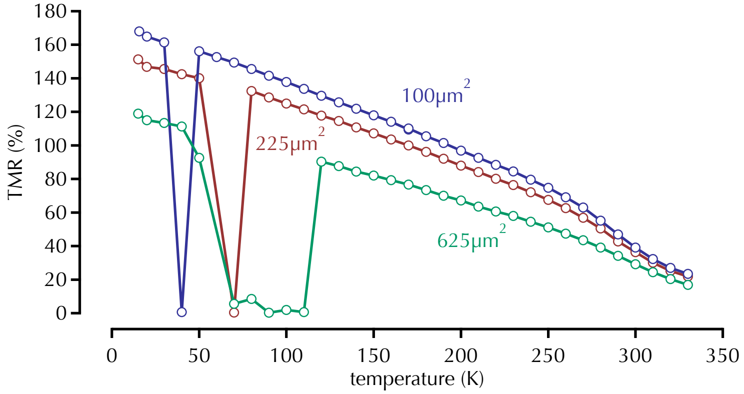

Figure 104: TMR effect over temperature for a stack with 1.5 nm thick MgO barrier. The MTJ areas are 100 µm$^2$ (blue), 225 µm$^2$ (red), and 625 µm$^2$ (green).

The highest (lowest) TMR effect is found for the smallest (largest) elements. For this reason, we will only consider the temperature dependence of the 100 µm$^2$ element. A TMR ratio of 39 % is found at 300 K. By decreasing the temperature to 15 K the TMR effect increases to 168 % ($\Gamma = 4.3$).[233] This temperature dependence is based on the constant parallel area resistance (*AR*) product, whereas the antiparallel *AR* increases. Attempts were made to describe this behavior by Shang et al.[234] and Moodera et al.[235] Both groups observed a temperature dependence of the spin polarization of the ferromagnetic electrodes. In addition, Drewello et al.[236] reported an expanded magnon model, where thermal smearing was taken into account. Furthermore, spin-flip effects, which are temperature dependent, are involved.[237] Hence, the increase of the TMR with decreasing temperature is clarified.

However, around 300 K the slope diverges from the almost linear increase and from 30 K to 120 K a decay of the TMR effect is visible for all element sizes. Very recently, Tsai et al.[238] reported a superparamagnetic state in MgO/Co-Fe-B/Ta structures. They carried out VSM measurements on flat samples. The obtained full hysteresis loops suggest a superparamagnetic state at around 280 K for a 1 nm thick Co-Fe-B layer that is used as bottom electrode. The top electrode, consisting of 1.2 nm Co-Fe-B, shows a superparamagnetic state at around 300 K. To determine the superparamagnetic state we shall take a closer look at the major loops at different temperatures (cf. Figure 105). The TMR effect at 230 K shows a distinct antiparallel state of the electrodes. The hard electrode switches sharply, whereas the soft electrode shows *s*-like switching. This *s*-shape becomes more distinct with increas-

[233] $\Gamma = \frac{\text{TMR(15 K)}}{\text{TMR(300 K)}}$

[234] C. H. Shang et al. In: *Physical Review B* 58.6 (1998)

[235] J. S. Moodera and G. Mathon. In: *Journal of Magnetism and Magnetic Materials* 200 (1999)

[236] V. Drewello et al. In: *Physical Review B* 77.1 (2008)

[237] J. Inoue and S. Maekawa. In: *Journal of Magnetism and Magnetic Materials* 198-199 (1999)

[238] C. C. Tsai et al. In: *IEEE Transactions on Magnetics* 50.1 (2014)

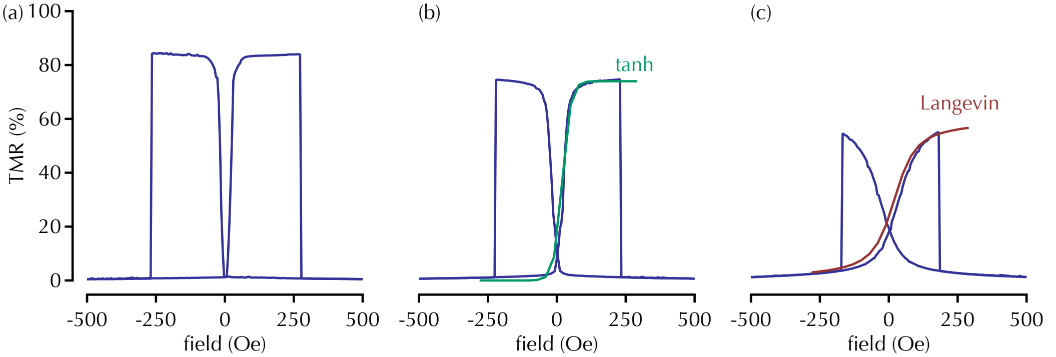

Figure 105: Different TMR curves at (a) 230 K, (b) 250 K, and (c) 280 K. The upcoming superparamagnetic state can be observed in the *s*-like curve of the soft electrode. The tanh (green) and Langevin function (red) were scaled and shifted to positive fields, but indicate the superparamagnetic state.

ing temperature (cf. Figures 105 (b) and 105 (c)). At a temperature of 250 K the major loop is similar to a tanh-function, which points to a superparamagnetic state. At 280 K the *s*-shape looks like a Langevin function. Because of the superparamagnetic electrode the antiparallel state is not achievable.

The remaining question is the decay of the TMR effect between 30 K and 50 K. Tsai et al.[239] reported a coercive field crossover in MgO/Co-Fe-B/Ta structures, due to differences in temperature dependence of the Co-Fe-B thin films. For this reason, during cooling or heating the soft (hard) electrode becomes the hard (soft) electrode (cf. Figure 106). Figure 107 illustrates our major loops obtained between 30 K and 50 K. At 30 K the coercive fields of the soft and hard electrode are almost equal. The antiparallel state is achieved, but only for around 15 Oe. By increasing the

[239] M. C. Tsai et al. In: *Journal of Applied Physics* 113.17 (2013)

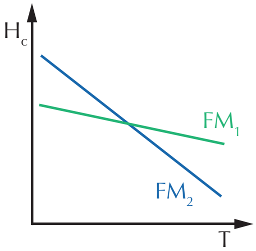

Figure 106: Schematic sketch of the coercive field crossover of electrode $FM_1$ (green) and $FM_2$ (blue).

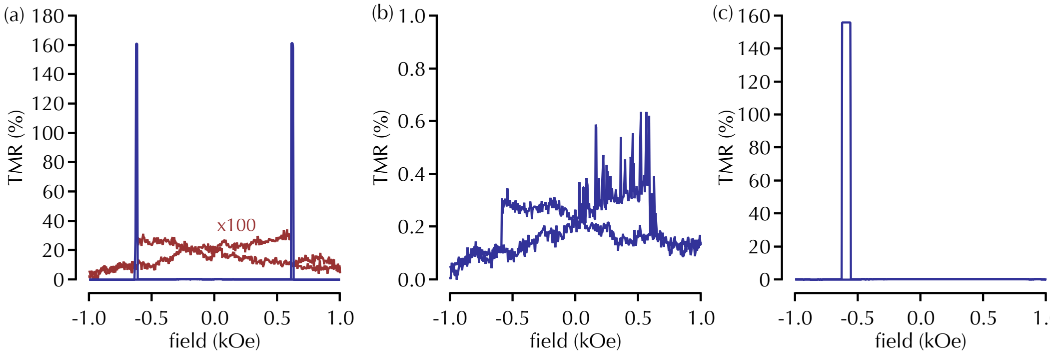

Figure 107: Major loops at (a) 30 K, (b) 40 K, and (c) 50 K that illustrate the crossover of the coercive fields. The red curve is an enlarged view of the background of the major loop at 30 K.

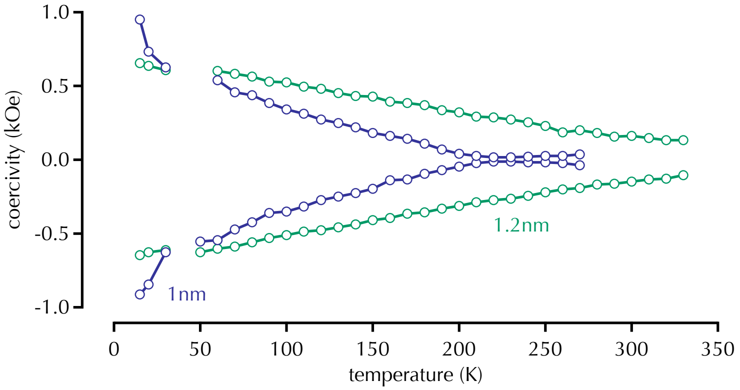

Figure 108: Coercive field of the 1 nm (blue) and 1.2 nm (green) thick Co-Fe-B electrodes depending on temperature. The MgO barrier thickness was 1.5 nm and the element size was 100 µm$^2$.

temperature to 40 K no antiparallel state is visible. The TMR signal is noisy and shows a linear slope until it drops sharply at around ±0.7 kOe. The achieved TMR effect is lower than 1 %. The underground signal is also seen in the TMR curve at 30 K (cf. Figure 107 (a)). By increasing the temperature to 50 K an upcoming TMR effect is visible. However, we are still in a critical temperature regime and thus the TMR effect is only visible on the negative $\vec{H}$-field side.[240] At higher temperatures the transport measurements show a typical TMR curve.

The temperature dependence of the coercive field $\vec{H}_c$ of both Co-Fe-B electrodes for the sample with a 1.5 nm thick MgO layer is shown in Figure 108. The coercivity is determined from the obtained major loops. Between 30 K and 50 K the hard electrode at RT, i.e., the 1.2 nm electrode, becomes the soft electrode and vice versa. The obtained graph was fitted by Equation (57) of the Stoner-Wohlfarth[241] model. Therefore, the dependence of $\vec{H}_c$ on $T^{1/2}$ was used. It has to be mentioned that the thin films of this size are not single domain particles. For this reason, the estimation of the blocking temperature via the Stoner-Wohlfarth model is more likely a first approximation. The determined val-

| | $T_B^{pos}$ (K$^{1/2}$) | $T_B^{neg}$ (K$^{1/2}$) | $H_{c0}^{pos}$ (Oe) | $H_{c0}^{neg}$ (Oe) |
|---|---|---|---|---|
| soft | 14.641(219) | 14.572(164) | 1122.00(3260) | −1142.40(2540) |
| hard | 20.655(123) | 20.4640(937) | 1000.4(109) | −997.58(811) |

Table 19: Data obtained from Figure 108 via Stoner Wohlfarth model (cf. Equation (57)).

[240] A second measurement at the same temperature could show a typical TMR loop or the same loop.

[241] E. C. Stoner and E. P. Wohlfarth. In: *Philosophical Transactions of the Royal Society of London. Series A. Mathematical and Physical Sciences* (1948)

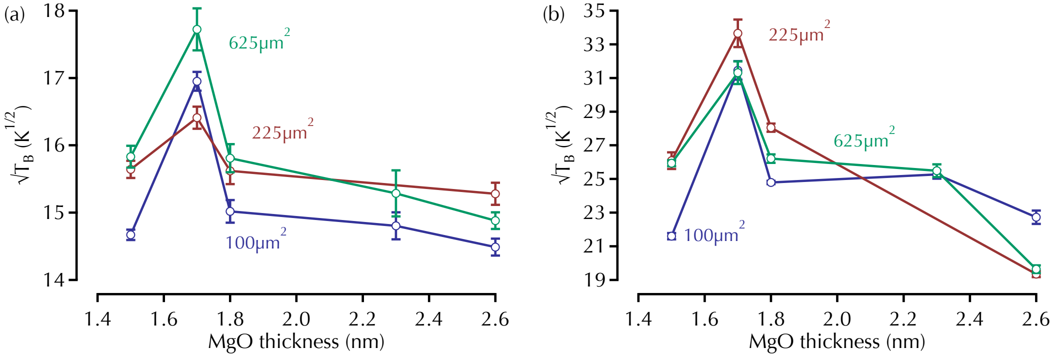

Figure 109: Dependence of $\sqrt{T_B}$ on the MgO barrier thickness for (a) 1 nm and (b) 1.2 nm Co-Fe-B. The element sizes were 100 µm$^2$ (blue), 225 µm$^2$ (red), and 625 µm$^2$ (green).

ues for the sample with 1.5 nm MgO barrier are shown in Table 19. The designation of soft and hard electrode refers to the magnetic state at 300 K. The calculated values of $T_B$ for the soft electrode is 213.35 K and for the hard electrode it is 422.69 K. These results fit in well with the experimentally obtained data for $T_B^{\text{soft}}$, whereas the superparamagnetic state of the hard electrode was not reached at 330 K. At around 200 K the major loop revealed an *s*-shape, due to the upcoming superparamagnetic regime of the 1 nm thick electrode.

The other samples with a different MgO barrier thickness $d_{\text{MgO}}$ show an analogous temperature dependence of the TMR effect. However, the $\vec{H}_c$ crossover temperature $T_\chi$ and the blocking temperature $T_B$ vary with $d_{\text{MgO}}$. Figure 109 illustrates the $T_B^{1/2}$ dependence of both Co-Fe-B electrodes on the barrier thick-

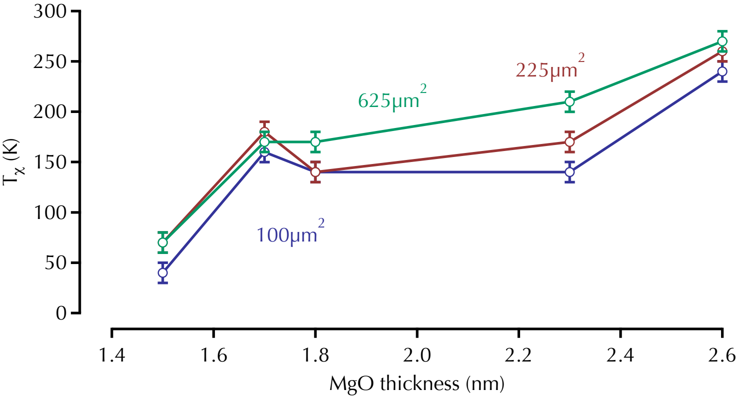

Figure 110: $T_\chi$ depending on the MgO barrier thickness for different element sizes, 100 µm$^2$ (blue), 225 µm$^2$ (red), and 625 µm$^2$ (green).

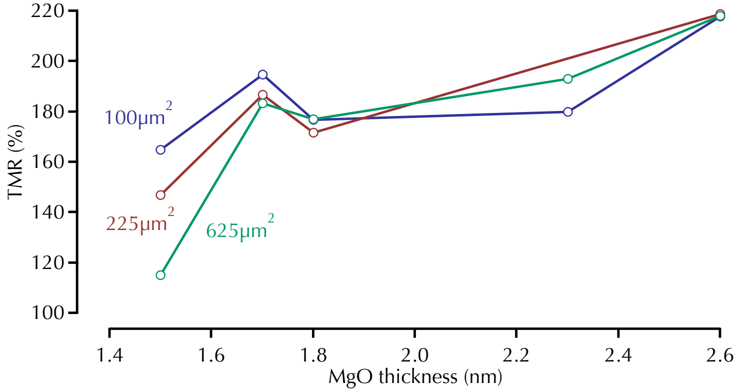

Figure 111: TMR effect at 20 K depending on the MgO barrier thickness for different element sizes, 100 µm$^2$ (blue), 225 µm$^2$ (red), and 625 µm$^2$ (green).

ness. In contrast to the bottom electrode, the coercive field of the top electrode correlates well with the Stoner-Wohlfarth behavior. Nonetheless, a clear correlation between $T_B$, $d_{\mathrm{MgO}}$, and the element size is not observable, independently of the electrode.

The dependence of $T_\chi$ on $d_{\mathrm{MgO}}$ is shown in Figure 110 for different element sizes. Again a clear correlation between the temperature and MgO thickness is not present. The MTJ's with a 1.7 nm barrier show a higher $T_B$ and $T_\chi$ compared to the samples with 1.6 nm and 1.8 nm. After the decrease of $T_\chi$ for the MTJ's with a 1.8 nm tunnel barrier, an increase is observed for the other film thicknesses. The highest $T_\chi$ is found for the samples with 2.6 nm MgO barrier. However, the sample shows no clear distinction between $T_\chi$ and $T_B$. Therefore, the coercive field crossover and superparamagnetic state merge into each other without visible transition.

Interestingly, the TMR effect at 20 K as a function of the MgO thickness shows the same dependence as $T_B$ and $T_\chi$ (cf. Figure 111). The sample with a 1.7 nm barrier reveals the highest TMR effect when compared to the samples with 1.6 nm and 1.8 nm MgO layer thickness. For a barrier thickness of 2.3 nm and 2.6 nm the TMR ratio increases and shows its maximum value for the thickest barrier. Because of the missing MgO barrier thicknesses between 1.9 nm and 2.2 nm and the high step size, an oscillatory behavior of the TMR effect could not be observed.[242]

[242] S. Yuasa et al. In: *Nature Materials* 3.12 (2004)

## *Bias voltage dependence*

The previous chapter revealed two interesting effects that depend on the temperature, the coercive field crossover and the superparamagnetic state. The coercive field crossover is based on differences in temperature dependence of the two Co-Fe-B electrodes. As previously mentioned, the coercive field can be modified by an external $\vec{E}$-field. With a high bias voltage $U_b$ a homogeneous electric field $\vec{E} = U_b/d_{\mathrm{MgO}}$ is induced. In that way, charge carrier accumulation takes place at one barrier interface and depletion at the other barrier interface. Differences in charge carrier density result in a variation of $\vec{H}_c$.[243] Figure 112 illustrates the temperature dependence of the TMR effect obtained at 700 mV for an MTJ with a 1.5 nm thick MgO barrier. The investigated element sizes were 100 $\mu$m$^2$, 225 $\mu$m$^2$ and 625 $\mu$m$^2$. A quick reminder: the TMR effect at $U_b = 10$ mV showed a decay between 30 K and 50 K for a junction size of 100 $\mu$m$^2$, for larger junctions the decay took place between 50 K and 70 K (225 $\mu$m$^2$) and 40 K and 120 K (625 $\mu$m$^2$) (cf. Figure 104). By applying a higher bias voltage the coercive field crossover is suppressed, as seen in Figure 112, for a junction size of 100 $\mu$m$^2$ and 225 $\mu$m$^2$. Figure 113 (a) illustrates the major loop at 40 K for $U_b = 10$ mV. To overcome the crossing of $\vec{H}_c$ a higher bias voltage of 700 mV was applied and a TMR effect is obtained (cf. Figure 113 (b)). It has to be mentioned that for all MgO barrier thicknesses a high bias voltage leads to a TMR effect during $T_\chi$. For the following discussion we will only take a look at the tunnel junctions with a 100 $\mu$m$^2$ area.

Figure 114 illustrates the $U_b$ dependence of the TMR effect

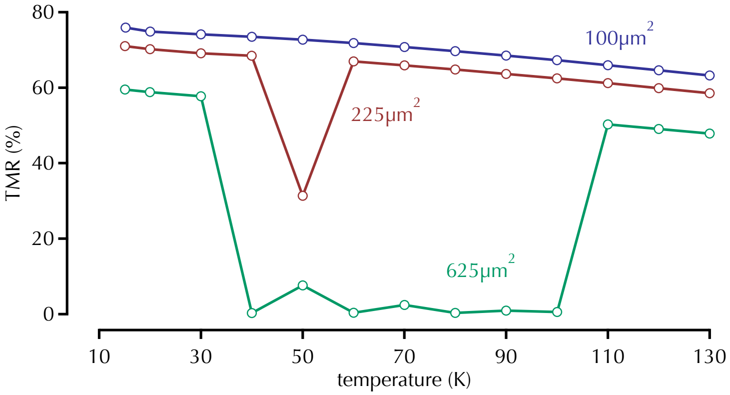

Figure 112: TMR effect depending on the temperature for $U_b = 700$ mV. The MTJ's have different areas: 100 $\mu$m$^2$ (blue), 225 $\mu$m$^2$ (red), and 625 $\mu$m$^2$ (green).

[243] This effect is yet not well understood.

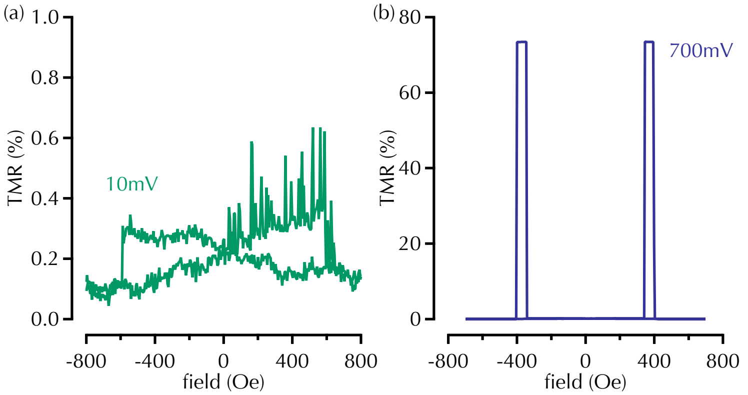

Figure 113: TMR effect obtained at 40 K for a bias voltage of (a) 10 mV (green) and (b) 700 mV (blue). The element area was 100 µm$^2$ and the barrier thickness 1.5 nm.

and the coercive field for an MTJ with a 1.5 nm MgO barrier. The sample temperature was set to 20 K and 100 K. The maximum TMR effect is observed for the low bias values ±10 mV at 20 K and 100 K. With increasing $|U_b|$ the TMR effect decreases. The slightly asymmetrical $U_b$-dependence of the TMR effect is typical and probably based on the differences between the Co-Fe-B electrodes.[244] Apart from the TMR ratio, we investigated the $\vec{H}_c$ dependence on the bias voltage (cf. Figure 114 (b)). The sample temperature was 100 K and thus the 1.2 nm thick Co-Fe-B layer was the hard-magnetic electrode. Between 10 mV and 100 mV the $\vec{H}_c$ drops drastically and remains almost constant with increasing $U_b$ for the 1 nm electrode. The 1.2 nm thick electrode shows an increasing $\vec{H}_c$ with increasing $U_b$ after the drop at 100 mV.

[244] D. D. Djayaprawira et al. In: *Applied Physics Letters* 86.9 (2005)

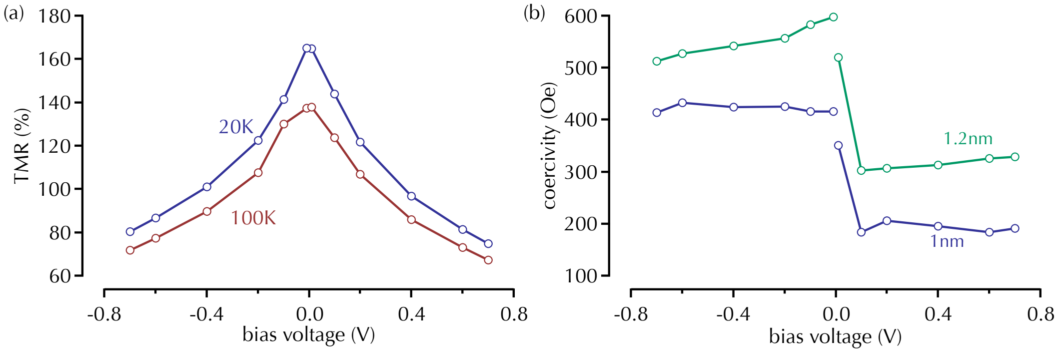

Figure 114: (a) TMR effect as a function of $U_b$ at 20 K (blue) and 100 K (red). (b) $\vec{H}_c$ depending on $U_b$ for the 1.2 nm (green) and the 1 nm (blue) thick Co-Fe-B electrode at 100 K. The MgO barrier of the MTJ was 1.5 nm.

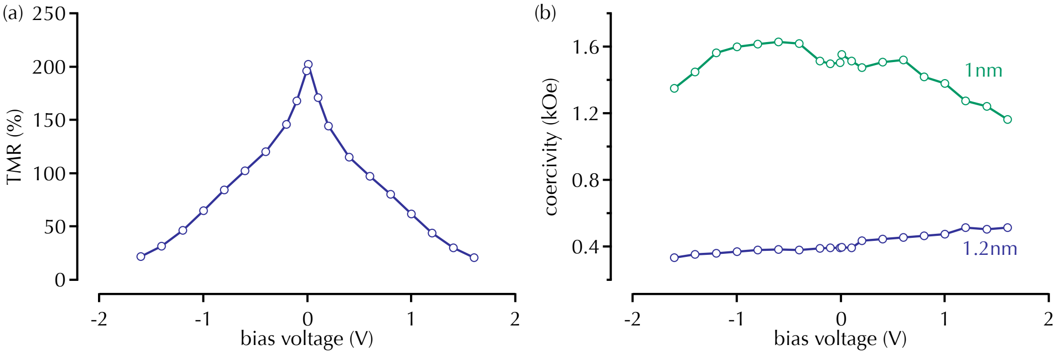

Figure 115: (a) TMR effect as a function of $U_b$ at 20 K. (b) $\vec{H}_c$ depending on $U_b$ for the 1 nm (green) and the 1.2 nm (blue) thick Co-Fe-B electrodes at 20 K. The MgO barrier of the MTJ was 1.7 nm.

However, the $\vec{H}_c$ of the hard-magnetic electrode decreases with increasing negative bias voltages, whereas the soft-magnetic electrode shows a poor increase of $\vec{H}_c$. By comparing the obtained results with the literature data an inconsistency was found. Wang et al. reported a different bias voltage dependence of the coercivity. The soft electrode shows a marginal increase of $\vec{H}_c$ between $-0.8\,\mathrm{V\,nm^{-1}}$ and $0\,\mathrm{V\,nm^{-1}}$ and for positive $\vec{E}$-fields a strong increase of the coercive field. However, the hard electrode shows a slight decrease of $\vec{H}_c$ between $-0.8\,\mathrm{V\,nm^{-1}}$ and $0.8\,\mathrm{V\,nm^{-1}}$.[245] A possible reason for the discrepancy in the behavior of our sample could be heating or tension.

Figure 115 depicts the TMR and $\vec{H}_c$ dependence on $U_b$. This sample exhibit an MgO barrier of 1.7 nm. The temperature was set to 20 K. The TMR effect shows the same dependence on $U_b$ as the previous sample with a 1.5 nm MgO barrier. The coercive field dependency on $U_b$ almost shows the behavior reported by Wang et al.[246] The hard electrode (1 nm Co-Fe-B thin film) shows a decreasing $\vec{H}_c$ with increasing $+U_b$, whereas the soft electrode shows an increasing $\vec{H}_c$ with increasing $+U_b$. The coercive field of the 1.2 nm electrode reveals a decrease with increasing $-U_b$. The 1.2 nm electrode exhibits increasing coercivity for $U_b \geq -600\,\mathrm{mV}$ and a decreasing coercive field for $U_b < -600\,\mathrm{mV}$. The only difference compared to the sample with a 1.5 nm MgO barrier is that the bottom (top) layer is the hard (soft) electrode.

[245] W. G. Wang et al. In: *Nature Materials* 11.1 (2011)

[246] W. G. Wang et al. In: *Nature Materials* 11.1 (2011)

## $\vec{E}$-field-assisted magnetization switching

In the previous section, the effect of an external $\vec{E}$-field on the PMA of thin Co-Fe-B films was discussed. As already mentioned in the introduction, the interplay of $\vec{H}_c$ and $\vec{E}$ results in a low critical current density $\vec{j}_c$ for STT switching. For this reason, we investigated apparently current-induced electrode switching in an MTJ with 1.5 nm MgO barrier thickness. In Figure 116 (a) the $I(U)$ dependence during transition from the parallel into the antiparallel magnetization state of that MTJ is shown. The sample temperature was set to 20 K. The switching procedure was as follows: after the sample was saturated with a high positive field ($\vec{H}_{\text{ext}} > 1.5\,\text{kOe}$), we applied a negative $\vec{H}$-field of $\vec{H}_b = -660\,\text{Oe}$, which is close to the $\vec{H}_c$ of the soft electrode. In this way, the parallel magnetization state of the top and bottom electrodes is conserved. By applying a negative bias voltage the coercivity of the soft electrode decreased (cf. Figure 117). In combination with the bias magnetic field, the direction of the soft electrode changed and an antiparallel magnetization state was achieved. The necessary bias voltage is around −190 mV (cf. Figure 116 (a) and 116 (b)). The antiparallel state is stable, even without an external magnetic field. However, by applying a positive bias voltage of $U_b = 690\,\text{mV}$ a collapse of the coercive fields is achieved (cf. Figure 117). The external magnetic field changed the direction of the hard-magnetic electrode and thus a parallel state was obtained. The values determined for $\vec{j}_c$ are around $10^4\,\text{A}\,\text{cm}^{-2}$ and therefore incredibly low. However, due to the combination of an $\vec{E}$- and $\vec{H}$-field, one has to emphasize that the switching is not

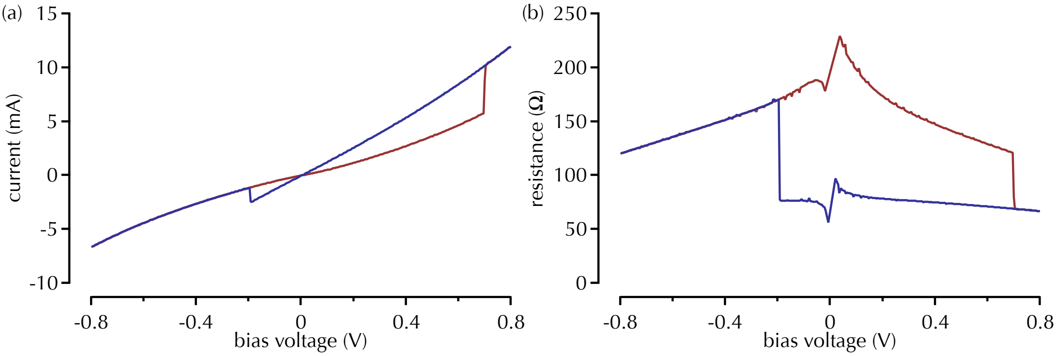

Figure 116: (a) $I(U)$ dependence during magnetization switching. (b) Resistance depending on $U_b$ during switching. The temperature was set to 20 K and the MgO thickness was 1.5 nm.

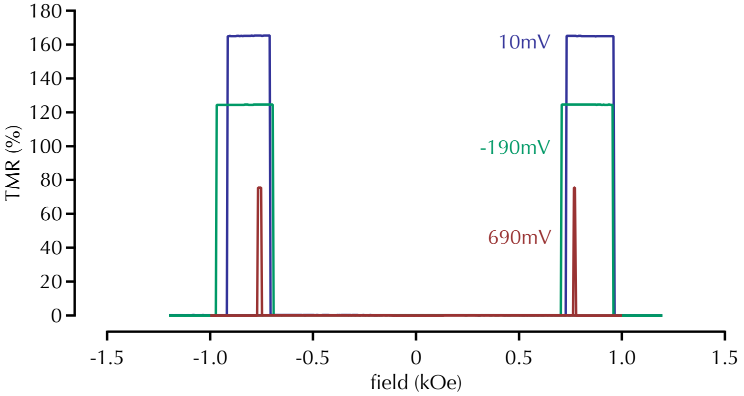

Figure 117: TMR effect at 20 K for different bias voltages 10 mV (blue), −190 mV (green), and 690 mV (red). The MgO thickness was 1.5 nm.

current-induced. Thus, the characterization of this effect by $\vec{j}_c$ is invalid. Nevertheless, several groups relate this switching mode to current-induced switching and therefore report incredibly low current densities.[247] However, the explanation that the $\vec{E}$-field lowers the energy barrier $E_B = \vec{M}_s \vec{H}_K V/2$ that has to be overcome to switch from one magnetization state into the other is vague (cf. Figure 96) because the additional bias magnetic field $\vec{H}_b$ that is necessary for the $\vec{E}$-field-assisted switching lowers the critical current density too (cf. Equation (52)). Therefore, we disregard the current density and focus on the critical electric field $\vec{E}_c$ necessary to switch the electrodes.

To investigate the dependence of $\vec{E}_c$ on $\vec{H}_b$, a 100 µm$^2$ large MTJ with a 1.7 nm MgO barrier was cooled down to 120 K. At this temperature, the 1 nm Co-Fe-B layer acts as a hard-magnetic electrode and the superparamagnetic state is avoided. The obtained TMR curve shows a distinct antiparallel state and the coercive fields are $\bar{H}_c^{\text{soft}} = 355(5)$ Oe and $\bar{H}_c^{\text{hard}} = 420(5)$ Oe (cf. Figure 118).[248] The TMR curve shows a shift of 20 Oe, probably induced by dipolar coupling or orange peel coupling of the electrodes. Furthermore, incorrect calibration of the applied magnetic field should not be neglected. Now we performed various $\vec{E}$-field-assisted $\vec{H}$-field switchings for different $\pm\vec{H}_b$. The obtained critical $\vec{E}$-field as a function of $\vec{H}_b$ is illustrated in Figure 119. Let us first take a look at the $P \rightarrow AP$ transition. Here, an increasing $\vec{E}_c$ with decreasing $\vec{H}_b$ is determined. This relation between $\vec{H}_b$ and $\vec{E}_c$ was expected. The transition from $AP \rightarrow P$ shows the same behavior. The smaller the applied $\vec{H}_b$ the higher the required $\vec{E}_c$ to decrease the coercive field. In addition, the necessary $\vec{H}_b$ and $\vec{E}_c$ are higher for $AP \rightarrow P$

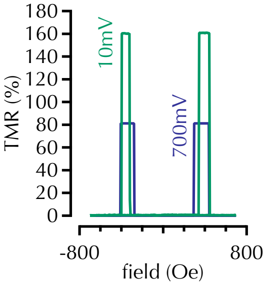

Figure 118: TMR effect at 10 mV (green) and 700 mV (blue). The MTJ consist of a 1.7 nm thick MgO barrier at 120 K and the element size was 100 µm$^2$.

[247] W. G. Wang et al. In: *Nature Materials* 11.1 (2011); W. G. Wang and C. L. Chien. In: *Journal of Physics D: Applied Physics* 46.7 (2013)

[248] $\bar{H}_c = \frac{|H_c^{\text{neg}}+H_c^{\text{pos}}|}{2}$

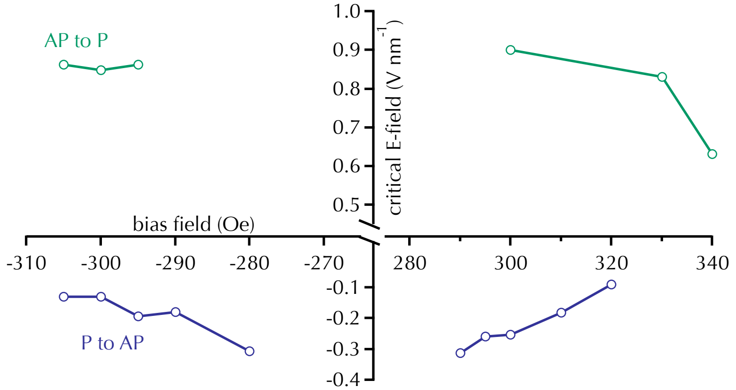

Figure 119: $\vec{E}_c$ as a function of $\vec{H}_b$ for the *AP* to *P* (green) and *P* to *AP* (blue) transition. The temperature was set to 120 K and the element size was 100 µm$^2$. The MgO thickness was 1.7 nm.

switching compared to $P \rightarrow AP$ switching. The reason for that behavior is simple and based on the obviously higher coercive field of the hard electrode. Therefore, a higher $\vec{E}_c$ is needed to induce a collapse of the coercivity of both electrodes. For pure current-induced magnetization switching a marginally higher $\vec{j}_c$ is required to switch from $P \rightarrow AP$.[249]

In a last attempt, we investigated the temperature dependence of the $\vec{E}$-field-assisted, $\vec{H}$-field-induced switching procedure from $P \rightarrow AP$. The determined critical $\vec{E}$-field was constant at all temperatures (cf. Figure 120). However, the bias magnetic field has to increase with decreasing temperatures due to the temperature

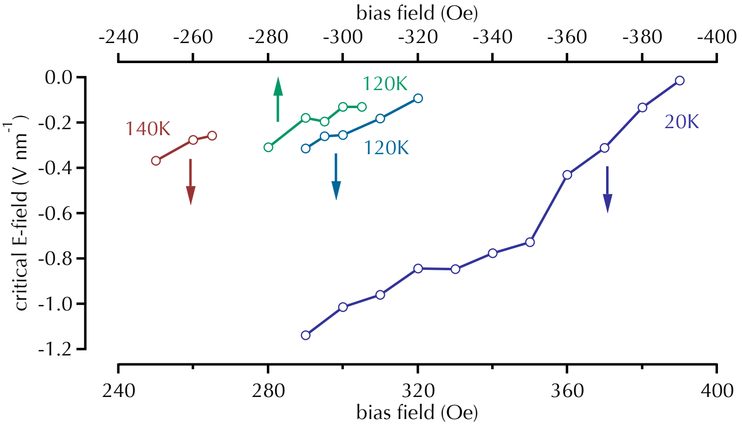

Figure 120: $\vec{E}_c$ depending on $\pm\vec{H}_b$ at various temperatures. The barrier thickness of the MTJ was 1.7 nm.

---

[249] H. Meng et al. In: *Journal of Physics D: Applied Physics* 44.40 (2011); S. Ikeda et al. In: *Nature Materials* 9.9 (2010)

dependence of $\vec{H}_c$. At 20 K only a transition from the parallel into the antiparallel state was observed. A transition from $AP \rightarrow P$ was not possible due to the large $\Delta\vec{H}_c = \vec{H}_c^{\text{hard}} - \vec{H}_c^{\text{soft}}$ that has to be overcome. In contrast to the MTJ with 1.5 nm MgO that exhibits a $\Delta\vec{H}_c$ of 157(5) Oe at 20 K, the $\Delta\vec{H}_c$ of the 1.7 nm MgO sample is $\Delta\vec{H}_c = 897(10)$ Oe.Thus a collapse of the coercive fields could not be induced by the applied $\vec{E}$-field without breaking the element. The lower $\Delta\vec{H}_c$ of the 1.5 nm MgO sample is due to the upcoming coercive field crossover of the electrodes at around 40 K. Therefore, we found a limitation on the variation of the coercive field via $\vec{E}$-field. In addition, we observed that the critical field $\vec{E}_c$ is independent of the sample temperature and of the MgO barrier thickness. These two characteristics are the main difference compared to the current-induced STT switching. Nonetheless, to obtain $\vec{E}$-field switching an external magnetic field is required that reduces the applicability of this switching mechanism in MRAM devices.

In the future, maybe the external magnetic field $\vec{H}_b$ could be replaced by a field-like current $\vec{I}_b$, as used for STT switching. In that way, $\vec{E}$-field-assisted STT-induced switching could be obtained.[250] As already mentioned above, Kanai et al.[251] reported a combination of STT switching and $\vec{E}$-field-induced switching. Additionally, a bias field $\vec{H}_b$ was used to compensate the dipolar coupling of the electrodes. The critical current density was still in the order of $10^6\ \mathrm{A\,cm^{-2}}$, but the switching time was only a few nanoseconds. However, new attempts have to be made in this field.

[250] J. G. Alzate et al. In: *IEEE International Electron Devices Meeting* (2012)

[251] S. Kanai et al. In: *Applied Physics Letters* 104.21 (2014)

## *Conclusion*

To summarize this chapter, we investigated $Co_{40}Fe_{40}B_{20}$ based pMTJ's. First, we analyzed the temperature dependent transport properties of pMTJ's with different MgO thicknesses. During cooling we found a decay in the TMR effect, due to a coercive field crossover of the electrodes. Around room temperature a transition from the ferromagnetic into the superparamagnetic state was found. There was no obvious dependence of the blocking temperature and crossover temperature on the MgO barrier thickness.

The bias voltage dependence of the TMR effect revealed an influence of the induced $\vec{E}$-field on the PMA of the samples. During the $\vec{H}_c$ crossover regime the TMR effect decreases due to the absence of an antiparallel state of the electrodes. By increasing the bias voltage an accumulation (depletion) of electrons at the barrier interface could be achieved. In that way, a lower (higher) coercive field of the electrode was obtained. The variation of the coercivity led to a stable antiparallel state of the electrodes and thus to a TMR effect.

The $\vec{E}$-field effect was used to switch the magnetization directions of the electrodes. Therefore, we used an $\vec{E}$-field to increase (decrease) the coercive field of the electrodes and a bias magnetic field that switches the electrodes. With this switching mechanism, incredibly low switching current densities were achieved. However, one has to keep in mind that this effect is not a current-induced switching effect. Therefore, we focused on the critical electric field necessary to switch the electrodes. The critical electric field showed no dependence on the temperature or barrier thickness, but on the bias magnetic field. If the bias magnetic field was close to the coercive field of the soft electrode a lower critical electric field was required for switching. However, with decreasing bias magnetic field the critical electric field increased. This $\vec{E}$-field-induced magnetization switching is an alternative to the already known STT switching. Unfortunately, $\vec{E}$-field switching requires a bias magnetic field to determine the magnetization direction of the electrodes. Therefore, the previous obstacle of a bias magnetic field still remains.

# *Summary and outlook*

We investigated different tetragonally distorted Mn-based Heusler compounds. We achieved highly crystalline thin films in the preferred (001) growth direction. The highest thin film quality with regard to surface roughness and crystallinity was found for layers on a $SrTiO_3$ substrate. Samples on MgO substrate also provide crystalline growth but with a tendency towards island growth. An optimum deposition temperature in terms of surface roughness and crystallinity was determined between 500 °C and 595 °C depending on the Heusler compound.

At the beginning, we prepared $Mn_{3\text{-}x}Ga$ thin films with different compositions on MgO and $SrTiO_3$ substrates. We gained insight into the surface, crystallographic, magnetic, and chemical properties. The $Mn_{3\text{-}x}Ga$ layers were sputtered from Mn-Ga composite targets and in certain cases in combination with an additional Mn target. The highest crystalline order was achieved for thin films prepared from a composite target without additional Mn target. These samples also showed the lowest surface roughness. In addition to the low roughness, the formation of Mn–O at the barrier interface was suppressed to a minimum. A high anisotropy energy of $0.97(2) \times 10^6\,\mathrm{J\,m^{-3}}$ was determined for a $L1_0$-ordered $Mn_{1.5}Ga$ film on MgO via SQUID measurements. The theoretically predicted decreasing total magnetic moment with increasing Mn content was verified via XAS and XMCD measurements.

In order to suppress the oxidation of Mn and to overcome the lattice mismatch between the $Mn_{3\text{-}x}Ga$ and the MgO barrier a 1 nm $Co_{40}Fe_{40}B_{20}$ or $Co_2FeAl$ layer was inserted, respectively.[252] Both ferromagnetic layers reduced the amount of Mn–O. Furthermore, element-specific hysteresis loops pointed out a parallel alignment between the magnetization direction of the $Mn_{3\text{-}x}Ga$ and the respective ferromagnetic interlayers. In other words, a perpendicularly magnetized $Co_2FeAl$ or $Co_{40}Fe_{40}B_{20}$ thin film was achieved without a further post-annealing process.

[252] M. Glas et al. In: *Journal of Applied Physics* 114.18 (2013)

To investigate the transport properties, we integrated $L1_0$-ordered $Mn_{1.5}Ga$ thin films with ferromagnetic interlayers into MTJ's. Two different perpendicularly magnetized counter electrodes were used. In a first attempt, we used a $(Co/Pt)_{10}$ multilayer counter electrode with ten repetition of Co (0.6 nm) and Pt (1.8 nm). The achieved TMR ratios were rather low and the preparation was time-consuming due to the multilayer fabrication. Moreover, the PMA of the multilayers depends on the Co and Pt film thickness as well as on the number of repetitions. For this reason, we replaced the multilayer electrode by a single $Co_{40}Fe_{40}B_{20}$ thin film with PMA. In order to achieve an easy magnetization direction perpendicular to the film plane, an ex-situ post-annealing process was performed. The additional annealing process also increased the crystallinity of the MgO barrier. However, the obtained TMR ratios still remained low for Co-Fe-B and also for the $Co_2FeAl$ interlayer. Auger electron depth profiles revealed the diffusion of Ga to the barrier interface. Therefore, the main reason for the low TMR ratio was found.

Finally we investigated the influence of a TiN seed layer on the properties of $Mn_{3\text{-}x}Ga$.[253] The TiN layer exhibited good epitaxial growth on MgO and $SrTiO_3$ substrates. A superconducting state was obtained for samples deposited at 405 °C and 595 °C on MgO and $SrTiO_3$. However, the added $Mn_{2.5}Ga$ thin film on top of the TiN showed a multiphase structure, a combination of the cubic $D0_3$ and the tetragonal $D0_{22}$ phase. The magnetic characteristics revealed a higher magnetization for the $Mn_{2.5}Ga$ layer on MgO than on $SrTiO_3$. This difference was induced by the multiphase on MgO.

For the purpose of further compensation of the magnetic moments, we added Co to the $Mn_{3\text{-}x}Ga$ crystal to obtain a $Mn_{3\text{-}x}Co_xGa$ compound. For $x \geq 0.5$ a cubic phase with an in-plane magnetization direction and for $0 < x < 0.5$ the tetragonally distorted $D0_{22}$ structure was reported.[254] Here again, MgO and $SrTiO_3$ substrates were used due to the low lattice mismatch. We prepared in-plane magnetized $Mn_{2.3}Co_{0.7}Ga$ on MgO and $SrTiO_3$ and out-of-plane magnetized $Mn_{2.7}Co_{0.3}Ga$ on MgO and $SrTiO_3$. These samples were co-sputtered from a $Mn_{45}Ga_{55}$ target, a Mn target and a Co target. XRR scans revealed a high surface roughness that lowers the applicability in tunnel junctions. Furthermore, $D0_{22}$-ordered $Mn_{2.6}Co_{0.3}Ga$ thin films on MgO and $SrTiO_3$ were deposited from a $Mn_{60}Ga_{40}$, a Mn, and a Co target in order to reduce the power applied to the Mn and Co targets. These samples showed the highest crystalline order. The $Mn_{45}Ga_{55}$

---

[253] A. Niesen et al. In: *arXiv.org* (2015). eprint: `1510.06256v2`

[254] V. Alijani et al. In: *Applied Physics Letters* 99.22 (2011)

target led to lower crystalline growth on MgO and $SrTiO_3$ substrates. VSM measurements revealed a soft-magnetic character for the cubic compound. Element-specific hysteresis loops revealed a hard-magnetic character for $Mn_{2.7}Co_{0.3}Ga$ thin films on MgO and $SrTiO_3$. Furthermore, the obtained magnetization from SQUID measurements for a $Mn_{2.6}Co_{0.3}Ga$ layer on MgO was lower compared to the $Mn_{2.8}Ga$ thin film. Hence, the lower magnetic moment due to the further compensation was proved. XAS and XMCD measurements revealed ferromagnetic coupling of the Mn and Co moments for the cubic structure and antiferromagnetic coupling in the tetragonal phase. This example shows the tunability of Heusler compounds, which is the main reason for the wide range of possible applications of these compounds. Furthermore, we showed that the insertion of a ferromagnetic interlayer reduces the amount of Mn−O at the barrier interface.

By replacing the Ga in the $Mn_{3\text{-}x}Ga$ compound with Ge, we obtained $D0_{22}$-ordered $Mn_{3\pm x}Ge$ thin films with an easy axis perpendicular to the film plane. The samples were prepared by co-sputtering from a Mn and Ge target. The thin films were deposited on (001) $SrTiO_3$ substrates at 450 °C and 550 °C. We investigated the crystalline and magnetic properties as well as the surface roughness of $Mn_{3\pm x}Ge$ thin films. We achieved crystalline growth in the (001) direction for different $Mn_{3+x}Ge$ compositions ($x = -0.3$, 0.2 and 0.6) on $SrTiO_3$ substrates. The magnetic properties were examined via AHE measurements and exhibited a coercive field of 3.25 T for the $Mn_{3.2}Ge$ compound. This is the highest coercivity of the Mn-based Heusler compounds investigated in this work. However, the $Mn_{3\pm x}Ge$ surface roughness was too high for integration into MTJ's.

Besides the investigation of new materials, we examined commonly known ferromagnetic $Co_{40}Fe_{40}B_{20}$ thin films with PMA. We prepared Co-Fe-B based pMTJ's and analyzed the magnetic and transport properties between 15 K and 330 K. Around RT a superparamagnetic state was found that drastically reduces the applicability of Co-Fe-B-based MRAM devices. The superparamagnetic state occurs due to the low nominal film thickness. The temperature dependent measurements showed a coercive field crossover of the two Co-Fe-B electrodes. The temperature regime of the crossover varied with MgO thickness. A dependence of the TMR effect and the coercive field on the bias voltage $U_b$ was found. The TMR ratio decreases with increasing $U_b$.[255] However, the coercive field increases or decreases according to the polarity of the voltage. In this way, we caused a temporary

[255] S. Zhang et al. In: *Physical Review Letters* 79.19 (1997)

decrease of the anisotropy energy. This effect was used in an $\vec{E}$-field-assisted $\vec{H}$-field-induced switching mechanism. The critical $\vec{E}$-field required for switching was independent of the MgO barrier thickness and the sample temperature. Only the $\vec{H}_b$-field needed to be adjusted, due to the temperature dependence of $\vec{H}_c$. This is a notable difference between EAMS ($\vec{E}$-field-assisted magnetization switching) and CIMS (current-induced magnetization switching). However, the requirement of a magnetic field reduces the applicability of EAMS in MRAM devices. For this reason, we propose a new switching method, where the external magnetic field is replaced by a spin-polarized current. In this case, the $\vec{E}$-field reduces the PMA and the current switches the electrodes.

This work showed that the preparation of new tetragonally distorted Heusler compounds with PMA provides a lot of obstacles. Even though the theoretically predicted properties were proved experimentally, integration into MTJ's did not lead to the theoretically expected TMR effects. The high oxygen affinity of Mn and the diffusion of Ga are drawbacks that have to be overcome. Another challenge is the surface roughness that needs to be minimized, i.e., below 1 nm to fulfill the requirements for STT switching. The reported TMR ratios for the Mn-based compounds are rather low and only showed adequate results when used in combination with a ferromagnetic interlayer. Most likely, this pinning effect between the ferrimagnet and the ferromagnet is promising for future applications. Ferromagnetic thin films like Co-Fe-B showed an upcoming superparamagnetic state for temperatures around and/or above RT. In combination with a hard-magnetic layer, this obstacle could be overcome. Nonetheless, the above-named Heusler compounds showed a lot of interesting properties and opened the path for other Mn-based compounds, such as Mn-Fe-Ga or Mn-Pt-Ga.[256]

In a nutshell, new materials for spintronic devices are required due to the constant miniaturization process. The competitors, like DRAM or SRAM, captivate by an easy preparation method and an incredibly low half-pitch size. Very recently, Intel and Samsung announced the serial production of DRAM chips with a half-pitch size of 14 nm.[257] Nevertheless, for the future STT-MRAM is sure to be the only candidate to replace DRAM and SRAM, due to its high endurance. However, to lower the critical current density for STT-MRAM one should also search for new effects, like the EAMS. In my opinion, a combination of both, a new material with high anisotropy and an $\vec{E}$-field supported

[256] C. Felser et al. In: *IEEE Transactions on Magnetics* 49 (2013); J. Winterlik et al. In: *Advanced Materials* 24.47 (2012)

[257] http://www.intel.com/content/www/us/en/silicon-innovations/intel-14nm-technology.html

STT switching process, appears to be the best solution for future storage devices.

# *Publications and conferences*

## *Publications*

1. M. Meinert, J.-M. Schmalhorst, **M. Glas**, G. Reiss, Elke Arenholz, Tim Böhnert, and Kornelius Nielsch (2012). *Insights into the electronic structure of $Co_2FeSi$ from x-ray magnetic linear dichroism.* Physical Review B, 86(5), 054420.

2. **M. Glas**, D. Ebke, I.-M. Imort, P. Thomas, and G. Reiss. (2013). *Anomalous Hall effect in perpendicularly magnetized $Mn_{3\text{-}x}Ga$ thin films.* Journal of Magnetism and Magnetic Materials, 333, 134-137.

3. **M. Glas**, C. Sterwerf, J.-M. Schmalhorst, D. Ebke, C. Jenkins, E. Arenholz, and G. Reiss (2013). *X-ray absorption spectroscopy and magnetic circular dichroism studies of $L1_0$-Mn-Ga thin films.* Journal of Applied Physics, 114(18), 183910.

4. A. Niesen, **M. Glas**, J. Ludwig, R. Sahoo, D. Ebke, E. Arenholz, J.-M. Schmalhorst, and G. Reiss (2013). *Titanium Nitride as a Seed Layer for Heusler Compounds.* arXiv:1510.06256.

## *Conferences*

1. M. Glas, D. Ebke, C. Sterwerf, M. Meinert, J.-M. Schmalhorst, C. Jenkins, E. Arenholz and G. Reiss, *$Mn_{3\text{-}x}Ga$ based magnetic tunnel junctions with perpendicular magnetic anisotropy*, DPG spring meeting, Regensburg (2013), MA 25.4

2. M. Glas, D. Ebke, K. Rott, E. Schellenberg, J.-M. Schmalhorst and G. Reiss, *Perpendicularly magnetized $L1_0$-Mn-Ga thin films in magnetic tunnel junctions*, DPG spring meeting, Dresden (2014), MA 10.5

3. M. Glas, K. Rott, L. Stockfisch, A. Gebauer, D. Ebke, J.-M. Schmalhorst, and G. Reiss, *MgO barrier dependent superparamagnetic state in CoFeB magnetic tunnel junctions*, InterMAG, Dresden (2014), HQ-11

4. M. Glas, K. Rott, L. Stockfisch, A. Gebauer, D. Ebke, J.-M. Schmalhorst, and G. Reiss, *Electric-field-induced electrode switching in CoFeB based perpendicular magnetic tunnel junctions*, MMM, Hawaii (2014), FS-06

5. M. Glas, D. Ebke, and G. Reiss, *Preparation and characterization of perpendicularly magnetized* $Mn_{3\pm x}Ge$ *thin films*, DPG spring meeting, Berlin (2015), MA 49.26

# *Bibliography*

Aguilar, M. and F. Agulló-López. "X-ray induced processes in $SrTiO_3$". In: *Journal of Applied Physics* 53.12 (1982).

Akinaga, H., T. Manago, and M. Shirai. "Material Design of Half-Metallic Zinc-Blende CrAs and the Synthesis by Molecular-Beam Epitaxy". In: *Japanese Journal of Applied Physics* 39.11B (2000).

Alijani, V., J. Winterlik, G. H. Fecher, and C. Felser. "Tuning the magnetism of the Heusler alloys $Mn_{3-x}Co_xGa$ from soft and half-metallic to hard-magnetic for spin-transfer torque applications". In: *Applied Physics Letters* 99.22 (2011).

Alzate, J. G., P. K. Amiri, P. Upadhyaya, S. S. Cherepov, J. Zhu, M. Lewis, R. Dorrance, J. A. Katine, J. Langer, K. Galatsis, D. Markovic, I. Krivorotov, and K. L. Wang. "Voltage-induced switching of nanoscale magnetic tunnel junctions". In: *IEEE International Electron Devices Meeting* (2012).

Arras, E., D. Caliste, T. Deutsch, F. Lançon, and P. Pochet. "Phase diagram, structure, and magnetic properties of the Ge-Mn system: A first-principles study". In: *Physical Review B* 83.17 (2011).

Ashcroft, N. W. and N. D. Mermin. *Solid state physics*. Brooks/Cole, Thomson Learning, 2005.

Baibich, M. N., J. M. Broto, A. Fert, F. Nguyen Van Dau, F. Petroff, P. Etienne, G. Creuzet, A. Friederich, and J. Chazelas. "Giant Magnetoresistance of (001) Fe/(001) Cr Magnetic Superlattices". In: *Phys. Rev. Lett.* 61 (21 1988).

Balke, B., G. H. Fecher, J. Winterlik, and C. Felser. "$Mn_3Ga$, a compensated ferrimagnet with high Curie temperature and low magnetic moment for spin torque transfer applications". In: *Applied Physics Letters* 90.15 (2007).

Bardeen, J., L. N. Cooper, and J. R. Schrieffer. "Theory of Superconductivity". In: *Physical Review* 108.5 (1957).

Bean, C. P. and J. D. Livingston. "Superparamagnetism". In: *Journal of Applied Physics* 30.4 (1959).

Berger, L. “Emission of spin waves by a magnetic multilayer traversed by a current”. In: *Physical Review B* 54.13 (1996).

— “Side-Jump Mechanism for the Hall Effect of Ferromagnets”. In: *Physical Review B* 2.11 (1970).

Binasch, G., P. Grünberg, F. Saurenbach, and W. Zinn. “Enhanced magnetoresistance in layered magnetic structures with antiferromagnetic interlayer exchange”. In: *Physical Review B* 39.7 (1989).

Bither, T. A. and W. H. Cloud. “Magnetic Tetragonal $\delta$-Phase in the Mn-Ga Binary”. In: *Journal of Applied Physics* 36.4 (1965).

Brataas, A., A. D. Kent, and H. Ohno. “Current-induced torques in magnetic materials”. In: *Nature Materials* 11.5 (2012).

Chae, K.-S., D.-Y. Lee, T.-H. Shim, J.-P. Hong, and J.-G. Park. “Correlation of the structural properties of a Pt seed layer with the perpendicular magnetic anisotropy features of full Heusler-based $Co_2FeAl$/ MgO/ $Co_2Fe_6B_2$ junctions via a 12-inch scale Si wafer process”. In: *Applied Physics Letters* 103.16 (2013).

Chen, C. T., Y. Idzerda, H. J. Lin, N. V. Smith, G. Meigs, E. Chaban, G. H. Ho, E. Pellegrin, and F. Sette. “Experimental Confirmation of the X-Ray Magnetic Circular-Dichroism Sum-Rules for Iron and Cobalt”. In: *Physical Review Letters* 75.1 (1995).

Coey, J. M. D. and M. Venkatesan. “Half-metallic ferromagnetism: Example of $CrO_2$ (invited)”. In: *Journal of Applied Physics* 91.10 (2002).

Cumings, J., L. Moore, H. Chou, K. Ku, G. Xiang, S. Crooker, N. Samarth, and D. Goldhaber-Gordon. “Tunable Anomalous Hall Effect in a Nonferromagnetic System”. In: *Physical Review Letters* 96.19 (2006).

Djayaprawira, D. D., K. Tsunekawa, M. Nagai, H. Maehara, S. Yamagata, N. Watanabe, S. Yuasa, Y. Suzuki, and K. Ando. “230% room-temperature magnetoresistance in CoFeB/ MgO/ CoFeB magnetic tunnel junctions”. In: *Applied Physics Letters* 86.9 (2005).

Drewello, V., J. Schmalhorst, A. Thomas, and G. Reiss. “Evidence for strong magnon contribution to the TMR temperature dependence in MgO based tunnel junctions”. In: *Physical Review B* 77.1 (2008).

Dürr, H. A., G. van der Laan, D. Spanke, F. U. Hillebrecht, and N. B. Brookes. “Electron-correlation-induced magnetic order of ultrathin Mn films”. In: *Physical Review B* 56.13 (1997).

Ebke, D., Z. Kugler, P. Thomas, O. Schebaum, M. Schäfers, D. Nissen, J. Schmalhorst, A. Hütten, E. Arenholz, and A. Thomas. “X-Ray Absorption and Magnetic Circular Dichroism Studies of $Co_2FeAl$ in Magnetic Tunnel Junctions". In: *IEEE Transactions on Magnetics* 46.6 (2010).

Endo, M., S. Kanai, S. Ikeda, F. Matsukura, and H. Ohno. "Electric-field effects on thickness dependent magnetic anisotropy of sputtered MgO/$Co_{40}Fe_{40}B_{20}$/Ta structures". In: *Applied Physics Letters* 96.21 (2010).

Felser, C., V. Alijani, J. Winterlik, and S. Chadov. "Tetragonal Heusler Compounds for Spintronics". In: *IEEE Transactions on Magnetics* 49 (2013).

Feng, W., D. Van Thiet, D. Dung, Y. Shin, and S. Cho. "Substrate-modified ferrimagnetism in MnGa films". In: *Journal of Applied Physics* 108.11 (2010).

Gallagher, W. J. and S. S. P. Parkin. "Development of the magnetic tunnel junction MRAM at IBM: From first junctions to a 16-Mb MRAM demonstrator chip". In: *IBM Journal of Research and Development* 50.1 (2006).

Gebauer, A. "Tunnelmagnetoresistance and electric-field-assisted switching in CoFeB/ MgO/ CoFeB magnetic tunnel junctions with perpendicular magnetization". Bachelor thesis. Bielefeld University, Faculty of Physics, 2014.

Glas, M. "Integration of $Mn_{3-x}Ga$ thin films into magnetic tunnel junctions". Diploma thesis. Bielefeld University, Faculty of Physics, 2012.

Glas, M., C. Sterwerf, J. Schmalhorst, D. Ebke, C. Jenkins, E. Arenholz, and G. Reiss. "X-ray absorption spectroscopy and magnetic circular dichroism studies of $L1_0$-Mn-Ga thin films". In: *Journal of Applied Physics* 114.18 (2013).

Groot, R. A. de, F. A. Mueller, P. G. van Engen, and K. H. J. Buschow. "New Class of Materials - Half-Metallic Ferromagnets". In: *Physical Review Letters* 50.25 (1983).

Hasegawa, M. and I. Tsuboya. "Magnetic Properties of eta Phase in Mn-Ga System". In: *Journal of the Physical Society of Japan* 20 (1965).

Huai, Y., F. Albert, P. Nguyen, and M. Pakala. "Observation of spin-transfer switching in deep submicron-sized and low-resistance magnetic tunnel junctions". In: *Applied Physics Letters* 84.16 (2004).

Ikeda, S., J. Hayakawa, Y. Ashizawa, Y. M. Lee, K. Miura, H. Hasegawa, M. Tsunoda, F. Matsukura, and H. Ohno. "Tunnel magnetoresistance of 604 % at 300 K by suppression of Ta diffusion in CoFeB/ MgO/ CoFeB pseudo-spin-valves annealed at high temperature". In: *Applied Physics Letters* 93.8 (2008).

Ikeda, S., K. Miura, H. Yamamoto, K. Mizunuma, H. D. Gan, M. Endo, S. Kanai, J. Hayakawa, F. Matsukura, and H. Ohno. "A perpendicular-anisotropy CoFeB/ MgO magnetic tunnel junction". In: *Nature Materials* 9.9 (2010).

Inoue, J. and S. Maekawa. "Effects of spin-flip and magnon-inelastic scattering on tunnel magnetoresistance". In: *Journal of Magnetism and Magnetic Materials* 198-199 (1999).

Jaklevic, R. C., J. Lambe, A. H. Silver, and J. E. Mercereau. "Quantum Interference Effects in Josephson Tunneling". In: *Physical Review Letters* 12.7 (1964).

Jesche, A., R. W. McCallum, S. Thimmaiah, J. L. Jacobs, V. Taufour, A. Kreyssig, R. S. Houk, S. L. Bud'ko, and P. C. Canfield. "Giant magnetic anisotropy and tunnelling of the magnetization in $Li_2(Li_{1-x}Fe_x)N$". In: *Nature Communications* 5 (2014).

Josephson, B. D. "Possible new effects in superconductive tunnelling". In: *Physics Letters* 1.7 (1962).

Jullière, M. "Tunneling Between Ferromagnetic-Films". In: *Physics Letters A* 54.3 (1975).

Li-Jun, Z., N. Shuai-Hua, and Z. Jian-Hua. "Recent progress in perpendicularly magnetized Mn-based binary alloy films". In: *Chinese Physics B* 22.11 (2013).

Kádár, G. and E. Krén. "Neutron Diffraction Study of $Mn_3Ga$". In: *International Journal Magnetism* 143.1 (1971).

Kamerlingh Onnes, H. "The resistance of pure mercury at helium temperatures". In: *Commun. Phys. Lab. Univ. Leiden* 12.120 (1911).

Kanai, S., Y. Nakatani, M. Yamanouchi, S. Ikeda, H. Sato, F. Matsukura, and H. Ohno. "Magnetization switching in a CoFeB/ MgO magnetic tunnel junction by combining spin-transfer torque and electric field-effect". In: *Applied Physics Letters* 104.21 (2014).

Karplus, R. and J. Luttinger. "Hall Effect in Ferromagnetics". In: *Physical Review* 95.5 (1954).

Kim, D., K. Y. Jung, S. Joo, Y. Jang, J. Hong, and B. C. Lee. "Perpendicular magnetization of CoFeB on top of an amorphous buffer layer". In: *Journal of Magnetism and Magnetic Materials* 375 (2015).

Köhler, A., I. Knez, D. Ebke, C. Felser, and S. S. P. Parkin. "Loss of anisotropy in strained ultrathin epitaxial $L1_0$ Mn-Ga films". In: *Applied Physics Letters* 103.16 (2013).

Krishnan, K. M. "Ferromagnetic $\delta$-$Mn_{1-x}Ga_x$ Thin-Films with Perpendicular Anisotropy". In: *Applied Physics Letters* 61.19 (1992).

Krockenberger, Y., S. Karimoto, H. Yamamoto, and K. Semba. "Coherent growth of superconducting TiN thin films by plasma enhanced molecular beam epitaxy". In: *Journal of Applied Physics* 112.8 (2012).

Kubota, T., Q. L. Ma, S. Mizukami, Z. Zhang, H. Naganuma, M. Oogane, Y. Ando, and T. Miyazaki. "Dependence of Tunnel Magnetoresistance Effect on Fe Thickness of Perpendicularly Magnetized $L1_0$-$Mn_{62}Ga_{38}$/Fe/MgO/CoFe Junctions". In: *Applied Physics Express* 5.4 (2012).

Kubota, T., S. Mizukami, Q. L. Ma, H. Naganuma, M. Oogane, Y. Ando, and T. Miyazaki. "Tunnel magnetoresistance effect using perpendicularly magnetized tetragonal and cubic Mn-Co-Ga Heusler alloy electrode". In: *Journal of Applied Physics* 115.17 (2014).

Kubota, T., S. Mizukami, D. Watanabe, F. Wu, X. Zhang, H. Naganuma, M. Oogane, Y. Ando, and T. Miyazaki. "Effect of metallic Mg insertion on the magnetoresistance effect in MgO-based tunnel junctions using $D0_{22}$-$Mn_{3-\delta}Ga$ perpendicularly magnetized spin polarizer". In: *Journal of Applied Physics* 110.1 (2011).

Kugler, Z., V. Drewello, M. Schäfers, J.-M. Schmalhorst, G. Reiss, and A. Thomas. "Temperature and bias voltage dependence of Co/Pd multilayer-based magnetic tunnel junctions with perpendicular magnetic anisotropy". In: *Journal of Magnetism and Magnetic Materials* 323.2 (2011).

Kugler, Z., J.-P. Grote, V. Drewello, O. Schebaum, G. Reiss, and A. Thomas. "Co/Pt multilayer-based magnetic tunnel junctions with perpendicular magnetic anisotropy". In: *Journal of Applied Physics* 111.7 (2012).

Kurt, H., N. Baadji, K. Rode, M. Venkatesan, P. Stamenov, S. Sanvito, and J. M. D. Coey. "Magnetic and electronic properties of $D0_{22}$-$Mn_3Ge$ (001) films". In: *Applied Physics Letters* 101.13 (2012).

Kurt, H., K. Rode, K. Oguz, M. Boese, C. C. Faulkner, and J. M. D. Coey. "Boron diffusion in magnetic tunnel junctions with MgO (001) barriers and CoFeB electrodes". In: *Applied Physics Letters* 96.26 (2010).

Kurt, H., K. Rode, M. Venkatesan, P. Stamenov, and J. M. D. Coey. "High spin polarization in epitaxial films of ferrimagnetic $Mn_3Ga$". In: *Physical Review B* 83.2 (2011).

Lee, D.-S., H.-T. Chang, C.-W. Cheng, and G. Chern. "Perpendicular Magnetic Anisotropy in MgO/ CoFeB/ Nb and a

Comparison of the Cap Layer Effect". In: *IEEE Transactions on Magnetics* 50.7 (2014).

Li, X. W., A. Gupta, G. Xiao, W. Qian, and V. P. Dravid. "Fabrication and properties of heteroepitaxial magnetite ($Fe_3O_4$) tunnel junctions". In: *Applied Physics Letters* 73.22 (1998).

Liu, G. D., X. F. Dai, H. Y. Liu, J. L. Chen, Y. X. Li, G. Xiao, and G. H. Wu. "$Mn_2CoZ$ (Z=Al, Ga, In, Si, Ge, Sn, Sb) compounds: Structural, electronic, and magnetic properties". In: *Physical Review B* 77.1 (2008).

Liu, T., Y. Zhang, J. W. Cai, and H. Y. Pan. "Thermally robust Mo/ CoFeB/ MgO trilayers with strong perpendicular magnetic anisotropy". In: *Scientific reports* 4 (2014).

Ma, Q. L., T. Kubota, S. Mizukami, X. M. Zhang, H. Naganuma, M. Oogane, Y. Ando, and T. Miyazaki. "Magnetoresistance effect in $L1_0$-MnGa/ MgO/ CoFeB perpendicular magnetic tunnel junctions with Co interlayer". In: *Applied Physics Letters* 101.3 (2012).

Ma, Q. L., S. Mizukami, T. Kubota, X. Zhang, A. Sugihara, H. Naganuma, M. Oogane, Y. Ando, and T. Miyazaki. "Tunneling magnetoresistance effect in MnGa based perpendicular magnetic tunnel junction with Fe/ Co interlayer". In: *Journal of Applied Physics* 114.16 (2013).

Maruyama, T., Y. Shiota, T. Nozaki, K. Ohta, and N. Toda. "Large voltage-induced magnetic anisotropy change in a few atomic layers of iron". In: *Nature* 4.3 (2009).

Meinert, M., J.-M. Schmalhorst, C. Klewe, G. Reiss, E. Arenholz, T. Böhnert, and K. Nielsch. "Itinerant and localized magnetic moments in ferrimagnetic $Mn_2CoGa$ thin films probed by x-ray magnetic linear dichroism: Experiment and ab initio theory". In: *Physical Review B* 84.13 (2011).

Meng, H., R. Sbiaa, S. Y. H. Lua, C. C. Wang, M. A. K Akhtar, S. K. Wong, P. Luo, C. J. P. Carlberg, and K. S. A. Ang. "Low current density induced spin-transfer torque switching in CoFeB/ MgO magnetic tunnel junctions with perpendicular anisotropy". In: *Journal of Physics D: Applied Physics* 44.40 (2011).

Miura, Y. and M. Shirai. "Theoretical Study on Tunneling Magnetoresistance of Magnetic Tunnel Junctions with $D0_{22}$-$Mn_3Z$ (Z=Ga,Ge)". In: *IEEE Transactions on Magnetics* 50.1 (2014).

Miyajima, H. "Simple analysis of torque measurement of magnetic thin films". In: *Journal of Applied Physics* 47.10 (1976).

Mizukami, S., A. Sakuma, A. Sugihara, T. Kubota, Y. Kondo, H. Tsuchiura, and T. Miyazaki. "Tetragonal $D0_{22}$ $Mn_{3+x}Ge$ Epitaxial Films Grown on MgO(100) with a Large Perpendicular Magnetic Anisotropy". In: *Applied Physics Express* 6.12 (2013).

Mizukami, S., F. Wu, A. Sakuma, J. Walowski, D. Watanabe, T. Kubota, X. Zhang, H. Naganuma, M. Oogane, Y. Ando, and T. Miyazaki. "Long-Lived Ultrafast Spin Precession in Manganese Alloys Films with a Large Perpendicular Magnetic Anisotropy". In: *Physical Review Letters* 106.11 (2011).

Monso, S., B. Rodmacq, S. Auffret, G. Casali, F. Fettar, B. Gilles, B. Dieny, and P. Boyer. "Crossover from in-plane to perpendicular anisotropy in Pt/ CoFe/ $\mathrm{AlO}_x$ sandwiches as a function of Al oxidation: A very accurate control of the oxidation of tunnel barriers". In: *Applied Physics Letters* 80.22 (2002).

Moodera, J. S., L. R. Kinder, T. M. Wong, and R. Meservey. "Large Magnetoresistance at Room-Temperature in Ferromagnetic Thin-Film Tunnel-Junctions". In: *Physical Review Letters* 74.16 (1995).

Moodera, J. S. and G. Mathon. "Spin polarized tunneling in ferromagnetic junctions". In: *Journal of Magnetism and Magnetic Materials* 200 (1999).

Niesen, A., M. Glas, J. Ludwig, R. Sahoo, D. Ebke, E. Arenholz, J. Schmalhorst, and G. Reiss. "Titanium Nitride as a Seed Layer for Heusler Compounds". In: *arXiv.org* (2015). eprint: `1510.06256v2`.

Niida, H., T. Hori, and Y. Nakagawa. "Magnetic-Properties and Crystal Distortion of Hexagonal $\mathrm{Mn_3Ga}$". In: *Journal of the Physical Society of Japan* 52.5 (1983).

Niida, H., T. Hori, H. Onodera, Y. Yamaguchi, and Y. Nakagawa. "Magnetization and coercivity of $\mathrm{Mn}_{3-\delta}\mathrm{Ga}$ alloys with a $\mathrm{D0}_{22}$-type structure". In: *Journal of Applied Physics* 79.8 (1996).

Nozaki, T., Y. Shiota, M. Shiraishi, and T. Shinjo. "Voltage-induced perpendicular magnetic anisotropy change in magnetic tunnel junctions". In: *Applied Physics Letters* 96.2 (2010).

Nunes, W. C., W. S. D. Folly, J. P. Sinnecker, and M. A. Novak. "Temperature dependence of the coercive field in single-domain particle systems". In: *Physical Review B* 70.1 (2004).

Ohno, H., D. Chiba, F. Matsukura, T. Omiya, T. Abe E .and Dietl, Y. Ohno, and K. Ohtani. "Electric-field control of ferromagnetism". In: *Nature* 408.6815 (2000).

Ohoyama, T. "X-ray and Magnetic Studies of the Manganese-Germanium System". In: *Journal of the Physical Society of Japan* 16.10 (2013).

Ouardi, S., T. Kubota, G. H. Fecher, R. Stinshoff, S. Mizukami, T. Miyazaki, E. Ikenaga, and C. Felser. "Stoichiometry dependent phase transition in Mn-Co-Ga-based thin films: From cubic in-plane, soft magnetized to tetragonal perpendicular, hard magnetized". In: *Applied Physics Letters* 101.24 (2012).

Parkin, S. S. P., C. Kaiser, A. Panchula, P. M. Rice, B. Hughes, M. Samant, and S.-H. Yang. "Giant tunnelling magnetoresistance at room temperature with MgO (100) tunnel barriers". In: *Nature Materials* 3.12 (2004).

Parratt, L. "Surface Studies of Solids by Total Reflection of X-Rays". In: *Physical Review* 95.2 (1954).

Pauw, L. J. van der. "A method of measuring specific resistivity and Hall effect of discs of arbitrary shape". In: *Philips Research Reports* 13.1 (1958).

Pickett, W. E. and J. S. Moodera. "Half Metallic Magnets". In: *Physics Today* 54.5 (2001).

Rodmacq, B., S. Auffret, B. Dieny, S. Monso, and P. Boyer. "Crossovers from in-plane to perpendicular anisotropy in magnetic tunnel junctions as a function of the barrier degree of oxidation". In: *Journal of Applied Physics* 93.10 (2003).

Sakuma, A. "Electronic structures and magnetism of CuAu-type MnNi and MnGa". In: *Journal of Magnetism and Magnetic Materials* 187.1 (1998).

Scherz, A. "Spin-dependent X-ray absorption spectroscopy of 3d transition metals: systematics and applications ". Ph.D. Thesis. Freie Universität Berlin, 2003.

Schmalhorst, J., D. Ebke, M. Meinert, A. Thomas, G. Reiss, and E. Arenholz. "Element-specific study of the temperature dependent magnetization of Co-Mn-Sb thin films". In: *Journal of Applied Physics* 105.5 (2009).

Schmalhorst, J., S. Kämmerer, M. Sacher, G. Reiss, A. Hütten, and A. Scholl. "Interface structure and magnetism of magnetic tunnel junctions with a $Co_2MnSi$ electrode". In: *Physical Review B* 70.2 (2004).

Schmalhorst, J., A. Thomas, S. Kämmerer, O. Schebaum, D. Ebke, M. Sacher, G. Reiss, A. Hütten, A. Turchanin, A. Gölzhäuser, and E. Arenholz. "Transport properties of magnetic tunnel junctions with $Co_2MnSi$ electrodes: The influence of temperature-dependent interface magnetization and electronic band structure". In: *Physical Review B* 75.1 (2007).

Schütz, G., W. Wagner, W. Wilhelm, P. Kienle, R. Zeller, R. Frahm, and G. Materlik. "Absorption of Circularly Polarized X-Rays in Iron". In: *Physical Review Letters* 58.7 (1987).

Shang, C. H., J. Nowak, R. Jansen, and J. S. Moodera. "Temperature dependence of magnetoresistance and surface magnetization in ferromagnetic tunnel, junctions". In: *Physical Review B* 58.6 (1998).

Shiota, Y., T. Maruyama, T. Nozaki, T. Shinjo, M. Shiraishi, and Y. Suzuki. "Voltage-Assisted Magnetization Switching in Ultrathin $Fe_{80}Co_{20}$ Alloy Layers". In: *Applied Physics Express* 2.6 (2009).

Skowroński, W., T. Stobiecki, J. Wrona, K. Rott, A. Thomas, G. Reiss, and S. van Dijken. "Interlayer exchange coupling and current induced magnetization switching in magnetic tunnel junctions with MgO wedge barrier". In: *Journal of Applied Physics* 107.9 (2010).

Slonczewski, J. C. "Conductance and exchange coupling of two ferromagnets separated by a tunneling barrier". In: *Physical Review B* 39.10 (1989).

— "Current-driven excitation of magnetic multilayers". In: *Journal of Magnetism and Magnetic Materials* 159 (1996).

Smit, J. "The spontaneous Hall effect in ferromagnetics I". In: *Physica* 21.6-10 (1955).

Soriano, L., M. Abbate, H. Pen, M. T. Czyżyk, and J. C. Fuggle. "The interaction of N with Ti and the oxidation of TiN studied by soft X-ray absorption spectroscopy". In: *Journal of electron spectroscopy and related phenomena* 62.1 (1993).

Spieß, L., R. Schwarzer, H. Behnken, and G. Teichert. *Moderne Röntgenbeugung*. Vol. 2. Vieweg+ Teubner, Wiesbaden, 2005.

Sterwerf, C., M. Meinert, J.-M. Schmalhorst, and G. Reiss. "High TMR Ratio in $Co_2FeSi$ and $Fe_2CoSi$ Based Magnetic Tunnel Junctions". In: *IEEE Transactions on Magnetics* 49.7 (2013).

Stoner, E. C. and E. P. Wohlfarth. "A mechanism of magnetic hysteresis in heterogeneous alloys". In: *Philosophical Transactions of the Royal Society of London. Series A. Mathematical and Physical Sciences* (1948).

Sugihara, A., S. Mizukami, Y. Yamada, K. Koike, and T. Miyazaki. "High perpendicular magnetic anisotropy in $D0_{22}$-$Mn_{3+x}Ge$ tetragonal Heusler alloy films". In: *Applied Physics Letters* 104.13 (2014).

Tedrow, P. M. and R. Meservey. "Spin Polarization of Electrons Tunneling From Films of Fe, Co, Ni, and Gd". In: *Physical Review B* 7.1 (1973).

Thole, B. T., R. D. Cowan, G. A. Sawatzky, J. Fink, and J. C. Fuggle. "New Probe for the Ground-State Electronic-Structure of Narrow-Band and Impurity Systems". In: *Physical Review B* 31.10 (1985).

Thomson, W. "On the electro-dynamic qualities of metals:–effects of magnetization on the electric conductivity of nickel and of iron". In: *Proceedings of the Royal Society of London* (1856).

Tsai, C. C., C. W. Cheng, and M. C. Tsai. "Superparamagnetic States and Perpendicular Magnetic Anisotropy in Ultrathin MgO/ CoFeB/ Ta Structures". In: *IEEE Transactions on Magnetics* 50.1 (2014).

Tsai, M. C., C. W. Cheng, C. C. Tsai, and G. Chern. "The intrinsic temperature dependence and the origin of the crossover of the coercivity in perpendicular MgO/ CoFeB/ Ta structures". In: *Journal of Applied Physics* 113.17 (2013).

ViolBarbosa, C. E., S. Ouardi, T. Kubota, S. Mizukami, G. H. Fecher, T. Miyazaki, X. Kozina, E. Ikenaga, and C. Felser. "Investigation of the $Mn_{3-\delta}Ga$/ MgO interface for magnetic tunneling junctions". In: *Journal of Applied Physics* 116.3 (2014).

Voss, S., M. Fonin, U. Rüdiger, M. Burgert, U. Groth, and Y. S. Dedkov. "Electronic structure of $Mn_{12}$ derivatives on the clean and functionalized Au surface". In: *Physical Review B* 75.4 (2007).

Wang, W. G. and C. L. Chien. "Voltage-induced switching in magnetic tunnel junctions with perpendicular magnetic anisotropy". In: *Journal of Physics D: Applied Physics* 46.7 (2013).

Wang, W. G., M. Li, S. Hageman, and C. L. Chien. "Electric-field-assisted switching in magnetic tunnel junctions". In: *Nature Materials* 11.1 (2011).

Weisheit, M., S. Fähler, A. Marty, Y. Souche, C. Poinsignon, and D. Givord. "Electric Field-Induced Modification of Magnetism in Thin-Film Ferromagnets". In: *Science* 315.5810 (2007).

Wen, Z., H. Sukegawa, S. Kasai, M. Hayashi, S. Mitani, and K. Inomata. "Magnetic Tunnel Junctions with Perpendicular Anisotropy Using a $Co_2FeAl$ Full-Heusler Alloy". In: *Applied Physics Express* 5.6 (2012).

Wen, Z., H. Sukegawa, S. Mitani, and K. Inomata. "Perpendicular magnetization of $Co_2FeAl$ full-Heusler alloy films induced by MgO interface". In: *Applied Physics Letters* 98.24 (2011).

Williamson, G. K. and W. H. Hall. "X-ray line broadening from filed aluminium and wolfram". In: *Acta metallurgica* (1953).

Winterlik, J., B. Balke, G. Fecher, C. Felser, M. Alves, F. Bernardi, and J. Morais. "Structural, electronic, and magnetic properties of tetragonal $Mn_{3-x}Ga$: Experiments and first-principles calculations". In: *Physical Review B* 77.5 (2008).

Winterlik, J., S. Chadov, A. Gupta, V. Alijani, T. Gasi, K. Filsinger, B. Balke, G. Fecher, C. A. Jenkins, F. Casper, J. Kübler, G. D.

Liu, L. Gao, S. S. P. Parkin, and C. Felser. "Design Scheme of New Tetragonal Heusler Compounds for Spin-Transfer Torque Applications and its Experimental Realization". In: *Advanced Materials* 24.47 (2012).

Wu, F., S. Mizukami, D. Watanabe, H. Naganuma, M. Oogane, Y. Ando, and T. Miyazaki. "Epitaxial $Mn_{2.5}Ga$ thin films with giant perpendicular magnetic anisotropy for spintronic devices". In: *Applied Physics Letters* 94.12 (2009).

Wurmehl, S., H. C. Kandpal, G. H. Fecher, and C. Felser. "Valence electron rules for prediction of half-metallic compensated-ferrimagnetic behaviour of Heusler compounds with complete spin polarization". In: *Journal of Physics: Condensed Matter* 18.27 (2006).

Yamada, N., H. Sakai, H. Mori, and T. Ohoyama. "Magnetic properties of $\epsilon$-$Mn_3Ge$". In: *Physica B* 149.1-3 (1988).

Yang, H. X., M. Chshiev, B. Dieny, J. H. Lee, A. Manchon, and K. H. Shin. "First-principles investigation of the very large perpendicular magnetic anisotropy at Fe | MgO and Co | MgO interfaces". In: *Physical Review B* 84.5 (2011).

Yonamoto, Y., T. Yokoyama, K. Amemiya, D. Matsumura, and T. Ohta. "Magnetism of an ultrathin Mn film on Co(100) and the effect of oxidation studied by x-ray magnetic circular dichroism". In: *Physical Review B* 63.21 (2001).

You, C. Y., T. Ohkubo, Y. K. Takahashi, and K. Hono. "Boron segregation in crystallized MgO/amorphous-$Co_{40}Fe_{40}B_{20}$ thin films". In: *Journal of Applied Physics* 104.3 (2008).

Yuasa, S. and D. D. Djayaprawira. "Giant tunnel magnetoresistance in magnetic tunnel junctions with a crystalline MgO (001) barrier". In: *Journal of Physics D: Applied Physics* 40.21 (2007).

Yuasa, S., A. Fukushima, and H. Kubota. "Giant tunneling magnetoresistance up to 410 % at room temperature in fully epitaxial Co/ MgO/ Co magnetic tunnel junctions with bcc Co (001) electrodes". In: *Applied Physics Letters* (2006).

Yuasa, S., T. Nagahama, A. Fukushima, Y. Suzuki, and K. Ando. "Giant room-temperature magnetoresistance in single-crystal Fe/MgO/Fe magnetic tunnel junctions". In: *Nature Materials* 3.12 (2004).

Zhang, S., P. M. Levy, A. C. Marley, and S. S. P. Parkin. "Quenching of magnetoresistance by hot electrons in magnetic tunnel junctions". In: *Physical Review Letters* 79.19 (1997).

Zhu, L. J., D. Pan, S. H. Nie, J. Lu, and J. H. Zhao. “Tailoring magnetism of multifunctional $\mathrm{Mn}_x\mathrm{Ga}$ films with giant perpendicular anisotropy”. In: *Applied Physics Letters* 102.13 (2013).

Zhu, L. and J. Zhao. “Perpendicularly magnetized $\mathrm{Mn}_x\mathrm{Ga}$ films: promising materials for future spintronic devices, magnetic recording and permanent magnets”. In: *Applied Physics A* (2013).

# *Acknowledgments*

First, I would like to thank Prof. Dr. Günter Reiss for giving me the opportunity to work in his laboratory on the present topic and for many fruitful discussions. Furthermore, I would like to thank Dr. Jan Schmalhorst for his constructive criticism and his advices, especially during our beamtimes at the Advanced Light Source.

My former supervisor Dr. Daniel Ebke deserves my deepest gratitude. I am very thankful for your support, advices, and our many discussions during the last years.

I would also like to thank Dr. Karsten Rott for maintenance of the equipment in the laboratory and Aggi Windmann for her support concerning bureaucratic matter.

I thank for the opportunity to work at BL 6.3.1 and BL 4.0.2 of the Advanced Light Source, Berkeley, USA. The Advanced Light Source, Berkeley, USA, which is supported by the Office of Science, Office of Basic Energy Sciences, of the U.S. Department of Energy, under Contract No. DE-AC02-05CH11231. Furthermore, I thank Dr. Elke Arenholz.

I would like to express my thanks to my students, especially Alessia Niesen and Andreas Gebauer.

Special thanks also go to my office colleagues Stefan Niehörster, Dr. Daniel Meier, Dr. Jan Rogge, Mike Gotzmann, and Michael van Straaten.

I thank all the colleagues who worked with me, in particular Christian Sterwerf, Alexander Böhnke, Christoph Klewe, and Dr. Timo Kuschel.

Special thanks go to the former PhD students, Dr. Volker Drewello, Dr. Zoë Kugler, Dr. Savio Fabretti, Dr. Patryk Krzysteczko, and Markus Schäfers, for their help during my early years on D2.

I would also like to thank PD Dr. Andy Thomas and Dr. Oliver Schebaum for their help with the Caesar package.

Finally, I would like to thank my family.